

15113

BROAD-BAND GEOMAGNETIC DEPTH-SOUNDING  
ALONG AN ANOMALOUS PROFILE IN THE CANADIAN CORDILLERA

by

HERBERT DRAGERT

B.Sc., University of Toronto, 1968

M.Sc., University of British Columbia, 1970

A THESIS SUBMITTED IN PARTIAL FULFILMENT OF  
THE REQUIREMENTS FOR THE DEGREE OF  
DOCTOR OF PHILOSOPHY

in the Department  
of  
GEOPHYSICS AND ASTRONOMY

We accept this thesis as conforming to the  
required standard

THE UNIVERSITY OF BRITISH COLUMBIA

March, 1973

In presenting this thesis in partial fulfilment of the requirements for an advanced degree at the University of British Columbia, I agree that the Library shall make it freely available for reference and study.

I further agree that permission for extensive copying of this thesis for scholarly purposes may be granted by the Head of my Department or by his representatives. It is understood that copying or publication of this thesis for financial gain shall not be allowed without my written permission.

Department of Geophysics

The University of British Columbia  
Vancouver 8, Canada

Date May 2, 1973

## ABSTRACT

A comprehensive, practical investigation of broad-band geomagnetic depth-sounding for profiles located in anomalous regions has been carried out in three stages.

First, instrumentation has been developed to record geomagnetic induction data over a wide range of frequencies (0.01 to 100 mHz). Both geomagnetic depth-sounding (GDS) and magnetotelluric (MT) data can be obtained; frequency response is linear or closely matched, permitting data analysis without frequency-dependent corrections. By recording the data in two overlapping frequency ranges, a wide dynamic range (~80 db) can be obtained, thus making this system particularly well suited to 'low- $\Delta Z$ ' regions such as the Canadian Cordillera, where attenuated short-period and normal-amplitude long-period vertical-field variations demand good sensitivity as well as an extensive dynamic range.

Secondly, analysis techniques for the evaluation of data from anomalous GDS profiles have been reviewed. For spectral estimation, an adaptation of the periodogram technique intended for large quantities of data, and an adaptation of the maximum entropy technique intended for limited data are discussed. The formulations of the single-station vertical transfer function and the paired-station transfer function matrix are reviewed and simple interrelations are derived. These techniques are then closely examined in the light of implicit assumptions and practical limitations.

Finally, a field study has been carried out investigating the detailed structure of the lateral conductivity discontinuity in the Cordillera geomagnetic 'transition' zone between Revelstoke and Calgary.

Analysis of data has revealed the presence of three conductive structures:

1) a near-surface conductor associated with sediments of the Rocky Mountain Trench; 2) a lower-crust/upper-mantle conductivity heterogeneity 40 to 50 km beneath the trench area, associated with possible hydration and partial melting; 3) a second deep conductivity structure orthogonal to the previous structure, associated with a buried Precambrian rift.

The interaction of the latter two conductors indicates that local deflection of current patterns induced over a larger region takes place.

## TABLE OF CONTENTS

	Page
ABSTRACT	(i)
TABLE OF CONTENTS	(iii)
LIST OF TABLES	(iv)
LIST OF FIGURES	(v)
ACKNOWLEDGEMENTS	(viii)
I. GENERAL INTRODUCTION	
1. Preface	1
2. Historical Background	2
3. Motivation and Outline of Thesis	8
II. INSTRUMENTATION DEVELOPMENT	11
III. DATA ANALYSIS TECHNIQUES FOR ANOMALOUS GDS PROFILES	30
IV. A FIELD INVESTIGATION OF THE CORDILLERA TRANSITION ANOMALY	53
V. SUMMARY	103
REFERENCES	105
APPENDICES	
I. Data Preparation	109
II A. Generation of the Variable-Width Window	113
II B. Computation of Transfer Function	114

LIST OF TABLES		Page
II-1.	Location of the four broad-band GDS systems during the 'pilot' project.	21
IV-1.	Summary of station identification and locations for the 'transition anomaly' profile.	60
IV-2.	Summary of digitizing information for the broad-band system data.	61
IV-3.	Harmonic peaks and phases for a 60-hour (360 points) 'quiet' record obtained by using the MEP technique.	65

	LIST OF FIGURES	Page
I-1.	Location of GDS stations in western Canada up to 1970. Profile A are stations of Hyndman (1963) and Lambert and Caner(1965); Profile B and C are stations described by Caner et al.(1967); Profiles D and E are stations of Dragert(1970). The dashed rectangle identifies the area containing the 20-station network of Lajoie and Caner(1970). (After Caner et al.,1971.)	3
I-2.	Conductivity structure model for southwest Canada, based on combined MT and GDS data. (After Caner, 1971.)	5
I-3.	Conductivity structure model for northern U.S. Rockies (48°N), based on GDS array data. (After Gough and Camfield, 1972.)	7
II-1.	Instrumentation for the 'broad-band' GDS system.	14
II-2.	Block diagram of system circuitry for GDS application.	16
II-3.	Block diagram of system circuitry for MT application.	17
II-4.	Frequency response curves of the system.	19
II-5.	Example of system GDS recordings of long periods (Band A).	24
II-6.	Example of system GDS recordings of short periods (Band B).	25
II-7.	Example of system GDS recordings of 'noise' at a magnetically quiet period (Band B).	26
II-8.	Example of vertical-component Fourier spectra for a 60-minute record of Band B simultaneous at all four stations.	27
III-1.	The spectral estimate of the raw FFT power, and the smoothed FFT power obtained by convolution with a Parzen window of varying width.	34

	Page
III-2. Estimates of the raw spectral power of a 60-hour magnetically quiet record obtained by using the conventional periodogram, the MEM, and the MEP techniques.	38
III-3. Schematic diagram indicating the fields contributing to the observed magnetic field variations.	40
III-4. Examples of simple 'multiple-anomaly' structures.	50
IV-1. Aerial photograph of the Rocky Mountain Trench taken above Tete Jaune looking northwest along the Trench. The Rocky Mountains are on the right, the Cariboo Mountains on the left. (courtesy of Dept. of Lands, Forest, and Water Resources, B.C.)	54
IV-2. Station locations for the field investigation of the 'transition zone' anomaly.	59
IV-3. Sample of Band B data recorded at broad-band stations.	66
IV-4. Smoothed spectral estimates for Band B averaged over 11 events. Component power ratios are also shown for selected periods. (Graph of geomagnetic latitude indicates possible latitude effects.)	67
IV-5. Sample of Band A data recorded at all profile stations.	69
IV-6. Smoothed spectral estimates for Band A for a sample event of 36 hours. Component power ratios are also shown for selected periods. (Graph of geomagnetic latitude indicates possible latitude effects.)	70
IV-7. Power attenuation ratios, $M_H$ , for Bands A and B determined from the spectra illustrated in Figs. IV-4 and IV-6.	71
IV-8. Single-station transfer function amplitudes and directions for Band B. Directions are measured positive east of true north.	73
IV-9. Single-station transfer function arrows for Band B. The in-phase vectors are negative to follow Parkinson's convention.	74



	Page
IV-10. Single-station transfer function amplitudes for Band A.	76
IV-11. Single-station transfer function directions for Band A (measured positive east of true north).	77
IV-12. Single-station transfer function arrows for Band A. The in-phase vectors are negative to follow Parkinson's convention.	78
IV-13. Average coherences between field components at the reference site and those at the closest and furthest station for Band A and Band B.	80
IV-14. Diagonal elements of the paired-station transfer matrix as functions of period (Band A) at each site.	82
IV-15. Elements $h_z$ and $d_z$ of the paired-station transfer matrix as functions of period (Band A) at each site.	84
IV-16. Elements $h_D$ and $d_H$ of the paired-station transfer matrix as functions of period (Band A) at COC.	85
IV-17. The vertical transfer function elements $z_H$ and $z_D$ contained in the transfer matrix T as functions of period (Band A).	86
IV-18. Elements $z_H'$ and $z_D'$ of the single-station vertical transfer function, $T_z$ , as functions of period (Band A) at BAN, COC, and SUF.	87
IV-19. The in-phase transfer function computed for Caner's (1971) and Gough and Camfield's (1972) conductivity models and the observed values. The response of an 'intermediate' model is also shown.	95
IV-20. Assumed boundaries of buried Precambrian rift in southwestern Alberta. Circles indicate Dominion Observatory gravity stations. (After Kanasewich et al., 1969.)	101

## ACKNOWLEDGEMENTS

I would like to thank Dr. G. K. C. Clarke for his extremely liberal supervision throughout the course of this thesis work. I am also indebted to the late Dr. B. Caner of the Victoria Geophysical Observatory for his direction and support of the instrumentation development. Personal thanks are extended to T. J. Ulrych and O. G. Jensen of the Department of Geophysics and Astronomy, University of B.C., for their helpful discussions on spectral analysis techniques, and the the personnel at the University of B.C. Computing Centre, especially J. W. Coulthard and B. B. Kerr, for their spontaneous help in the extensive computing required in the numerical analysis of data. The use of equipment from the Earth Physics Branch at Ottawa and Victoria and the financial support of both the National Research Council and the Defense Research Board are gratefully acknowledged.

## I. GENERAL INTRODUCTION

### 1. *Preface*

The prime purpose of this research was the investigation of the lower-crust/upper-mantle conductivity structure at the eastern edge of the Canadian Cordillera. In achieving this aim, the work of this thesis falls into three distinct parts:

- 1) Instrumentation Development
- 2) Analysis Technique Evaluation
- 3) Detailed Field Investigation

Conceptually, these sections are highly interdependent. For example, the instrumentation was designed particularly for geomagnetic field measurements in areas having strongly attenuated vertical field fluctuations; the subsequent field work was carried out in such an area, and hence it also served as a pilot project for the evaluation of the instruments. Furthermore, the selection of analysis techniques was determined not only by the form of the data collected, but also by the particular geomagnetic field behaviour expected in the field study. However, in the course of this work, these topics were dealt with separately, and are therefore presented in three independent sections which may be read individually without loss of comprehension.

The design and development of the instrumentation was a joint project between the Department of Geophysics and Astronomy, University of British Columbia, and the Division of Geomagnetism of the Earth Physics Branch at the Victoria Geophysical Observatory. Much of this part of the work was carried out at Victoria under the direction of the late Dr. B. Caner, and a description of this instrument system has been published (Caner and Dragert, 1972). A small part of the section

dealing with the evaluation of analysis techniques has been incorporated in a paper submitted for publication (Dragert, 1973). The planning, organization, execution, and analysis of the field work was carried out solely by the candidate.

## 2. *Historical Background*

### (i) Geomagnetic Depth-Sounding in the Canadian Cordillera

Prompted by the pioneering work of Schmucker (1964) in the southwest U.S.A., various geomagnetic depth-sounding (GDS) and magnetotelluric (MT) studies have investigated the lateral conductivity inhomogeneities in the lower crust and upper mantle in western Canada. The GDS traverse carried out by Hyndman (1963) in southwestern Canada (see Fig. I-1) established the presence of a region west of  $117^{\circ}$  W longitude in which vertical field variations having periods less than 60 min were attenuated by about a factor of three compared to vertical field variations to the east. Subsequent work (Caner et al., 1967) mapped the extent of this 'low-I' region (where I is the ratio of vertical field variations divided by horizontal field variations) to a latitude of  $51^{\circ}$  N, with the low-I/high-I transition occurring in the area of the Rocky Mountain Trench. Further GDS mapping (Dragert, 1970) showed these low Z variations to be characteristic of the Canadian Cordillera west of the Trench to a latitude of at least  $54^{\circ}$  N. In general terms, this attenuation of the vertical field fluctuations in the period range of 5 to 20 min has been attributed to the presence of a more conductive lower crust and/or upper mantle underlying the Cordillera west of the Rocky Mountains.

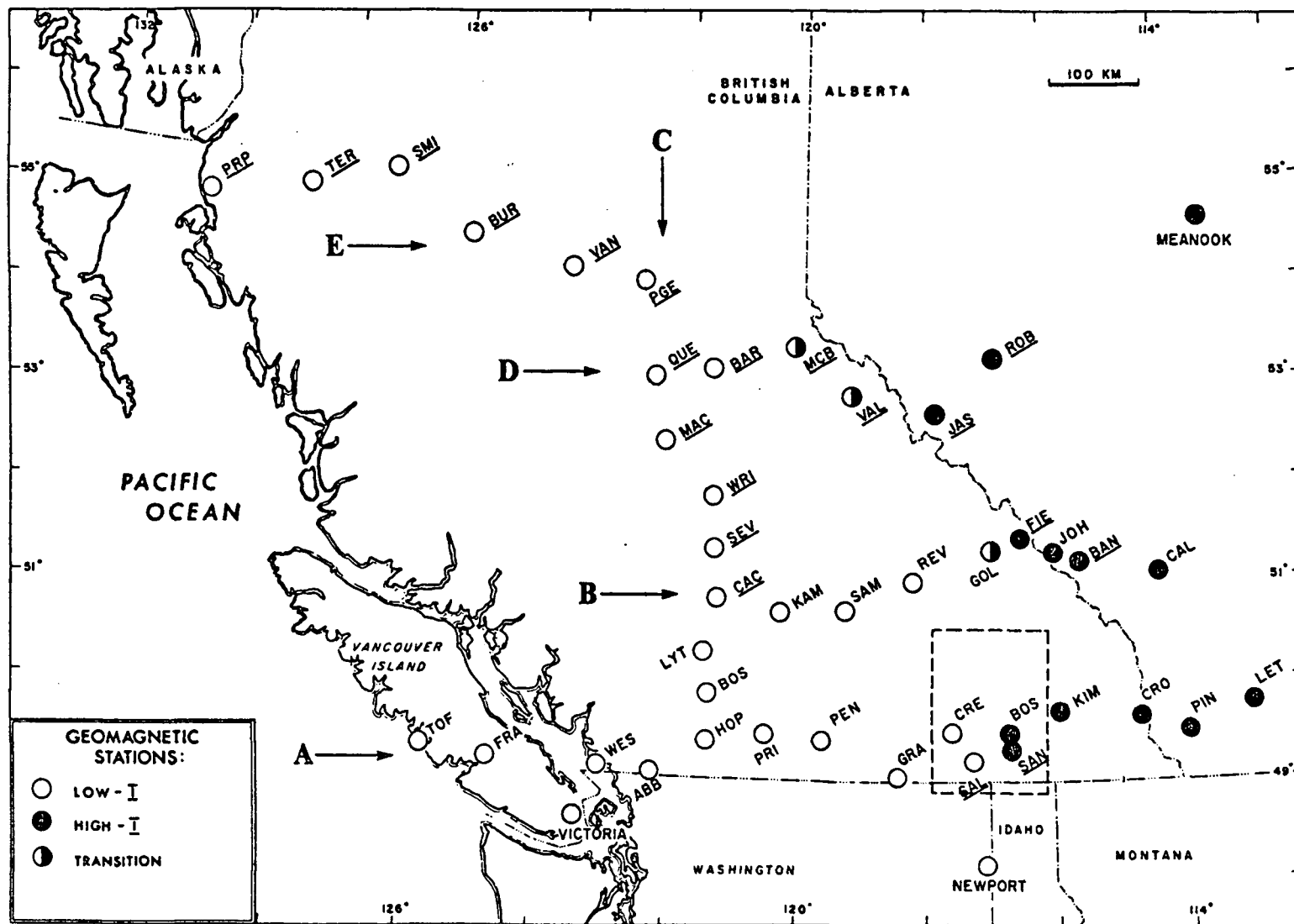


Fig. I-1. Location of GDS stations in western Canada up to 1970. Profile A are stations of Hyndman (1963) and Lambert and Caner (1965); Profile B and C are stations described by Caner et al.(1967); Profiles D and E are stations of Dragert(1970). The dashed rectangle identifies the area containing the 20-station network of Lajoie and Caner(1970). (After Caner et al.,1971.)

During the course of these primarily qualitative investigations, three anomalous geomagnetic areas were located: 1) the coast anomaly, 2) the Kootenay anomaly, and 3) the Trench anomaly. (The term 'anomalous' is applied to localities where one or more of the variational field components are functions of azimuth.) Located by Hyndman's initial profile, the first two anomalies have been subject to more detailed study. Lambert and Caner (1965) interpreted the 'coast effect' at the west coast of Vancouver Island as a combination of two effects: 1) the conductivity contrast of the land-sea interface and 2) inhomogenities in the upper mantle associated with the edge of the continental shelf. Lajoie and Caner (1970) have found the strong anomaly at Kootenay Lake to be due to a sharp, east-west trending conductivity discontinuity, possibly associated with a deep sinistral strike-slip feature in a subsequently inert basement. The Trench anomaly located at the western front of the Rocky Mountains in both the Golden and McBride areas, appears to be associated with the high-I/low-I transitional zone. A detailed investigation of this anomaly comprises one third of the work of this thesis.

#### (ii) Proposed Conductivity Models

Based on an assumption of a simple two-layer structure, Caner and Cannon (1965) presented an initial conductivity model for southwest Canada. It consisted of an upheaved conductive mantle, with a conductivity of roughly  $1 \text{ (ohm-m)}^{-1}$  beneath the western low-I zone, coming within 15 km of the surface, but remaining at greater depths (100 to 500 km at Lethbridge) under the high-I zone. A revised three-layer model was subsequently proposed by Caner et al. (1967): the western  $\Delta Z$

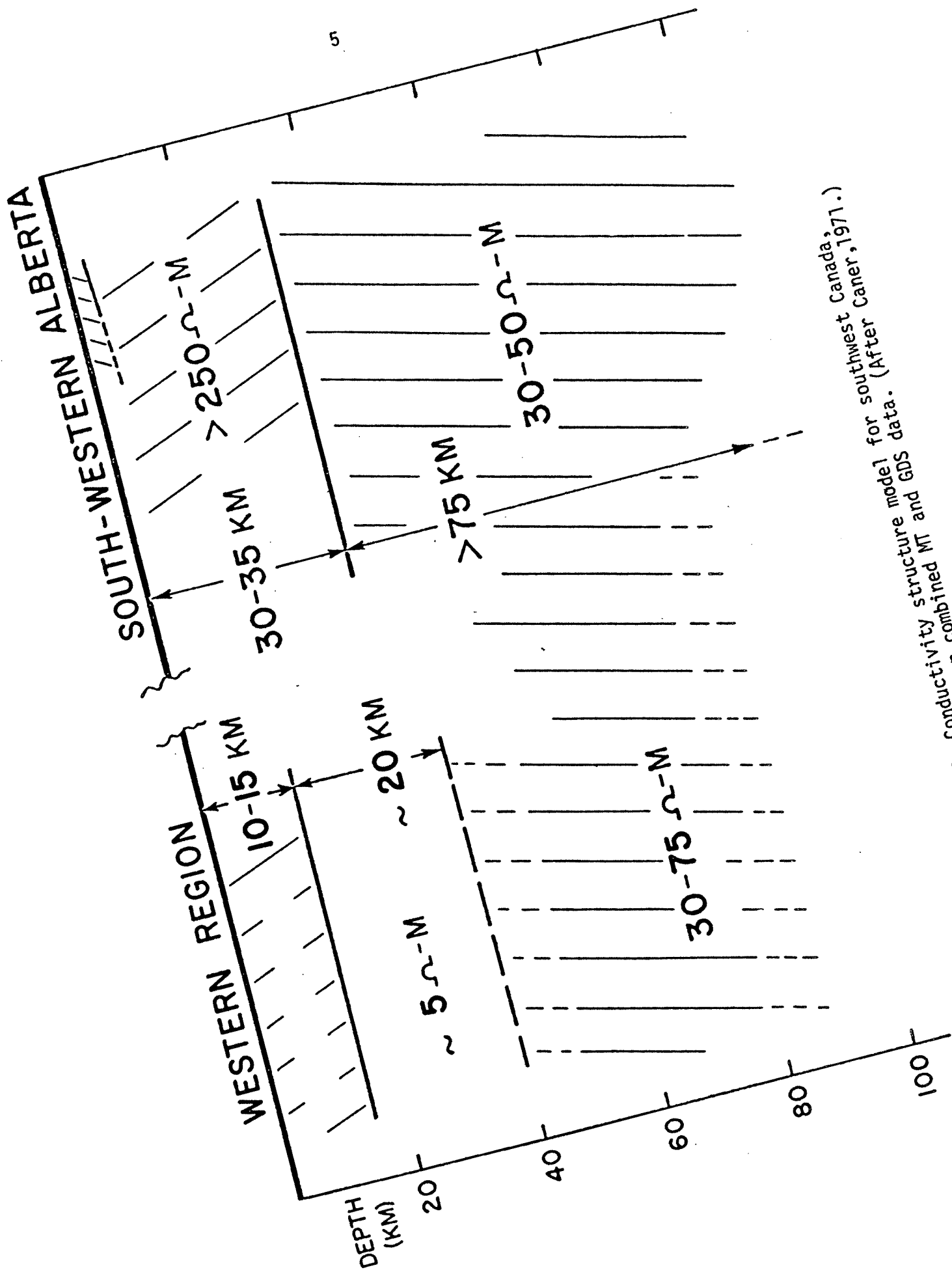


Fig. 1-2. Conductivity structure model for southwest Canada, (After Caner, 1971.)

attenuation was attributed to a layer 15 to 20 km thick at a depth of 30 km and having a conductivity of about  $1 \text{ (ohm-m)}^{-1}$ .

A comprehensive, integrated GDS/MT and petrological investigation of the electrical conductivity structure of the lower crust and upper mantle in southwestern Canada was carried out by Caner (1969). Figure I-2 shows the most recent conductivity model derived by Caner using primarily parametric fitting to obtain observed MT surface impedances and observed GDS impedance ratios. A moderately conducting ( $0.02 \text{ to } 0.03 \text{ (ohm-m)}^{-1}$ ) sub-stratum is proposed to underlie the entire Cordillera at a depth of about 35 km. At the western front of the Rocky Mountains and towards the west, the lower crust (from a depth of 10 to 15 km) becomes conductive as well, the most likely cause being hydration and possible partial melting.

By calculation of transfer functions, Cochran and Hyndman (1970) corrected the observed vertical-field fluctuations for anomalous contributions. From their adjusted impedance ratios, they propose a model similar to Caner's, but their depths to the more conductive layers are roughly 15 km greater in both the western and eastern regions. From two-dimensional array GDS data, Gough and Camfield (1972) have proposed an alternate conductivity model for the American Northern Rockies area based primarily on a line of their 'station grid' lying just south of the U.S. - Canada border. Figure I-3 illustrates the general features of their suggested model. For both western and eastern regions a resistive crust and mantle ( $0.001 \text{ (ohm-m)}^{-1}$ ) extend to 350 km where the conductive mantle ( $0.1 \text{ (ohm-m)}^{-1}$ ) is encountered. The eastern region is overlain by a 2 km conductive layer of sediments, whereas the western region has a thicker, moderately conductive upper crustal layer. The low  $\Delta Z$  variations of the western Cordillera have been attributed to the presence of a thin (10 to 20 km)



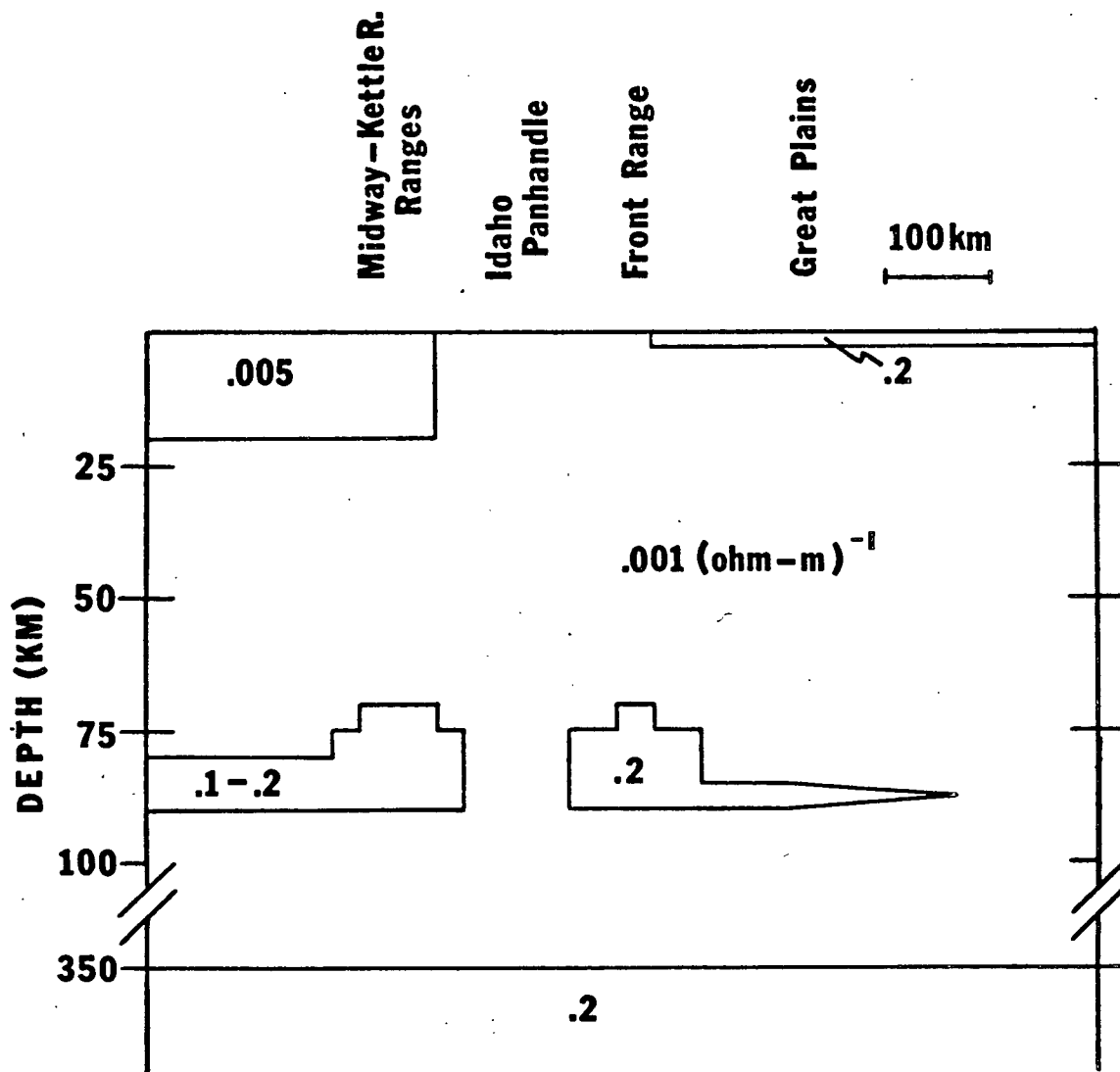


Fig. I-3. Conductivity structure model for northern U.S. Rockies (48°N), based on GDS array data. (After Gough and Camfield, 1972.)

conductive layer at a depth of about 80 km. To account for a double-peak geomagnetic anomaly observed in the region of the Idaho Panhandle, a 100 km gap in this conductive layer is postulated, accompanied by a thickening of this layer at each side of the gap.

The differences between the models presented by Caner and by Gough and Camfield are obvious, and it is beyond the scope of a localized study to resolve the variances of two such models based on regional investigations. However, the detailed field work of this thesis can still reflect on the validity of either model for the anomalous transition zone between Revelstoke and Calgary.

### *3. Motivation and Outline of Thesis*

First, concerning data quality, it has been pointed out by Caner (1971), that instrumentation used for GDS studies in North America has been limited to a resolution of the order of 1 to 2 $\gamma$ . Within the low-I zone of the Cordillera, this resolution has restricted the recording of vertical-component data having adequate signal-to-noise ratio to a frequency band between  $10^{-3}$  to  $10^{-5}$  Hz. Conductivity models based on such narrow banded data collected from a single profile are consequently subject to large ambiguities.

Secondly, for the quantitative interpretation of GDS data recorded within an anomalous area, it is imperative that a 'best-possible' separation of the 'anomalous field', i.e. the field due to internal earth currents associated with lateral conductivity discontinuities, and the 'normal field', i.e. the field due to external and internal currents in an area of horizontal conductivity layering, be carried out. For data from a single profile, the single-station transfer function as formulated by

Everett and Hyndman (1967) appears to be the most practical technique to determine anomalous  $\Delta Z$  variations. Implicit in this approach is the assumption that anomalous vertical fields are induced primarily by horizontal field variations. However, anomalous fields may be due to an induction or conduction effect associated with horizontal or vertical source field fluctuations; consequently, the validity of the single-station transfer function must be examined in the light of a nine-element transfer matrix as first formulated by Schmucker (1970).

Thirdly, the geomagnetic anomaly associated with the high-I/low-I transition zone in western Canada has been located along a line bordering the western front of the Rocky Mountains from  $49^\circ$  N to at least  $54^\circ$  N latitude. It therefore presents a large scale tectonic feature meriting the attention of a detailed investigation.

The aims of this thesis are therefore as follows:

- 1) to develop broad-band GDS instrumentation for recording geomagnetic induction data over a wider range of frequencies;
- 2) to examine the transfer function technique for the analysis of GDS profile data;
- 3) to investigate in greater detail the nature of the geomagnetic anomaly between Revelstoke and Calgary.

The resolution of these proposals form the three separate, independently presented sections of this thesis:

- 1) The first section deals with the development of the 'broad-band' geomagnetic and telluric system. A description of the system as well as an outline of its general field operation are given, followed by an evaluation of the system based on the field study of this thesis, which served as a GDS pilot project for the new instrumentation.

2) The next section first outlines the spectral techniques employed for optimum data presentation in the frequency domain. An examination of the analysis methods of single-station vertical transfer functions and paired-station transfer matrices follows, which compares the two methods in the light of implicit assumptions and practical limitations.

3) The final section deals with the field work carried out along a profile between Clearwater, B.C., and Suffield, Alta., during the fall of 1971. Presented are the methods of collection, reduction and analysis of data and their subsequent qualitative and quantitative interpretation.

## II. INSTRUMENTATION DEVELOPMENT

	Page
1. Introduction	12
2. Description of the Broad-Band GDS System	15
3. General Operation of the System	20
4. Performance of the System during Pilot GDS Project	21
5. Evaluation of the Broad-Band System	23
6. Conclusions	26

## 1. Introduction

Geomagnetic induction work carried out by the Earth Physics Branch in Victoria and the Department of Geophysics and Astronomy at the University of B.C. has shown the western part of the southern Canadian Cordillera to be characterized by a strong attenuation of the vertical component fluctuations ( $\Delta Z$ ) at periods less than thirty minutes. Hence, most of this work has been concerned with the delineation and interpretation of this 'low- $\Delta Z$ ' region. Unfortunately, standard Z-variographs, such as Askania variographs or saturable core magnetometers, have limited sensitivities resulting in poor signal-to-noise ratios for short-period magnetic variations in such regions. Consequently, quantitative interpretation is usually based on a restricted bandwidth (about 1.5 decades) for which valid data are available, creating a large ambiguity in the choice of suitable conductivity structure models. In order to limit this choice of models, broader bandwidth data ( $>2.5 - 3$  decades) are required, and therefore it was decided to develop instrumentation to record short-period variations.

No innovations were required for time-scale resolution, since the shortest periods to be recorded were of the order of 5 s and even existing photographic variographs could be adapted for higher resolution by the modification of chart speeds.

The major problem then was to increase instrumental sensitivity to record small-amplitude, high-frequency variations, and yet remain within the dynamic range of the recording system for large-amplitude, long-period geomagnetic bays and diurnal fluctuations. It should be noted that the subsequent development of these broad-band GDS systems

involved simply a logical assemblage of two components that recently became available:

a) a commercially available, transistorized, three-component saturable-core magnetometer of modest cost (about \$3000). This instrument (Trigg et al., 1971) is a transistorized model of the tube-type "IGY" design of Serson (1957). Its D.C. power consumption is low enough ( $\sim 5$  w) to permit battery-powered mobile operation.

b) an automatic zero suppression circuit by Trigg (1970), which applies a baseline shift whenever the output signal of the magnetometer reaches a preset limiting value. This circuit can 'step' seven times in each direction, providing a greatly extended dynamic range; for example, with a step-back of  $100\gamma$  a total range of  $1600\gamma$  peak-to-peak can be handled even though the recording device operates at a full scale range of only  $200\gamma$ .

In addition, seven-channel slow-speed FM tape recorders (Geotech type 17373 and Precision Instruments type PI-5100) were available as recording systems and thus allowed the building up of four complete broad-band systems without impossible financial strain.

Fig. II-1. Instrumentation for the 'broad-band' GDS system.





## *2. Description of the Broad-Band GDS System*

Figure II-1 shows a photograph of the basic components of the broad-band GDS system: 1) the fluxgate instrument comprised of the cylindrical detector head (sitting on the wooden battery box) and its control electronics (uppermost within the transit case) which include the zero suppression circuits and internal timing board; 2) the interface-control unit (below fluxgate control unit) containing active filter-amplifier cards, signal monitor capabilities, and tape recorder calibration circuitry; 3) the slow-speed, seven-channel FM tape recorder (shown in front), recording three magnetic components in parallel long-period and short-period bands. The seventh channel can be used for carrier-wave reference (for the purpose of reducing recording noise) or to record an absolute time signal from a WWVB radio receiver (shown at bottom within transit case, with accompanying ferrite core antenna shown at right of the case). The system is fully weatherproof, with equipment being mounted within waterproof aluminum transit cases with adequate thermal and mechanical protection; all connections between units are made through external waterproof connectors and cables, enabling operation with all lids closed.

A block diagram of the circuitry used for geomagnetic depth-sounding work is shown in Figure II-2. In order to reach very short periods (5-10 s), the fixed fluxgate outputs are split into two bands: 1) Band A (D.C. to 200 s), the long-period band; using the "scale expanders" of Trigg (1970) provides an effective dynamic range of about 65-70 db (1600 $\gamma$  full-scale, with noise level under 0.5-1.0 $\gamma$  peak-to-peak in a low-pass frequency-restricted band). 2) Band B(500 s to 5 s), the

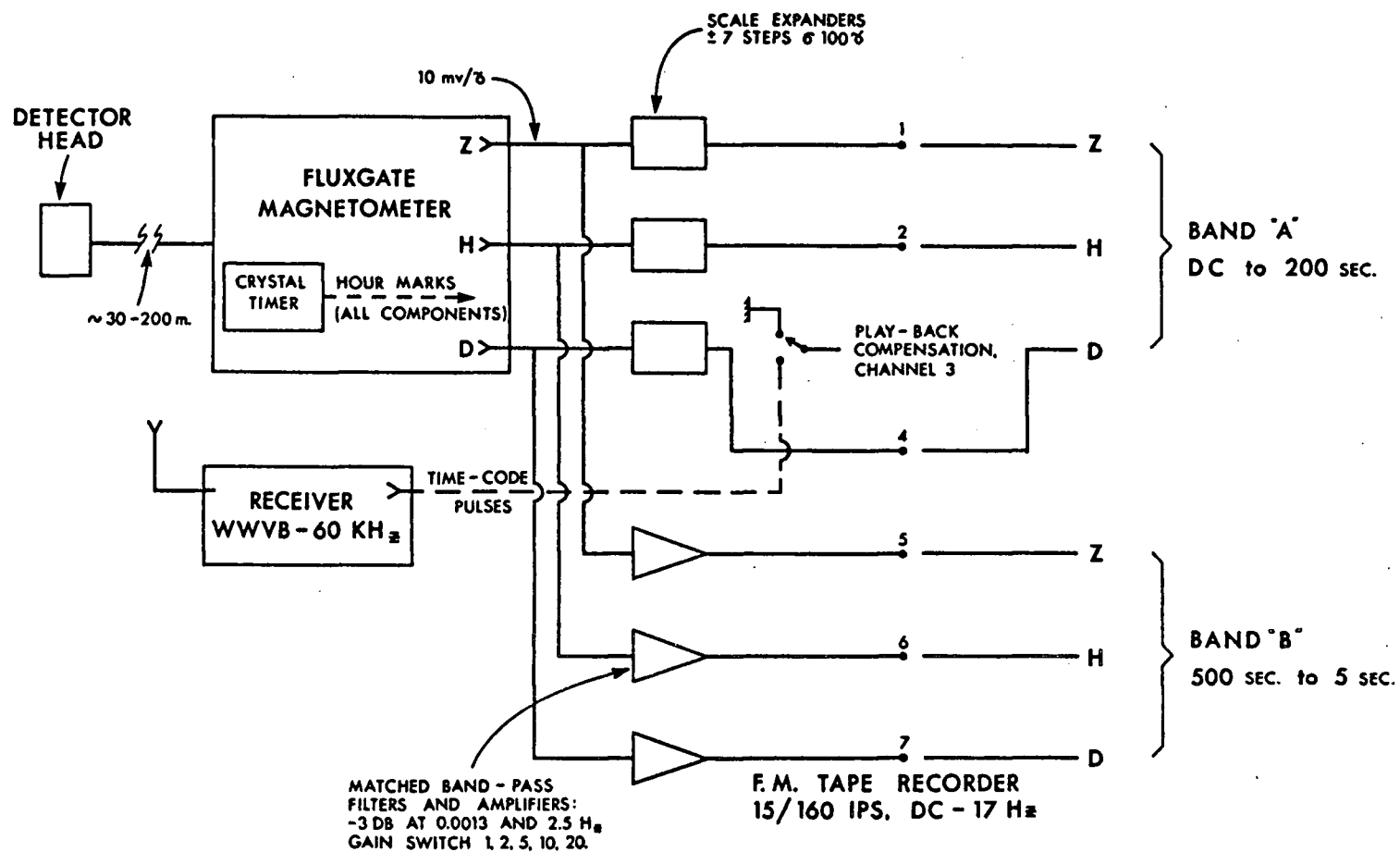


Fig. II-2. Block diagram of system circuitry for GDS application.

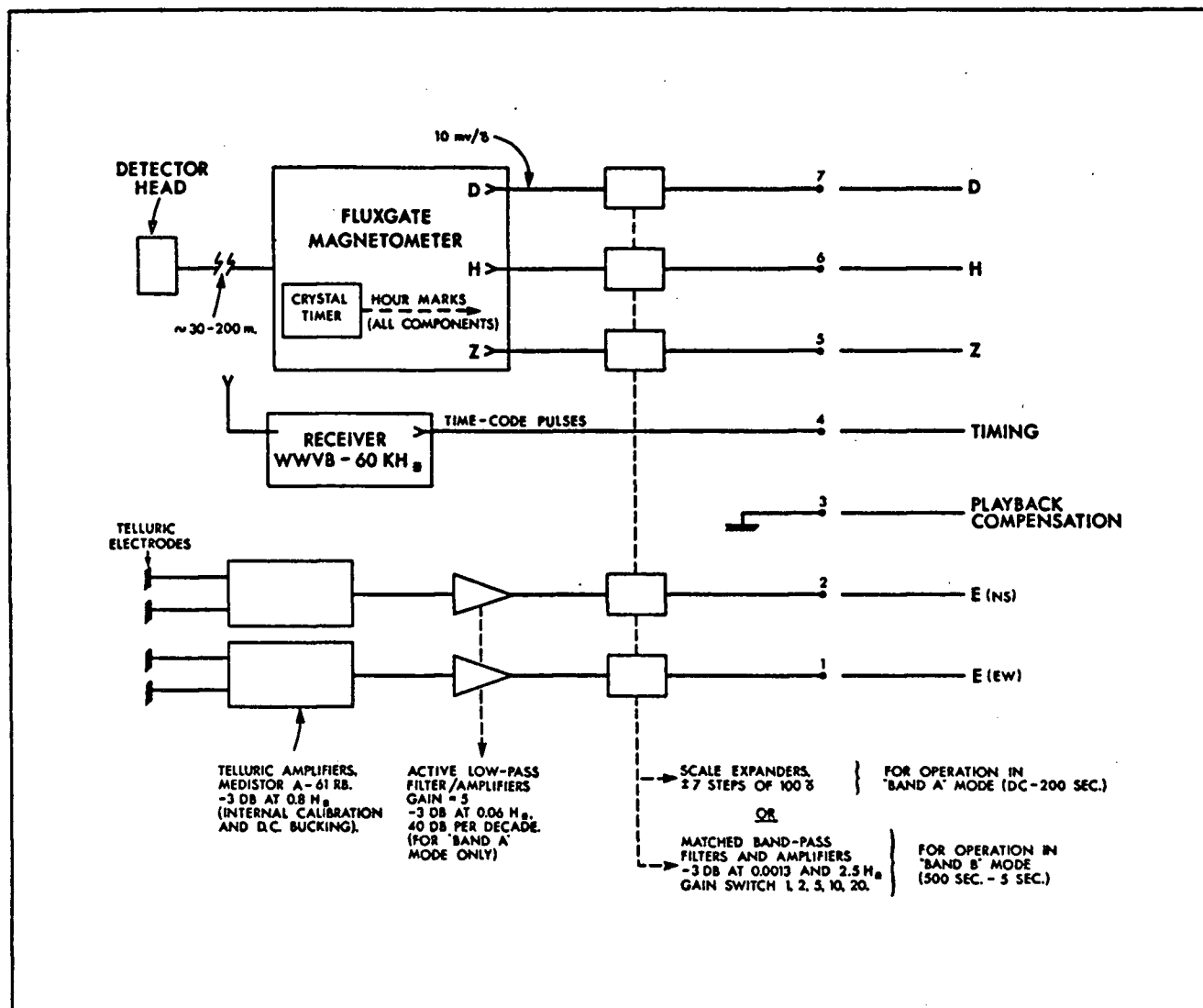


Fig. II-3. Block diagram of system circuitry for MT application.

short-period band; by inserting band-pass filters to attenuate the large-amplitude long-period fluctuations, additional amplification can be introduced to provide higher sensitivity for short-period fluctuations. Depending on the gain settings, resolution of signals as low as 0.1-0.2 $\gamma$  can be achieved, with a dynamic range of the order of 50 db. The overall effective "system" dynamic range is better than 78 db, and permits the extraction of quantitatively valid data over about 3.5-4 decades in frequency, even with "low- $\Delta Z$ " signals.

As shown in Figure II-2, Bands A and B are recorded simultaneously using six of the tape recorder channels. One of the channels (channel three) is operated with shorted input to provide automatic flutter compensation on playback, resulting in a significant improvement in signal-to-noise ratio. At the start and end of each tape, time marks from a standard-frequency radio receiver are recorded on this channel to provide absolute time calibration of the internally-generated hour marks.

Although the system was developed primarily for geomagnetic depth-sounding, a magnetotelluric adaptation was also built and tested at Victoria. A block diagram of this MT version is shown in Figure II-3. Since five channels are required for each band (three magnetic and two electric components), the two frequency bands are recorded separately. In that case, radio timing as well as playback compensation are applied continuously. Data in the two bands are recorded in consecutive periods, but could of course be recorded simultaneously if two tape recorders per station were available.

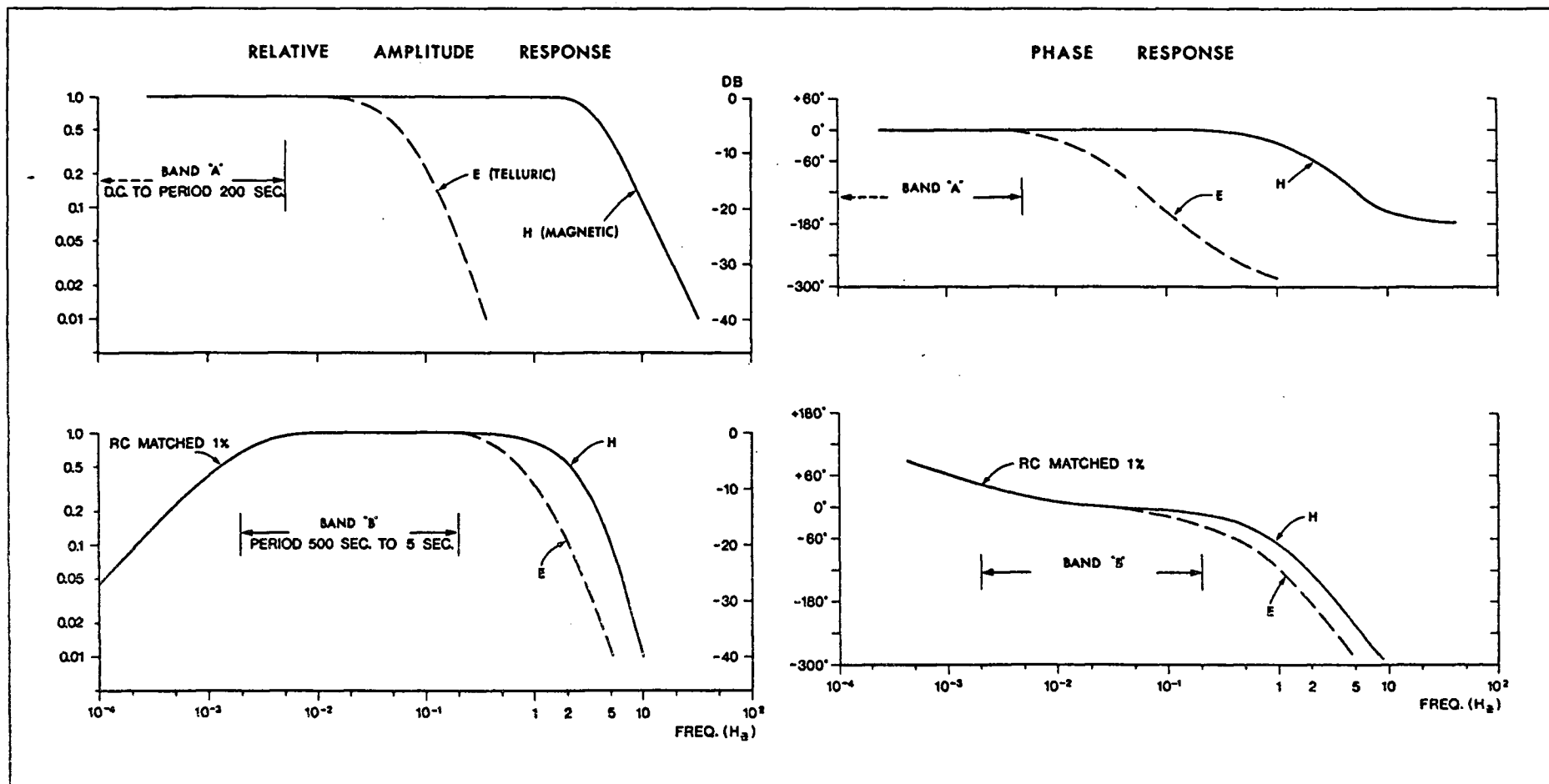


Fig. II-4. Frequency response curves of the system.

The overall frequency response curves of the systems are shown in Figure II-4. Active filters provide the required sharp high-frequency cutoffs and the low-cut characteristics for Band B. It should be noted that frequency response characteristics within signal bands are either rigorously flat or closely matched. Consequently, data analysis, which is usually concerned with ratios between components in this type of work, can be carried out without any frequency-dependent instrument-response corrections.

### *3. General Operation of the System*

The fluxgate sensing head is usually mounted on a cement-embedded, vertical aluminum pipe placed in a covered pit in order to reduce temperature variations. A shielded cable carries the signal to the control equipment located at least 50 feet from the sensor. The control electronics are adequately protected in the insulated, weatherproof transit cases which require no further enclosures. However, the tape recorder electronics are extremely temperature and humidity sensitive, and must be kept in a reasonably dry environment at over 32° F to function according to manufacturer's specifications.

In mobile operation, each GDS system requires the following batteries: two 18-Volt batteries for the fluxgate and other electronic circuitry, and one or two 12-V batteries for the tape recorder (depending on whether a PI or Geotech instrument is used). Each 10.5 inch diameter tape reel, holding 3600 feet of tape and recording at 15/160 IPS, lasts for over 120 hours, permitting a 5-day service cycle for unattended stations. Using heavy-duty batteries (100 AH for 18-V batteries), adequately constant voltage is maintained for these 5 days. Smaller 18-V batteries could be used without any significant deterioration in data

quality, as the equipment is quite insensitive to power supply parameters. For sites where line power is available, the batteries can be omitted, since the equipment can be operated directly from line power; internal voltage regulation is provided so that the quality of the line power is not critical in either voltage or frequency. Alternatively, the batteries can be connected in a "stand-by" configuration to provide recording continuity during line power failures.

#### *4. Performance of the System during Pilot GDS Project*

During a period of two months, beginning mid-September 1971, four complete broad-band GDS systems were operated as part of a short-spaced profile in the Rocky Mountain Trench area near Golden, British Columbia. The locations of these four systems are given in Table II-1.

<u>Station</u>	<u>Longitude</u>	<u>Latitude</u>	<u>Geomagnetic Latitude</u>
Downie Creek (DOW)	118.2°W	51.3°N	58.0°N
Rogers Pass (ROG)	117.6°W	51.2°N	58.1°N
Nicholson (NIC)	117.0°W	51.3°N	58.3°N
Banff (BAN)	115.6°W	51.2°N	58.6°N

Table II-1. Location of the four broad-band GDS systems during the 'pilot' project.

All sites were easily accessible by road and had facilities of either line or diesel-generated electric power. Consequently, all systems used A.C. power for operation, but batteries were also connected in a stand-by configuration to ensure continuous recording during power failures or diesel-generator shut-downs. Indoor sheltering for the



temperature and humidity sensitive tape recorders was available at all sites except Rogers Pass where an insulated, weatherproof wooden shelter was used to house the recorder. During the course of the project, low temperatures and wet weather necessitated the addition of a drying agent and an 8-w heating bulb within the recorder housing to ensure a dry, above-freezing environment. All recording was done using 10.5-inch precision reels holding 3600 feet of magnetic tape, thus permitting a five-day service cycle. The relatively short spacing of stations and their ease of accessibility allowed efficient servicing by a single operator within this cycle, even during adverse weather conditions. Completed data tapes were shipped in magnetically shielded, insulated transit boxes to the University of British Columbia where a brief playback of tapes would reveal any serious instrument failures which were subsequently communicated to the field operator for correction.

All four systems were operated simultaneously for a period of 55 days, each recording 6 channels of data and thus giving 330 'channel-days' of possible records at each site, a possible 1320 channel-days for the entire project. The data loss due to instrument failure was approximately 200 channel-days, giving a better than 80% relative data return. Tape recorder failure was the primary cause of system breakdown, and would certainly have caused greater data loss but for the constant attention of the five-day service cycle. Over the first fifteen days of operation, ample simultaneous short-period data had been recorded for a thorough Band B analysis. It was expected to collect sufficient long-period data for Band A analysis within thirty days; however, the infrequent occurrence of magnetic storms and the interruption of continuous, simultaneous records by successive servicing of tape stations prolonged data collection.

## 5. Evaluation of the Broad-Band System

### (i) Record Quality

Figure II-5 shows a sample of long-period data (Band A) recorded at Downie Creek. 'Step-backs' of the automatic zero suppression circuit (shown by arrows) illustrate the extension of the dynamic range. Each step is recorded as an instantaneous change of  $100\gamma$  and hence is usually recognizable even during intense magnetic disturbances. Peak-to-peak noise in this band was found to average from 1 to  $2\gamma$ . Short-period data at Rogers Pass (Fig. II-6) shows a section of record dominated by a 43-s period pulsation. Comparing the traces of this figure to those of Figure II-7, which were recorded at a magnetically undisturbed period, shows that a resolution of  $0.2\gamma$  is operationally attainable in Band B. To emphasize the increased sensitivity and extended coverage of the short-period band, an example of Fourier amplitude spectra of the vertical component simultaneous at all four stations is illustrated in Figure II-8. These spectra reveal that for this event, coincident spectral peaks exist for magnetic variations with amplitudes as low as  $0.4\gamma$ , and that power at 20-s periods is still above background noise. (For this event, a gain of 5 was used for the Z channel at all stations except at DOW where a gain of 10 was used.)

### (ii) Timing Marks

The hourly time marks generated by the fluxgate control unit were calibrated against a standard WWVB signal at the beginning and end of each tape. During the field project, the maximum deviation observed over a five-day period was two seconds, indicating an absolute timing stability of better than 1 part in  $2 \times 10^5$ . Furthermore, the timing drifts were generally linear and simultaneous playback of timing marks and the WWVB signal indicated that relative time could be recovered to within 0.2 s.

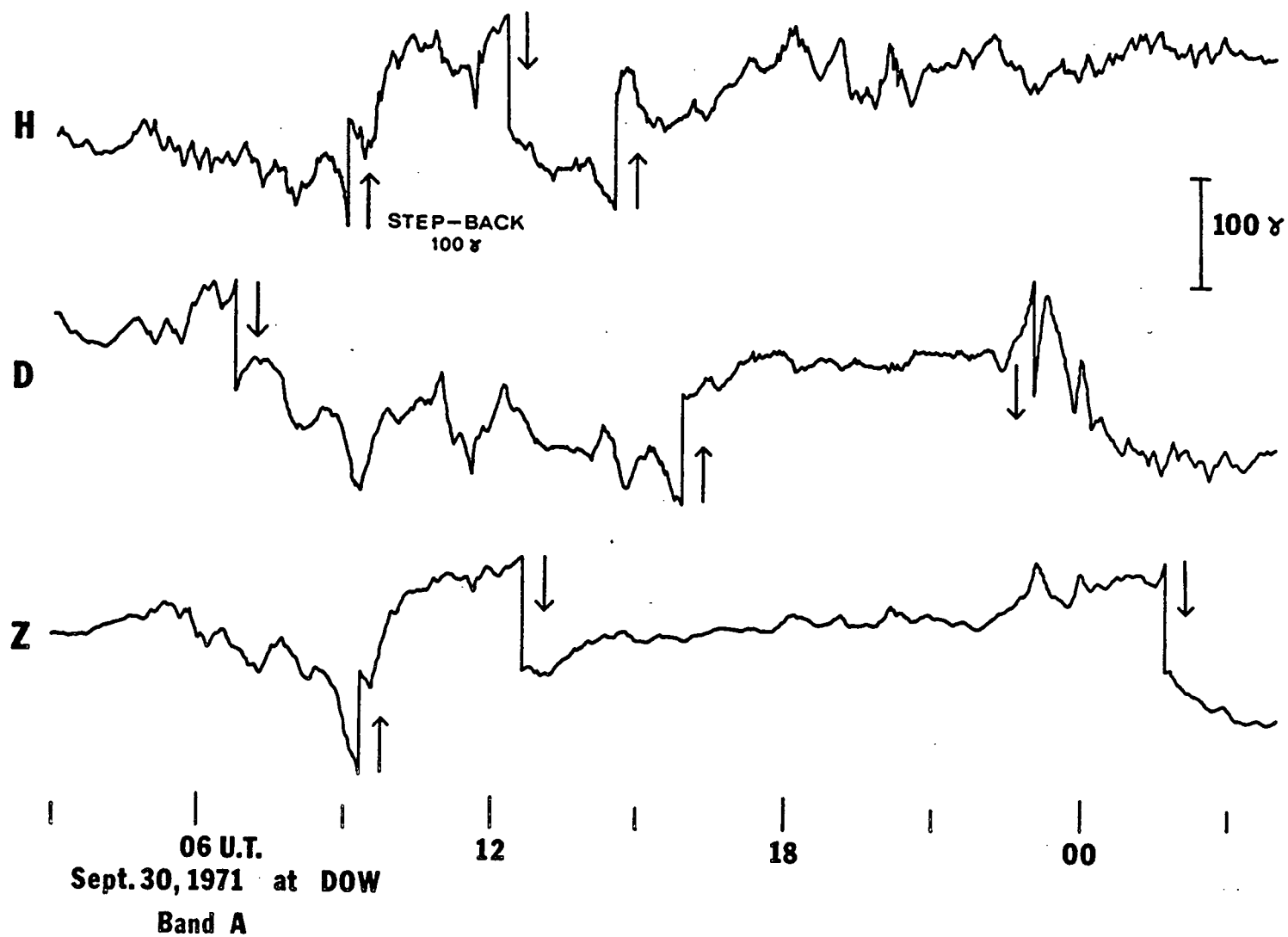


Fig. II-5. Example of system GDS recordings of long periods (Band A).

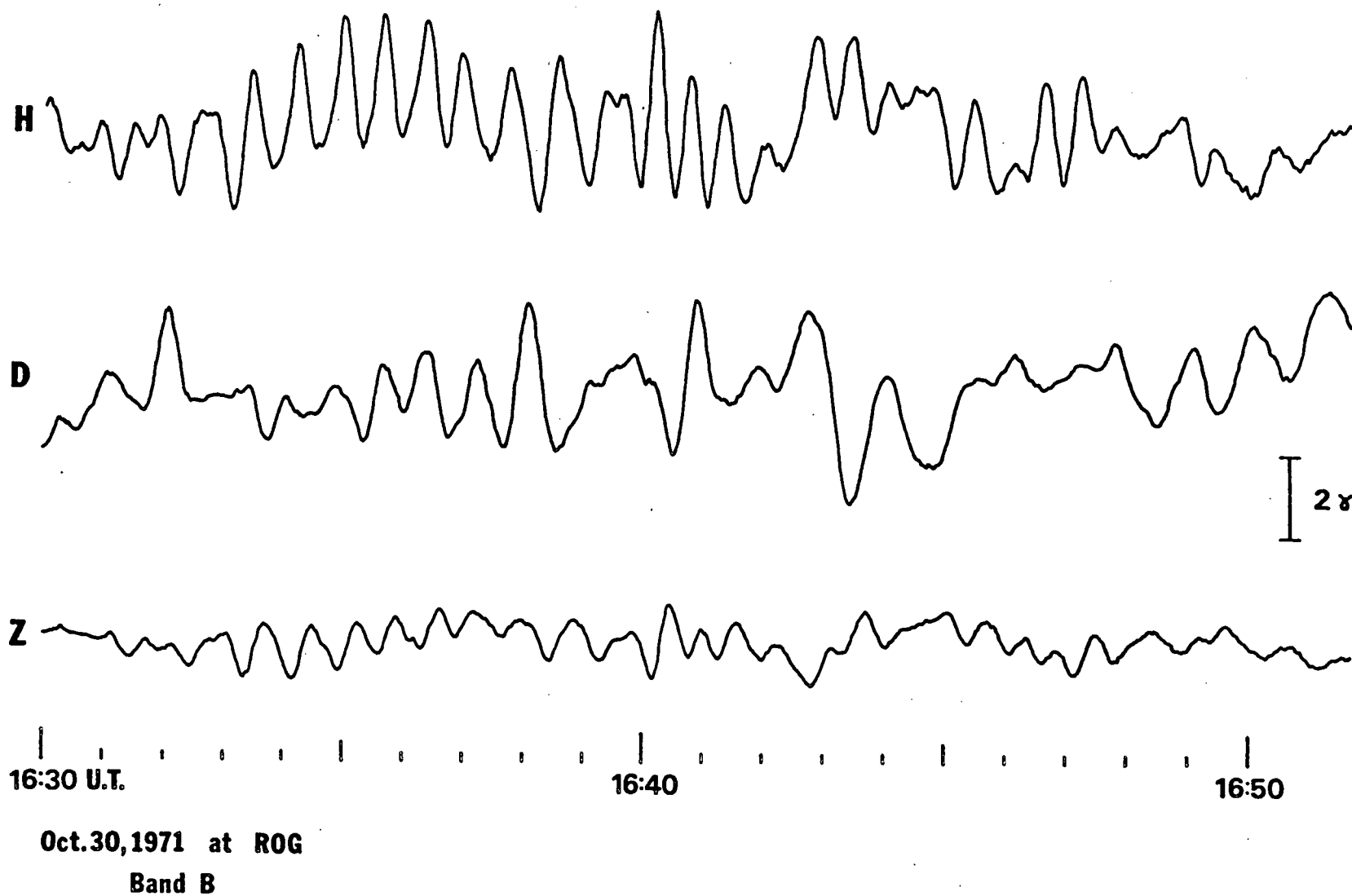
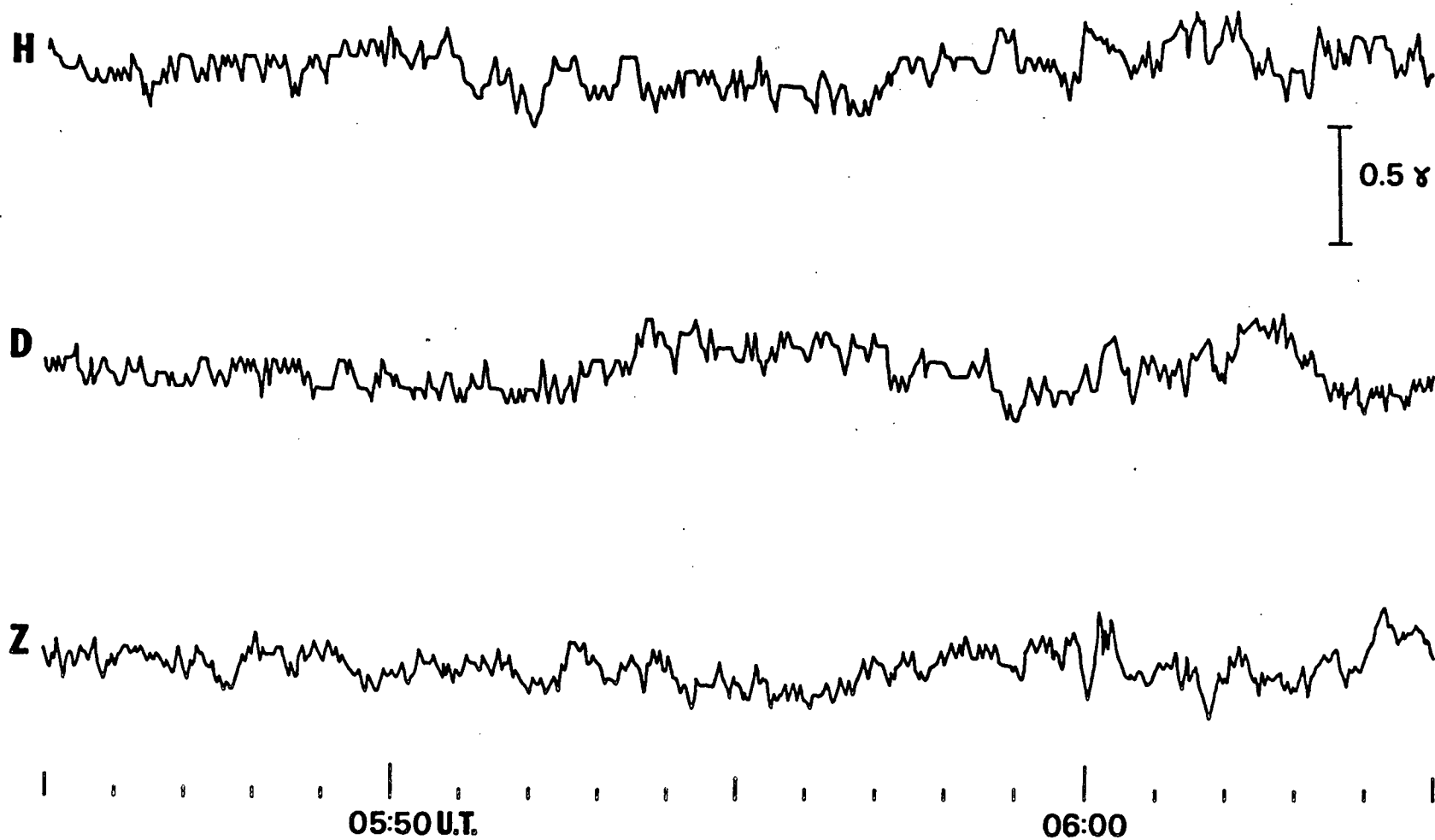


Fig. II-6. Example of system GDS recordings of short periods (Band B).



**NOV.2,1971 at ROG**  
**BAND B**

Fig. II-7. Example of system GDS recordings of 'noise' at a magnetically quiet period (Band B).

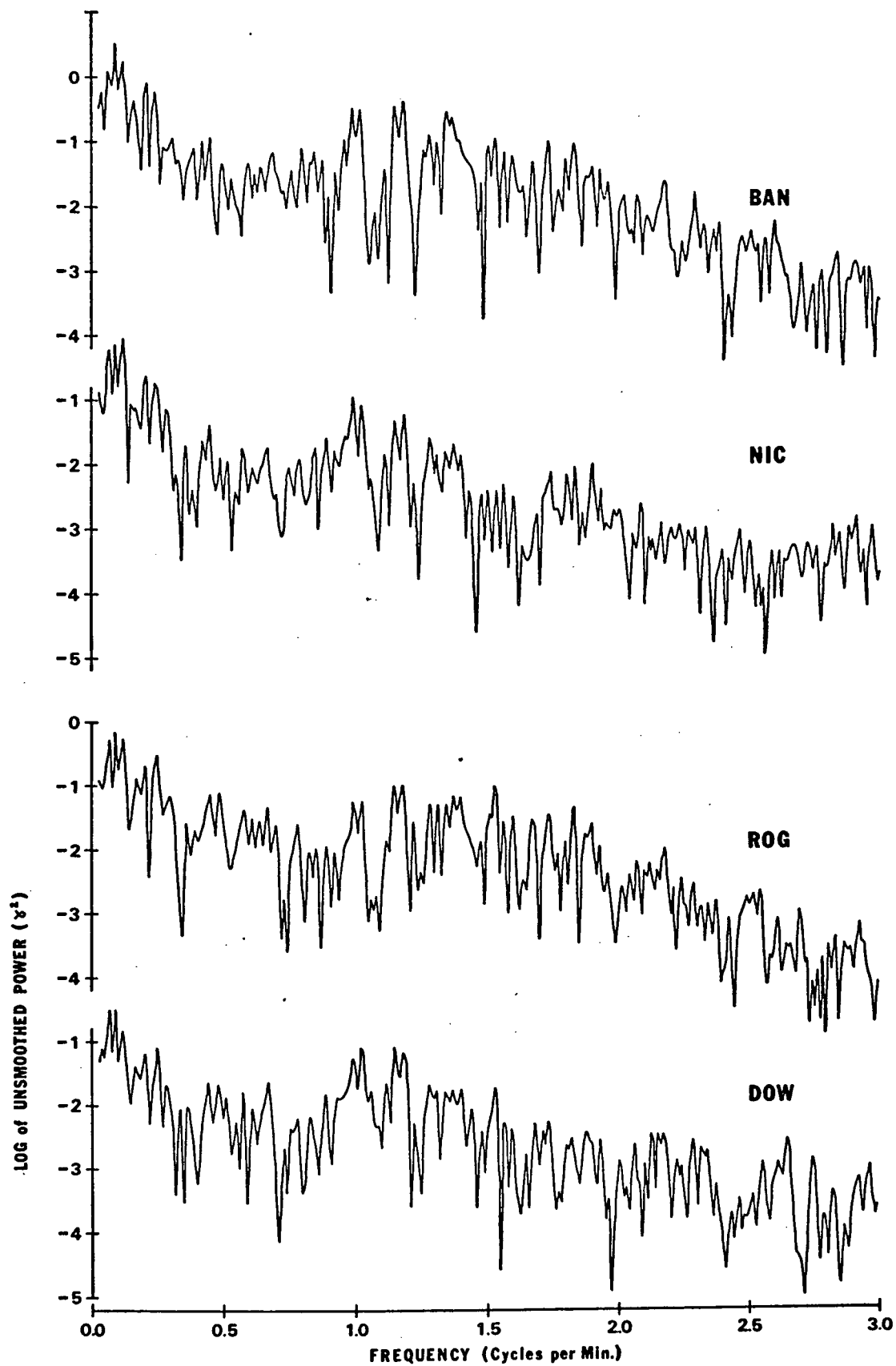


Fig. II-8. Example of vertical component Fourier spectra for a 60-minute record of Band B simultaneous at all four stations.

Unfortunately, the fluxgate control unit could not be easily altered to introduce time marks after the matched band-pass filter, resulting in a slowly decaying, filter-convolved step function appearing on Band B records. In spite of short-circuiting the time marks of the Band B components, power fluctuations due to relay closures still generated small pulses which were later removed from the digitized records. (See Appendix I for an outline of data processing.)

### (iii) Calibration

Calibrations of the systems were carried out at the beginning and end of each tape by an accurate  $\pm 1.0$  volt pulse from an internal battery. Over the 55-day project, three of the systems showed less than 2% variation in sensitivity. The tape recorder at Rogers Pass, subject to more extreme temperature changes (15°F to 65°F) showed calibration changes as large as 5%. However, when only the 'end-of-tape' calibrations, in which the temperature equilibrium of the tape recorder is left undisturbed, are considered, calibration variations averaged 1%.

## 6. *Conclusions*

Perhaps the only major shortcoming of this broad-band system is the fact that the gain of information achieved on the short-period side is at the expense of long-period (diurnal) data. The fluxgate sensing head presently used with the system lacks the temperature stability of the standard Askania variograph. Consequently, extreme daily temperature variations (~30°F or more) can limit the reliability of the long-period data. Furthermore, a practical shortcoming of the system rests with the method of recording. The slow-speed FM tape recorders appear to be too sensitive to temperature and humidity and hence are ill-suited to an

environment of extremes. Also, the five-day cycle imposed by the length of the data tapes makes it extremely difficult to record uninterrupted long-period events simultaneously at several stations. An obvious solution is to use longer data tapes (14-inch reels holding 7200 feet of tape), or better, to record long-period data on digital tapes having a 30-day cycle capability.

In general, it can be concluded that the pilot project has shown the instrumentation developed to be a valuable and practical new tool for field research in geomagnetic variation studies. The extended frequency range (0.01 to 100mHz) and the wide dynamic range (~ 80 db) of the two overlapping frequency bands, make this instrument system well suited to areas where short-period vertical field variations are strongly attenuated.



III. DATA ANALYSIS TECHNIQUES FOR ANOMALOUS  
GDS PROFILES

	Page
1. Introduction	31
2. Spectral Techniques	31
3. Transfer Function Techniques	39
4. Conclusions	51

## 1. *Introduction*

The analysis of geomagnetic depth sounding (GDS) data collected at isolated stations or along a profile is subject to two severe limitations:

1) the inability to separate external and internal parts of the field variations with the consequence that neither the time nor spatial dependence of the source field can be determined.

2) the subsequent inability to isolate internal fields due to horizontal conductivity layering (the induced normal fields), and those due to lateral conductivity discontinuities (the anomalous fields).

Unlike the two-dimensional analysis of grid-array data (c.f. Porath et al., 1971) which deals with these problems directly, the single-dimension approach must deal with these limitations indirectly, through assumptions and qualitative evaluation. The transfer function techniques (as described by Schmucker, 1970; and Everett and Hyndman, 1967) provide a practical, frequency-domain method for profile data analysis, but their success depends directly on how well they overcome the stated limitations. It is with this in mind that the formulation of the single-station vertical transfer function ( $T_z$ ) and the paired-station transfer matrix ( $T$ ) is briefly reviewed.

## 2. *Spectral Techniques*

To establish the frequency dependence of the magnetic field component powers at each site, and to evaluate the transfer functions, two spectral techniques were deemed useful.

### A. *Standard Spectral Method*

When ample simultaneous data were available at all stations of the profile, the following spectral method was employed. First, record sections were digitized with digitizing intervals and record durations

appropriate to the frequency band of interest. These digitized geomagnetic storm events were then prepared for Fourier transformation by the application of some or all of the following: removal of the mean and linear drifts; removal by least-mean-square fitting of the first four daily harmonics; pre-whitening; zero extension; and cosine-bell tapering. (See Appendix I for details.) The resultant real time series were arbitrarily given an imaginary part of zero to form complex series represented here by

$$\{ X_k | k=0,1,2,\dots,N-1 \}$$

$\{X_k\}$  was then transformed by means of the Fast Fourier Transform algorithm (c.f. Cooley and Tukey, 1965) to yield the finite Fourier transform

$$(2.1) \quad A_n = \frac{1}{N} \sum_{k=0}^{N-1} x_k e^{-2\pi i k n / N} \quad n=0,1,\dots,N-1$$

The raw power-spectral estimate was then calculated by

$$(2.2) \quad I_X(\omega_n) = \frac{N}{2\pi} |A_n|^2$$

Note that although not explicitly shown, this spectral estimate was always normalized and re-coloured, according to what preparatory steps had been carried out on the time series. To obtain a spectral estimate whose variance goes to zero with increasing  $N$ , the raw estimate was convolved with a normalized Parzen window (c.f. Jenkins, 1961) given by

$$(2.3) \quad W(\omega_n, M) = \frac{3M}{4\pi} \left\{ \frac{\sin(\omega_n M/4)}{\omega_n M/4} \right\}^4$$

The resulting convolved quantity

$$(2.4) \quad S_X(\omega_n) = \sum_{m=-M}^M W(\omega_n, m) I_X(\omega_{n-m})$$

was defined as the smoothed spectral estimate. It should be noted here that a variable-window-width technique was used in the spectral convolution. The importance of a stable spectral estimate was given priority over detailed resolution, and consequently the value of  $M$ , which represents an effective window width, was made a monotonic increasing function of frequency. Furthermore, this varying window was applied along the spectrum not at each  $\omega_n$ , but in such a manner that adjacent windows intersected at their equivalent band-widths. This resulted in relatively independent smoothed spectral estimates of decreasing variance evaluated at a limited number of frequency 'bands' of increasing width. Figure III-1 illustrates a raw power spectral estimate (normalized) and its smoothed form obtained by convolution with the Parzen window of varying width. Illustrated also are the extent of overlap between adjacent windows, and the change of window shape from low to higher frequencies.

Smoothed cross-spectral estimates were obtained in a completely analogous manner, and these auto- and cross-spectra, evaluated for a number of events, were statistically dealt with in subsequent analysis.

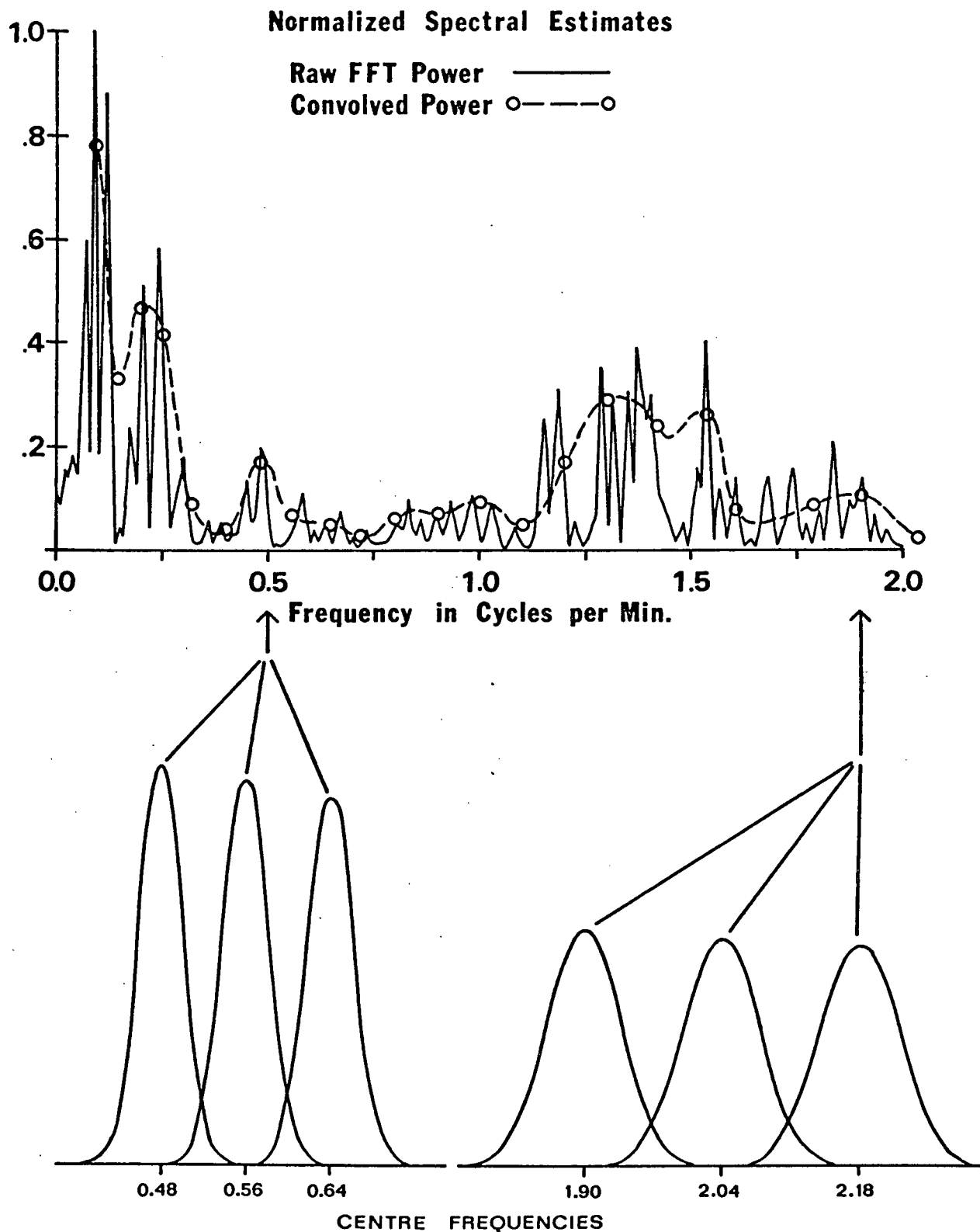


Fig. III-1. The spectral estimate of the raw FFT power, and the smoothed FFT power obtained by convolution with a Parzen window.

## B. Maximum Entropy Method

The standard methods of spectral estimation such as the periodogram (c.f. Jones, 1965) and the autocorrelation approach (Blackman and Tukey, 1958) result in questionable accuracy whenever periods analyzed are comparable to sampled data lengths. Not only do the necessary assumptions of either data-length periodicity or zero-extension of data become suspect, but also, the window functions, required to obtain a stable spectral estimate from finite data sets, introduce spectral shifts, spectral leakage, and smear resolution.

Often in geomagnetic depth-sounding, only limited simultaneous data are available for a group of recording sites. Consequently, if spectral estimates of long-period variations (such as daily harmonics) are desired, such short data sets are unsuitable for analysis by conventional spectral techniques. A newer, nonlinear method appropriate to the analysis of short records, especially those containing narrow spectral peaks, is the Maximum Entropy Method (MEM) first proposed by Burg (1967, 1968). It is described by Lacoss (1971) as a "data-adaptive" method in that it assumes neither a null nor a periodic extension, but adapts itself to the sample of the process analyzed in such a way that the spectral estimate displays maximum entropy or "information content", while still fully agreeing with the available data (McGee, 1969).

A detailed derivation of the MEM algorithms can be found in Barnard (1969), McGee (1969), and Lacoss (1971), whereas a more qualitative outline is given by Ulrych (1972). In summary, it is shown that for a discrete stochastic process with unit sampling, an estimate of the power can be written

$$(2.5) \quad P_B(f) = \frac{P_{M+1}}{\left| 1 + \sum_{k=1}^M a_{Mk} e^{-i2\pi f k} \right|^2}$$

where  $P_B$  = the Burg power spectral estimate

$P_{M+1}$  = mean output power of the  $(M+1)$  - point  
prediction-error filter with  $a_{M0} = 1$

$\{a_{Mk} | k=1, \dots, M\}$  = the prediction-error-filter  
coefficients given by the matrix equation (2.6)

$$(2.6) \quad \begin{bmatrix} \phi_0 & \phi_1 & \dots & \phi_M \\ \phi_1 & & & \vdots \\ \vdots & & & \phi_1 \\ \phi_M & \dots & \phi_1 & \phi_0 \end{bmatrix} \begin{bmatrix} 1 \\ a_{M1} \\ \vdots \\ a_{MM} \end{bmatrix} = \begin{bmatrix} P_{M+1} \\ 0 \\ \vdots \\ 0 \end{bmatrix}$$

where  $\phi_0, \phi_1, \dots, \phi_M$  are estimates of the autocorrelations of the process.

Hence, to numerically obtain  $P_B$ , the prediction-error-filter coefficients must first be determined from (2.6), which presumes a knowledge of the  $(M+1)$  autocorrelation functions. Burg (1968) devised a recursive technique, based on minimizing the average power of the generated prediction-error filter, which, without invoking zero extension of data, allows not only the estimation of the correlation matrix, but also the direct evaluation of the filter coefficients. It should be noted that the actual power is proportional not to the amplitude but to the area of the narrow MEM peak.

Tests on synthetic data (c.f. Ulrych, 1972) indicate that the MEM method is extremely successful in the resolution of discrete frequency components for limited data. However several questions still remain unanswered. For one, the optimum number of filter coefficients generated appears to be data dependent, and since no estimate of 'equivalent

degrees of freedom' or 'asymptotic variance' has yet been established, no quantitative measure of validity can be associated with the various MEM spectral estimates. For another, it appears that the MEM technique tends to 'over-resolve'; i.e. power which is continuous over a wider frequency band is still relegated to discrete frequencies.

A predictive filtering technique, here referred to as the Maximum Entropy Prediction (MEP) method, has recently been proposed by Ulrych et al. (1973). Prediction-error-filter coefficients are generated as in the MEM method, but instead of evaluating  $P_B$  directly from equation (2.5), a N-point least-squares prediction filter for unit prediction distance (c.f. Peacock and Treitel, 1969) is evaluated from the  $a_{Mk}$ 's. The prediction filter is then run over not only the actual data but also over the predicted time series four or five times the original data length. The periodogram of the extended series, evaluated as shown in (2.1) and (2.2), compares very closely with the raw Burg power obtained in the MEM method (Ulrych et al., 1973). The advantage of the MEP method lies in the facts that: 1) the amplitude of spectral peaks give actual power levels, allowing a more direct comparison with standard techniques; (This closer parallel to standard methods may allow an easier formulation of 'equivalent variance' for the MEP approach.) 2) both amplitude and phase spectra can be evaluated; this naturally allows filtering, especially sharp band-pass or band-reject filtering, on the MEP spectral estimate.

The resolution capability of the MEM and the MEP techniques are self-evident in Figure III-2. The spectra illustrate daily harmonic components of a 60-hour (360 points) data section recorded during a magnetically quiet period. No smoothing window was applied to the standard periodogram, but a null extension of four times the data length was used.



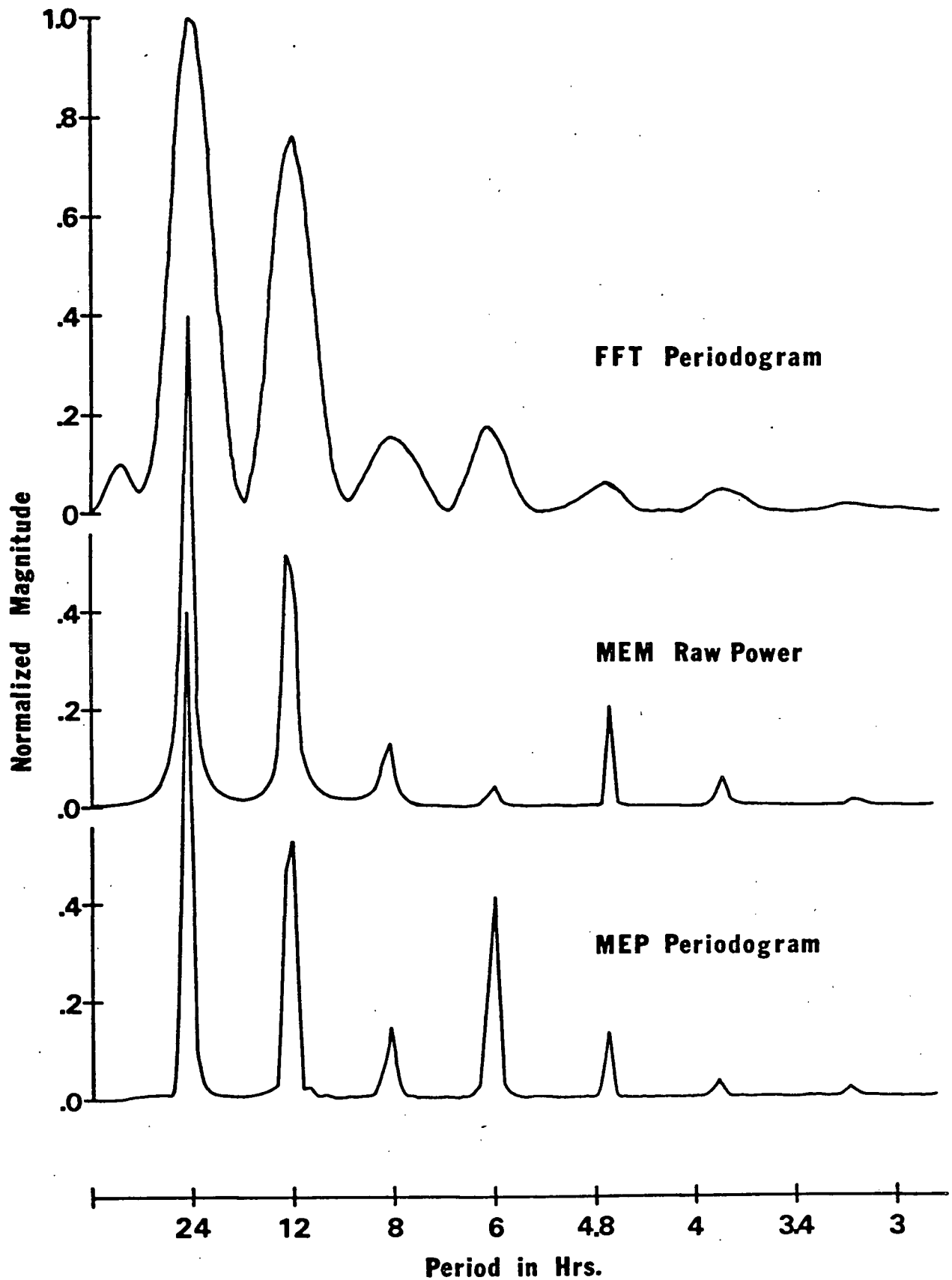


Fig. III-2. Estimates of the raw spectral power of a 60-hour magnetically quiet record obtained by using the conventional periodogram, the MEM, and the MEP techniques.

The MEM estimate, based on 180 filter coefficients, shows the expected narrow peaks. (It is the area under these peaks which is representative of the power.) The MEP estimate, based on a predicted series five times the length of the original, is almost identical to the MEM estimate, and its peaks may be directly compared to those of the conventional FFT periodogram.

It is obvious that for limited data the amplitudes and phases of the discrete daily harmonics can be determined with greater clarity by the use of the MEP technique. This method was subsequently employed in an attempt to gain diurnal variation information from relatively short records.

### 3. *Transfer Function Techniques*

#### A. Outline of Derivation

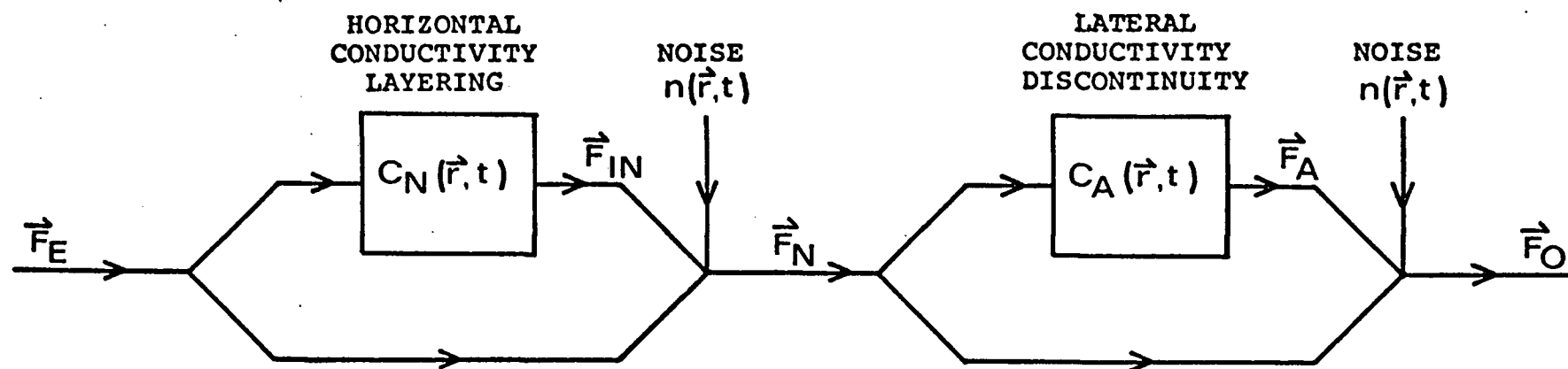
The total time-varying magnetic field observed at the earth's surface can be considered in terms of the constituent parts defined in the schematic diagram of Figure III-3. The prime objective of analysis is to separate  $\vec{F}_N$ , and its perturbation,  $\vec{F}_A$ , determine their spatial and frequency dependence, and subsequently interpret these in terms of conductivity structures. In this perturbation type approach, the basic equation for the interpretation of induction anomalies is (Schmucker, 1970)

$$(3.0) \quad \nabla^2 \vec{F}_A + \frac{\nabla \sigma_A}{\sigma_N + \sigma_A} \times (\nabla \times (\vec{F}_N + \vec{F}_A)) = i\omega\mu \left\{ \sigma_N \vec{F}_A + \sigma_A (\vec{F}_N + \vec{F}_A) \right\}$$

where  $\sigma_N$  = the constant normal conductivity of a certain subsurface layer.

$\sigma_A$  = the variable anomalous conductivity of the layer.

The observed field,  $\vec{F}_N + \vec{F}_A$ , satisfies the basic differential equation for  $\vec{F}$  below the earth's surface



$\vec{F}_E$  = External source field variations.

$\vec{F}_{IN}$  = Internal field variations due to induction in horizontal conductivity layering.

$\vec{F}_N = \vec{F}_E + \vec{F}_{IN}$  = The normal time-varying field observed over a region of laterally homogeneous conductive structure.

$\vec{F}_A$  = The perturbations of the normal field due to lateral conductivity inhomogeneities.

$\vec{F}_O = \vec{F}_N + \vec{F}_A$  = The total observed field variations.

( all fields are functions of  $\vec{r}$  and  $t$  )

Fig. III-3. Schematic diagram indicating the fields contributing to the observed magnetic field variations.

$$(3.0a) \quad \nabla^2 \vec{F} + \frac{\nabla \sigma}{\sigma} \times (\nabla \times \vec{F}) = i\omega\mu\sigma \vec{F}$$

while the normal field,  $\vec{F}_N$ , satisfies the diffusion equation

$$(3.0b) \quad \nabla^2 \vec{F}_N = i\omega\mu\sigma_N \vec{F}_N$$

within the given subsurface layer.

Under the assumptions of a uniform source, these governing relations for  $\vec{F}$  imply that a postulated correlation between  $\vec{F}_A$  and  $\vec{F}_N$  is necessarily linear. Hence, to statistically relate the anomalous to the normal field, the following equation is formulated (Schmucker, 1970) usually in the complex Fourier domain

$$(3.1) \quad \begin{bmatrix} H_A \\ D_A \\ Z_A \end{bmatrix} = \begin{bmatrix} h_H & h_D & h_Z \\ d_H & d_D & d_Z \\ z_H & z_D & z_Z \end{bmatrix} \begin{bmatrix} H_N \\ D_N \\ Z_N \end{bmatrix} + \begin{bmatrix} \delta_H \\ \delta_D \\ \delta_Z \end{bmatrix}$$

i.e.  $\bar{F}_A = T \bar{F}_N + \bar{\Delta}$

where  $T$  = the transfer function matrix of 9 complex elements.

$\bar{\Delta} = (\delta_H, \delta_D, \delta_Z)$ , the transform of a residual containing uncorrelated parts of the anomalous component. Such a residual is necessary since both the normal and the anomalous fields can only be approximated.

$\bar{F}_A = (H_A, D_A, Z_A)$ , the transform of the anomalous field.

$\bar{F}_N = (H_N, D_N, Z_N)$ , the transform of the normal field.

The quantities of equation (3.1) should actually be double transforms, i.e. quantities in the wavenumber-frequency domain. Hence, the elements of matrix  $T$  are dependent on frequency and on a wavenumber vector  $\vec{k}$ ,

which in effect describes a quasi-stationary spatial modulation (Schmucker 1970a) and is *not* the wavenumber of a true electromagnetic wave propagating at the speed of light. To allow the formulation (3.1), consider the elements of (T) to be frequency dependent only. Then deriving an optimum T in the least-squares sense is equivalent to minimizing the power of the residual  $\bar{\Delta}$ , that is, demanding that there be no coherence between  $\bar{F}_N$  and  $\bar{\Delta}$ . This leads to the spectral relation

$$(3.2) \quad \begin{bmatrix} S_{AHN} & S_{ADN} & S_{AZN} \\ S_{DAH} & S_{DAD} & S_{DAZ} \\ S_{ZAH} & S_{ZAD} & S_{ZAZ} \end{bmatrix} = T \begin{bmatrix} S_{HNN} & S_{HND} & S_{HNZ} \\ S_{DNN} & S_{DND} & S_{DNZ} \\ S_{ZNN} & S_{ZND} & S_{ZNZ} \end{bmatrix}$$

or  $P_{AN} = T P_{NN}$

where the  $S_{XY}$ 's are the smoothed cross-power estimates for the X,Y components, and  $P_{AN}$  and  $P_{NN}$  can be considered as spectral matrices.

The solution of equation (3.2) forms the basis of the Transfer Function Matrix (TFM) technique. (See Appendix II for the computational methods of evaluating T.) As formulated, this method linearly relates the anomalous field to the normal field allowing for arbitrary variations in inducing field directions and for coherencies between components of the normal field, but not taking source field wavelengths into account.

In the determination of the single-station vertical transfer function (Cochrane and Hyndman, 1970), here referred to as the Z-Transfer Function (ZTF) technique, only the vertical anomalous component is analyzed and the following assumptions are made:

- (i) there is no long term correlation between normal components;

$$\text{i.e. } S_{HND} = S_{HNZ} = S_{DNZ} \approx 0 \text{ when averaged over time.}$$

(ii) induction is primarily by the horizontal field;

$$\text{i.e. } S_{Z_N Z_N} \ll S_{H_N H_N} \text{ or } S_{D_N D_N}.$$

With these constraints, the vector relation (3.1) becomes

$$(3.3) \quad Z_A = Z_H H_N + Z_D D_N + \delta_Z$$

and the matrix relation (3.2) reduces to

$$(3.4) \quad \begin{aligned} S_{Z_A H_N} &= Z_H S_{H_N H_N} + Z_D S_{D_N H_N} \\ S_{Z_A D_N} &= Z_H S_{H_N D_N} + Z_D S_{D_N D_N} \end{aligned}$$

The observed field ( $H_0, D_0, Z_0$ ) is then used instead of an estimated normal field to calculate spectral powers and (3.4) is solved for  $T_Z = (z_H', z_D')$ , the single-station vertical transfer function. (See Appendix II for computational methods used.) Consequently, the ZTF method relates the anomalous vertical component at a single station to the horizontal field at the same station and allows for horizontal induction only, taking neither source field wavelengths nor normal field correlations into account.

## B. Practical Limitations of Analysis Techniques

### (i) The Problem of Source

Both transfer function techniques as formulated cannot deal directly with source correlations. If a source is localized such that it will appear non-uniform to the stations of a profile, the nature of the induced currents will be largely determined by the source dimensions. Past work

(Caner et al., 1967; Madden and Swift, 1969; Cochrane and Hyndman, 1970; Porath et al., 1970) has indicated a spatial wavelength of over 1000 km can be expected for periods of over 30 minutes. For shorter periods, wavelengths of less than 1000 km are probable and values of coherence between similar components from station to station must be used to estimate spatial uniformity.

Furthermore, if a source is non-random in that it shows a persistent direction or orientation (c.f. Rostoker, 1966), the correlations of such a systematic source field cannot be separated from those attributed to internal current patterns. Fortunately, observations have shown (e.g. Hyndman and Cochrane, 1971) that in some areas the external geomagnetic variations can be considered quasi-random, with source field parameters changing randomly such that a time-average of coherencies between normal components will approach zero. If  $H_N D_N$ ,  $H_N Z_N$ , or  $D_N Z_N$  correlations persist, the ZTF formulation breaks down; however, as long as these correlations are consistent for the entire profile, the TFM approach will remain valid.

#### (ii) Ambiguity of the Normal Field

For profile work, a station well-removed from the investigated anomaly is usually used as a reference site and arbitrarily defined as normal. Hence, the paired-station transfer matrix evaluated is only an approximation of the true transfer function matrix, since the reference location could still be affected by the anomaly in question or have its own anomalous nature, or indeed have a different normal field due to a change in the regional horizontal conductivity structure.

To illustrate the problem of using an arbitrary reference site as normal, consider relation (3.1) in terms of the total transfer function matrix  $T$  and with a zero residual. Setting  $\bar{F}_A = \bar{F}_0 - \bar{F}_N$  yields

$$(3.5) \quad \bar{F}_0 = (T+I) \bar{F}_N = T \bar{F}_N$$

where  $I$  = the identity matrix

If station 1 is the 'anomalous' station and station 2 is relegated to 'normal', the equation which the data are submitted to is

$$(3.6) \quad \bar{F}_1 = T_{12} \bar{F}_2$$

where  $T_{12}$  will be the calculated total transfer function relating  $\bar{F}_1$  and  $\bar{F}_2$ . But for each station equation (3.5) holds

$$(3.7) \quad \bar{F}_1 = T_1 \bar{F}_N \text{ and } \bar{F}_2 = T_2 \bar{F}_N$$

where  $T_1$  is the true total transfer matrix relating the observed to the normal field at station 1, and  $T_2$  is the transfer matrix relating the anomalous field at station 2 to the normal field at station 1. Consequently from (3.6) and (3.7)

$$(3.8) \quad T_{12} = T_1 T_2^{-1}$$

Hence, only when  $T_2$  is equivalent to the identity matrix, i.e., station 2 has *no* anomalous nature and the normal field is the same for both stations, will the calculated paired-station transfer matrix be equivalent to the true transfer matrix at an anomalous station.



In practice, by first examining the data with a single-station technique such as the ZTF method or Parkinson induction arrows (Parkinson, 1962), it is possible to establish a reference site with minimum anomalous vertical field. Although this does not assure that the reference field is truly representative of the regional normal field, it minimizes the possible anomalous contribution of  $T_2$  to  $T_{12}$ . Furthermore, for a random uniform source field, the contributions of  $T_2$  to  $T_{12}$  due to differences in the normal field will be restricted to the diagonal elements of  $T_{12}$  and lie within theoretically definable bounds.

(iii) The Direction of Inducing Fields and the ZTF Technique

As pointed out previously, the TFM method allows for variations in the direction of the inducing field; however the more commonly used ZTF method is based on the assumption of horizontal induction. The following brief argument will show how the vertical transfer function,  $T_z$ , may be biased by vertical induction.

As outlined before, for single-station transfer functions, the data are fitted to the relation

$$(3.9) \quad Z_A = z_H' H_0 + z_D' D_0$$

where *observed* field components are used. Substituting

$$H_0 = H_N + H_A \text{ and } D_0 = D_N + D_A$$

and using the more general matrix equation (3.1) to express the anomalous components in terms of the normal field and the matrix elements of  $T$ , equation (3.9) becomes

$$(3.10) \quad Z_0 = z_H' (H_N + h_H H_N + h_D D_N + h_Z Z_N) + z_D' (D_N + d_D D_N + d_H H_N + d_Z Z_N)$$

Examining equation (3.10) reveals that parts of  $H_0$  that correlate with  $Z$  could be due to the orthogonal cross-terms  $h_D D_N$  and  $h_Z Z_N$  (similarly for parts of  $D_0$ ), but under the simple formulation of single-station transfer functions, these cross-term contributions are absorbed in the  $(z_H', z_D')$  terms.

The critical question remaining is the relative magnitude of the terms in equation (3.10). If an anomalous area is viewed as a local perturbation of the horizontal conductivity structure, then  $Z_N$  will be much smaller than  $H_N$  or  $D_N$  (Price, 1962) and any anomalous vertical field will be primarily due to induction by the horizontal field. If, however, an anomalous area is viewed as the region marking the edge of a plane laminar conductor (Bullard and Parker, 1968; Edwards et al., 1971; Ashour, 1971), then the large enhancement of the vertical field near the edge of the sheet conductor can be attributed to a current flow induced by vertical field variations over the entire sheet. The magnitude of such a current would depend directly on the area of the sheet conductor whereas its direction would generally be determined by the local geometry of the sheet edge.

The validity of the single-station transfer function can be theoretically estimated through the relation deduced below.

By comparing equation (3.10) with the relation

$$(3.11) \quad Z_0 = z_H H_N + z_D D_N + (z_Z + 1) Z_N$$

(obtained from the matrix formulation (3.1)), and assuming that the normal components are independent, it follows that

$$\begin{aligned}
 (3.12) \quad z_H &= z_H' (1 + h_H) + z_D' d_H \\
 z_D &= z_D' (1 + d_D) + z_H' h_D \\
 z_Z &= z_H' h_Z + z_D' d_Z - 1
 \end{aligned}$$

From (3.12), the components  $(z_H', z_D')$  can be expressed as follows

$$\begin{aligned}
 (3.13) \quad z_H' &= \frac{d_Z z_H - d_H (z_Z + 1)}{d_Z (1 + h_H) - d_H h_Z} \\
 z_D' &= \frac{h_Z z_D - h_D (z_Z + 1)}{h_Z (1 + d_D) - h_D d_Z}
 \end{aligned}$$

It is obvious that the relationship between  $(z_H', z_D')$  and  $(z_H, z_D)$  is far from simple if all elements of  $T$  are significant. If the anomaly investigated is due to a simple two-dimensional lateral conductivity discontinuity, then new reference coordinate axes may be found (perpendicular and parallel to conductor strike) such that  $h_D = d_H = 0$ , and (3.13) will simplify to

$$\begin{aligned}
 (3.14) \quad z_H' &= \frac{z_H}{(1 + h_H)} \\
 z_D' &= \frac{z_D}{(1 + d_D)}
 \end{aligned}$$

If equation (3.14) holds for observed data, it follows that the formulation assumptions for the ZTF technique apply and the anomaly is effectively two-dimensional. However in practice, the facts that  $T$  is only approximated by a paired-station transfer matrix and that both the computations of  $T$  and  $T_Z$  are statistical, usually entailing large deviations, add sufficient ambiguity to make a direct comparison of  $T$  and  $T_Z$  inconclusive.

#### (iv) Complexity of Lateral Conductivity Discontinuities

In many places where the ZTF assumptions hold and the conductivity anomaly is effectively two-dimensional, the simpler single-station formulation has been convincingly justified by numerical modelling techniques which provide theoretical curves in good agreement with observed data (Wright, 1969; Schmucker, 1970; Hyndman and Cochrane, 1971). On the other hand, proponents of vertical induction have obtained suitable model curves for the 'coast-effect' by considering the ocean as a thin flat sheet bounded by insulating continents (Edwards et al., 1971; Bullard and Parker, 1971; Ashour, 1971). It should be noted here that although the 'plane laminar conductor' concept has been applied so far to only the ocean and the corresponding land-sea interface, there is no *a priori* reason, except perhaps increased complexity, why it cannot be employed to model say a sub-crustal partial melting zone or low-velocity zone of large areal extent but possessing abrupt lateral disruptions.

The simplistic models required for approximate analytical or numerical solutions can obviously be perturbed in two general ways. First, if the horizontal conductivity discontinuity has finite length with detectable 'end-effects', or if the 'thin sheet' has an appreciable thickness, a three-dimensional problem is posed. Analytic solutions (Treumann, 1970; Gretton, 1973) and numerical solutions (Lines and Jones, 1972) have been proposed, but due to their assumptions, are ill-suited to the practical interpretation of magnetic variations data collected along an inland profile. Secondly, the addition of another anomalous structure, whether independent or related to the first structure, complicates the situation beyond present model solutions. Figure III-4 presents, in diagrammatic form, two simple, tectonically plausible

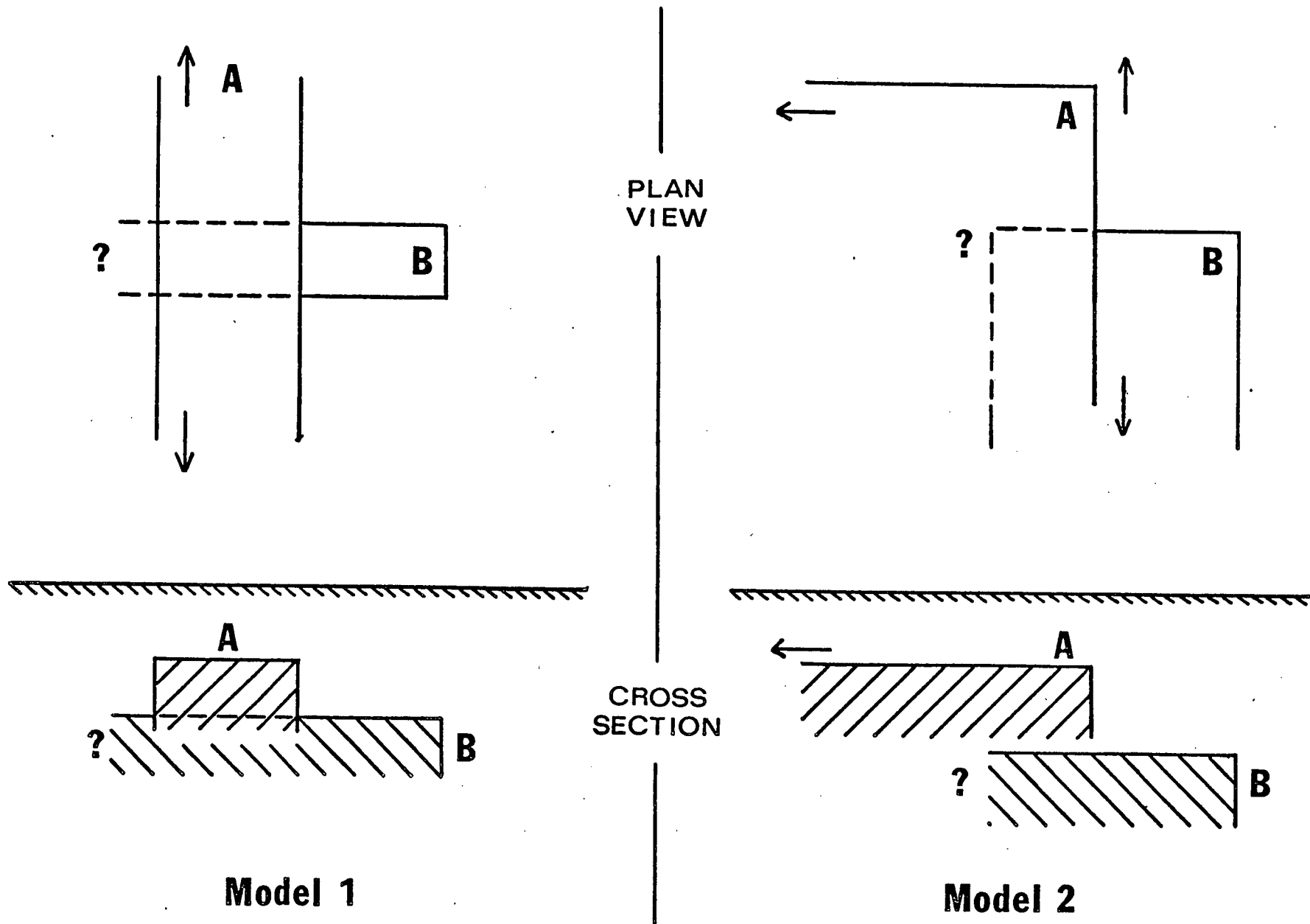


Fig. III-4. Examples of simple 'multiple-anomaly' structures.

conductivity structures. Model 1 is complicated by the fact that conductor B is finite in its strike direction and that B could be either continuous with or merely contiguous to conductor A. A similar ambiguity exists for the relationship of the plate conductors A and B in Model 2. (A configuration similar to Model 2 has been presented by Caner et al. (1971) as a speculative structural model for the intersection of two separate conductive structures in southwestern Canada.)

The ZTF and TFM techniques cannot resolve multiple anomalies; however they can indicate whether or not a two-dimensional model is applicable. In-phase and quadrature induction vectors or induction ellipses (Everett and Hyndman, 1967) can be evaluated from either  $T$  or  $T_z$ . If the directions of the in-phase and quadrature vectors are reasonably concordant and are independent of frequency, a two-dimensional model is adequate. The equivalent condition for the induction ellipse is that it degenerates to a straight line whose direction is independent of frequency.

#### 4. *Conclusions*

The formulations of the paired-station transfer matrix and the single-station transfer function have been reviewed in order to assess the practical scope of each technique. Simple relations expressing the bias contained in each formulation and the analytic dependence between the two formulations have been deduced. The more detailed discussion of technique limitations leads to the following principal conclusion: Although seldom used in the analysis of real data, the paired-station transfer matrix method allows the evaluation of an approximate true transfer matrix, providing information complementary to the single-station transfer function method. It not only permits an assessment of the

validity of the ZTF assumptions, but also provides estimates of vertical and horizontal transfer functions which allow for normal component correlations and arbitrary directions of the inducing field. Hence, for a more comprehensive evaluation of data from an anomalous profile, *both* techniques should be applied.

IV. A FIELD INVESTIGATION OF THE CORDILLERA  
TRANSITION ANOMALY

	Page
1. Introduction	55
2. Description of Field Work	56
3. Data Reduction and Analysis	58
4. Results of Analysis	63
5. Qualitative Interpretation	88
6. Numerical Modelling	93
7. Conclusions and Discussion	97



Fig. IV-1. Aerial photograph of the Rocky Mountain Trench taken above Tete Jaune looking northwest along the Trench. The Rocky Mountains are on the right and the Cariboo Mountains on the left. (Courtesy of the Dept. of Lands, Forest, and Water Resources British Columbia.)



## 1. *Introduction*

The dominant geomagnetic feature for the Canadian Cordillera is the presence of the low-I zone, a region in which vertical variations having periods less than 30 minutes are greatly attenuated compared to variations observed further east. The transition zone where the amplitudes of vertical field fluctuations not only increase sharply but also show strong azimuthal dependence has been found to follow approximately a line along the western front of the Rocky Mountains from 49°N to at least 54°N latitude (Caner et al., 1971). Consequently, it constitutes a large scale inland anomaly, marking a relatively abrupt lateral conductivity change in the lower crust or upper mantle.

Unlike the other anomalous areas in southwestern Canada such as the 'coast-effect' at Vancouver Island (Lambert and Caner, 1965) or the strong 'Kootenay Anomaly' (Lajoie and Caner, 1970), the transition zone has not yet been subject to detailed investigation, and its correlation with the 'inland anomaly' of the western United States (Schmucker, 1964; Reitzel et al., 1970; Porath et al., 1971) has yet to be defined. Also serving to motivate this detailed investigation is the Rocky Mountain Trench (shown in Fig. IV-1). Since the Trench is a major physiographic feature lying within the transition zone, it is natural to speculate on a direct or indirect relation between the origin of both features. However, it must be emphasized that the primary purpose of the field work was not to elucidate this speculation, but to investigate in greater detail the nature of the lateral conductivity changes encountered in this zone.

## 2. *Description of Field Work*

### (i) Instrumentation

Instruments used in the field were of two types:

#### (a) The Askania Geomagnetic Variograph Gv3

This variograph records time variations in the three field components H, D, and Z, using three small, fibre-suspended bar magnets which, along with their optical systems and calibration coils, comprise the three independent variometers. In addition to these three traces, a base-line, an internal temperature level, and hourly time marks (externally controlled) are recorded on continuously advancing photographic recording paper. To ensure that temperature fluctuations remained less than 1°C, a thermostatically controlled heater, which can be set at 10°C to 40°C, is enclosed in the housing. The recording reels, designed and built at the Victoria Magnetic Observatory, allow operation with 60 Hz line power and accommodate 10 m of recording paper. Various chart speeds are available. Employed in this particular project, speeds of 30mm/hr and 60mm/hr provided 7 and 14 days of continuous record with a time scale resolution of about 120 and 60 s respectively. Optimum resolution is between 1 and 2γ, and the dynamic range is about 55 db.

During field operation all Askania variographs were located on stable platforms within weatherproof enclosures which had line-power access. Actual power was delivered to the instruments through a 'converter-battery-charger' configuration in order to provide continuous operation during temporary line failures. A Sprengnether chronometer was used for the control of time marks and also provided a calibrated 60-cycle power supply for the recording reels.

## (b) Broad-Band GDS Systems

This electronic system, developed by Caner and Dragert (1972) is fully described in Section II of this thesis. In summary, it is comprised of a transistorized three-component saturable core magnetometer (Trigg et al., 1971), a system of matched band-pass filters and amplifiers, and a 7-channel slow-speed FM tape recorder. The three magnetic field components are recorded in two overlapping frequency bands (BAND A: DC to 200 s; Band B: 500 s to 5 s) providing a recorded frequency range of 0.01 to 100 mHz. Variable sensitivities for Band B allow a resolution of 0.1 to 0.2 $\gamma$ , and in conjunction with the automatic zero suppression circuits (Trigg, 1970) of Band A, yield a dynamic range of about 80 db for the entire system. Crystal controlled hourly time marks are internally supplied from the fluxgate unit and superimposed on all channels. The seventh channel is used to record WWVB time signals or a reference frequency later utilized in playback for flutter control. The recording speed of 15/160 ips is fixed, allowing a time scale resolution of better than 0.1 s, and a continuous record of 5 days if a standard 10 $\frac{1}{2}$  inch (3600') reel of magnetic tape is used.

During field operation, the fluxgate sensing heads must be buried to minimize temperature effects. The control circuitry and filters are contained in an insulated, weatherproof, custom-made transit case and need no other protection; the tape recorders on the other hand, must be in a dry, above-freezing environment to function according to manufacturer's specifications. For this project, both line power and batteries were used simultaneously to provide continuous power for the system.

### (ii) Location of Profile

A geomagnetic depth-sounding profile of closely spaced stations using the newer broad-band instrumentation as well as the standard Askania variographs was operated for a period of two months during the fall of 1971. The location of the profile is shown in Figure IV-2, and the station identification detail is summarized in Table IV-1. Two shortcomings of this particular profile are obvious: 1) the station spacing is still too large for accurate spatial resolution of possible short-period anomalies; and 2) the nature of the anomaly in this area is suspected to be three-dimensional (Caner et al., 1971), thus possibly precluding a simple two-dimensional solution. However, practical considerations such as suitable instrument protection, accessibility of sites, limited number of broad-band systems, minimization of geomagnetic latitude effects, and complete bracketing of the transition anomaly favoured the chosen profile location.

## 3. *Data Reduction and Analysis*

### (i) Digital Preparation

After preliminary editing of all tapes and films, simultaneous record sections with suitable continuous magnetic activity were chosen for analysis. The Askania film sections were digitized at the Victoria Magnetic Observatory using a digitizing interval of 60.0 s (accurate to better than 1%) and fixed record lengths of 36 hr. The digitized output, punched automatically on cards, consisted of four significant digits which were subject to a digital noise of less than 1 $\gamma$  peak-to-peak.

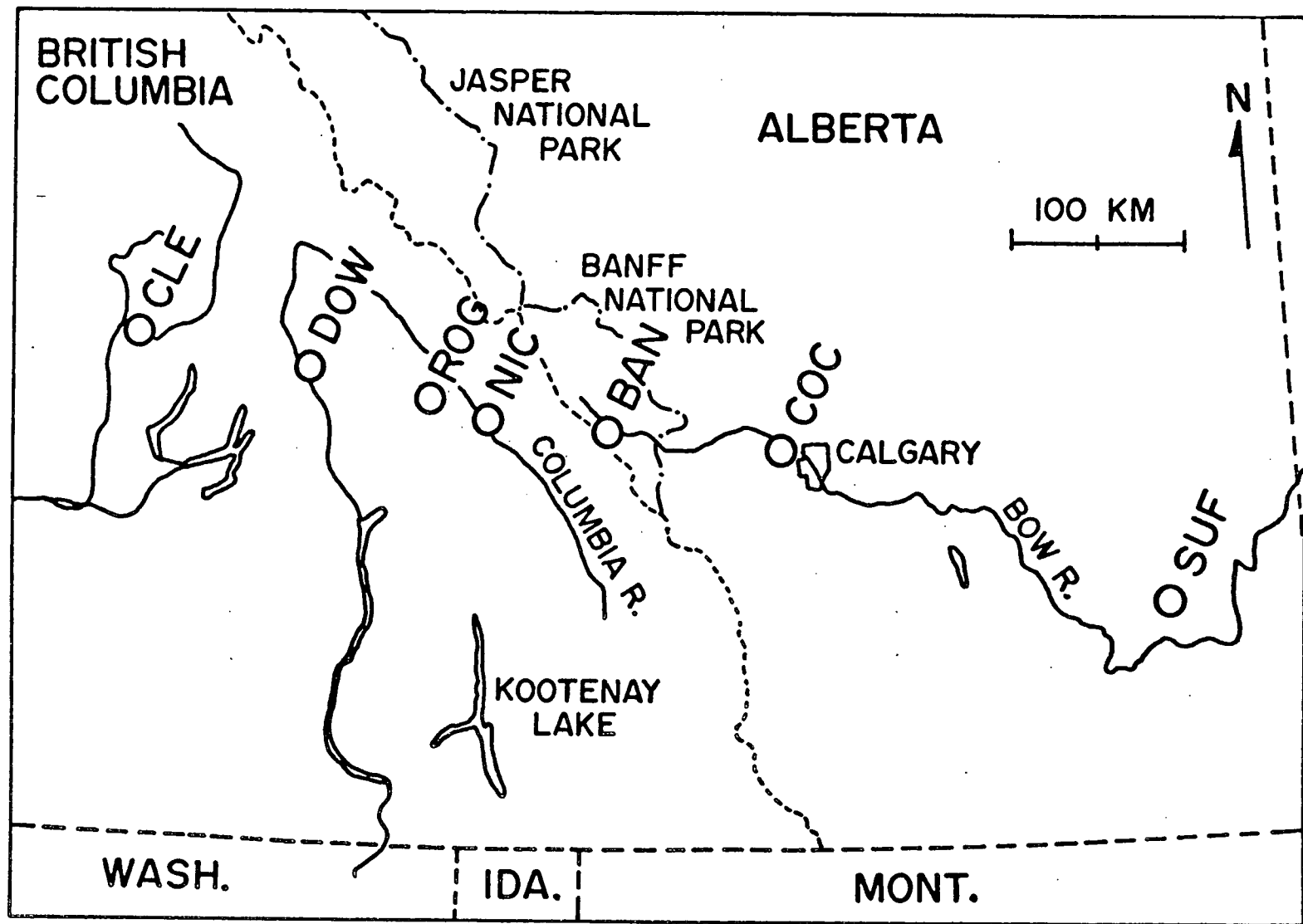


Fig. IV-2. Station locations for the field investigation of the 'transition zone' anomaly.

STATION	GEOGRAPHIC LOCATION LONG.(°W) LAT.(°N)		GEOMAGNETIC LAT.(°N)	TYPE OF INSTRUMENT	TIME OF OPERATION
CLE (Clearwater)	120.0	51.6	57.9	Askania	Aug.23-Nov.16
DOW (Dowie Creek)	118.2	51.3	58.0	Broad-band	Sept.17-Nov.11
ROG (Rogers Pass)	117.6	51.2	58.1	Broad-band	Sept.17-Nov.12
NIC (Nicholson)	117.0	51.3	58.3	Broad-band	Sept.18-Nov.12
BAN (Banff)	115.6	51.2	58.6	Broad-band	Sept.19-Nov.13
COC (Cochrane)	114.2	51.1	58.8	Askania	Sept.20-Nov.15
SUF (Suffield)	111.1	50.2	58.6	Askania	Sept.20-Nov.14

TABLE IV-1. Summary of station identification and locations for the 'transition anomaly' profile.



The magnetic tape records from the broad-band GDS systems were digitized in three overlapping frequency bands using the Interdata Analogue/Digital converter at the Dept. of Geophysics and Astronomy, University of B.C.. To significantly reduce playback noise and aliasing, the analogue signals were low-pass filtered before digitizing. This resulted in a less than 1% combined playback-digital noise level. The digitizing intervals were controlled by a Wave-Tek signal generator with a monitored stability of better than 1 part in  $10^3$ ; random fluctuations in tape-recording and tape-playback speeds reduced this stability to about 1%. The relevant digitizing information is summarized in Table IV-2.

BAND NO.	EFFECTIVE PERIOD RANGE	DIGITIZING INTERVAL	LOW-PASS FILTER CUT-OFF	RECORD LENGTHS	TOTAL NO. OF EVENTS/STATION
1	10-500 s	2.50 s	5.00 s	100 min (2400 points)	12
2	5-180 min	1.00 min	2.00 min	36 hr (2160 points)	7
3	1-12 hr	10.0 min	20.0 min	100 hr (600 points)	3*

\*Record sections for Band 3 were not simultaneous at the 4 broad-band stations and were primarily 'quiet'.

TABLE IV-2 Summary of digitizing information for the broad-band system data. Note that Bands 1 and 2 are equivalent to Bands B and A respectively.

All digitized data were visually inspected using an Adage Graphics Terminal, and obvious digital spikes and stray filter pulses as well as unwanted time pulses and data step-functions were removed. (For details see Appendix I.) These cleaned digital data were then stored on magnetic tape for subsequent numerical analysis.

## (ii) Numerical Methods

## (a) Spectral Analysis

To efficiently handle the large quantities of data, the periodogram spectral approach (c.f. Jones, 1965) utilizing the Fast Fourier Transform (Cooley and Tukey, 1965) was used for spectral analysis of Band 1 and Band 2 events. A variable-width Parzen window (see Section III and Appendix II of this thesis) was used to convolve the raw power periodograms, yielding, as a function of frequency, smoothed independent spectral estimates of decreasing variance at a limited number of frequency bands of decreasing resolution. To further increase spectral stability and to obtain spectral features independent of time, the auto- and cross-power estimates were averaged over all events within each Band (1 and 2) at each station.

The relative component power ratios

$$(P_x)_{\text{STATION}} / (P_x)_{\text{REFERENCE STATION}}$$

where  $X = H, D$ , or  $Z$ , were evaluated from the smoothed spectral estimates to reveal possible latitude effects and to illustrate separately the relative variation of the individual component energies with frequency from station to station. Also the standard impedance ratios or power attenuation ratios (Cander et al., 1967) given by

$$M_H = (P_Z/P_H)_{\text{STATION}} / (P_Z/P_H)_{\text{REFERENCE STATION}}$$

were evaluated. This normalized dimensionless attenuation factor is relatively independent of geomagnetic latitude effects, and its variation with frequency, *in the absence of anomalous fields*, characterizes differences in horizontal conductivity layering.

The severely limited simultaneous data available for Band 3 made a

conventional spectral approach unreliable. Consequently, the magnetically quiet data of Band 3 was examined with the 'Maximum Entropy Prediction' (MEP) technique (Ulrych et al., 1973; see also Section III of this thesis). It was hoped that this high-resolution technique would allow stable estimates of the discrete daily harmonic peaks and thus permit a consistent evaluation of Z/H impedance ratios at periods of 24, 12, 8, and 6 hr.

#### (b) Transfer Function Evaluation

To determine the magnitude and phase of anomalous field contributions, mean single-station vertical transfer function  $T_Z$  (Cochrane and Hyndman, 1970) and mean paired-station transfer function matrices  $T$  (Schmucker, 1970) were evaluated from the averaged spectral estimates for Bands 1 and 2. A measure of confidence was established by evaluating  $T_Z$ 's and  $T$ 's for each individual event and computing their standard deviations from the mean values. (See Section III of this thesis for an outline of the transfer function formulation, and Appendix II for details of the computational methods used.) In addition to a comparison of  $T_Z$  and  $T$  for all stations, induction vectors (Everett and Hyndman, 1967) were determined to illustrate the dominant anomalous effect in a manner concordant with previous work (Caner et al., 1971; Cochrane and Hyndman, 1970), and to allow assessment of the applicability of a two-dimensional model.

### 4. Results of Analysis

#### (i) The MEP Method and Band 3

Of the digitized Band 3 data, only two sections of record, one 60 hours in length and a second 48 hours in length, having 360 and 288 points respectively, were simultaneously recorded at all four broad-band stations without interruption. These two events were analyzed using

the MEP technique with the number of filter coefficients equivalent to 50% data length, and an extended predicted series five times original data length. The results were disappointing in that no uniform spectral estimates of daily harmonics of the Z component could be obtained. However, the inability to arrive at consistent spectral estimates is believed to be rooted not in the analysis technique but in an uncontrolled temperature effect on the fluxgate sensing heads. Strong daily temperature variations will be apparent in recorded data in two ways: 1) the first harmonic (24-hour period) of all components will be more strongly affected than the other harmonics (e.g. Schmucker, 1970); and 2) the increased temperature sensitivity of the Z component ( $\sim 6\gamma/C^\circ$ ) combined with the usual strong attenuation of vertical variations (Price, 1950), will render the recorded Z fluctuations the most erratic. This is indeed the case, as shown by the pattern of amplitudes and phases for the daily harmonic components of the 60-hour event. (See Table IV-3.) Only the harmonics of order 2 or greater for H and D begin to show a more consistent pattern for the four sites. Consequently, meaningful Z/H ratios could not be determined for diurnal variations, limiting subsequent interpretation to the higher frequency bands.

#### (ii) Spectral Results for Bands 1 and 2

Figure IV-3 illustrates sample records for the short-period band recorded at the broad-band stations of the profile. Note that the 'digitizing' classifications of Band 1 and Band 2 are equivalent to Band B and Band A respectively as used by Caner and Dragert (1972), and as used in Section II of this thesis. To maintain consistency, these frequency bands are henceforth referred to by the latter classification. This particular record is dominated by a regular pulsation of H with a

STATION		DOW		ROG		NIC		BAN	
COMPONENT		Amplitude	Phase	Amplitude	Phase	Amplitude	Phase	Amplitude	Phase
		( $\gamma$ )	(degrees)	( $\gamma$ )	(degrees)	( $\gamma$ )	(degrees)	( $\gamma$ )	(degrees)
H	24 hrs	43.2	231	25.4	328	29.3	321	36.0	340
	12 "	33.8	271	25.2	268	34.8	261	34.1	274
	8 "	9.5	77	8.1	68	10.2	64	11.1	84
	6 "	5.1	223	6.2	220	4.5	215	7.7	229
D	24 hrs	36.1	113	27.4	64	26.0	58	21.1	210
	12 "	15.2	13	20.0	23	21.1	15	45.0	13
	8 "	10.4	168	10.8	176	11.3	162	9.5	146
	6 "	13.1	126	17.7	123	21.3	109	21.3	94
Z	24 hrs	5.3	92	1.4	135	0.3	114	3.3	240
	12 "	2.7	343	0.5	18	1.6	312	3.7	288
	8 "	1.4	94	1.2	61	0.9	207	0.8	237
	6 "	1.7	329	2.5	264	0.8	237	1.9	145

Table IV-3. Harmonic peaks and phases for a 60-hour (360 points) 'quiet' record obtained by using the MEP technique. Amplitudes are in gamma and phases are relative to a local time of 03:00 U.T., Oct. 15, 1971.

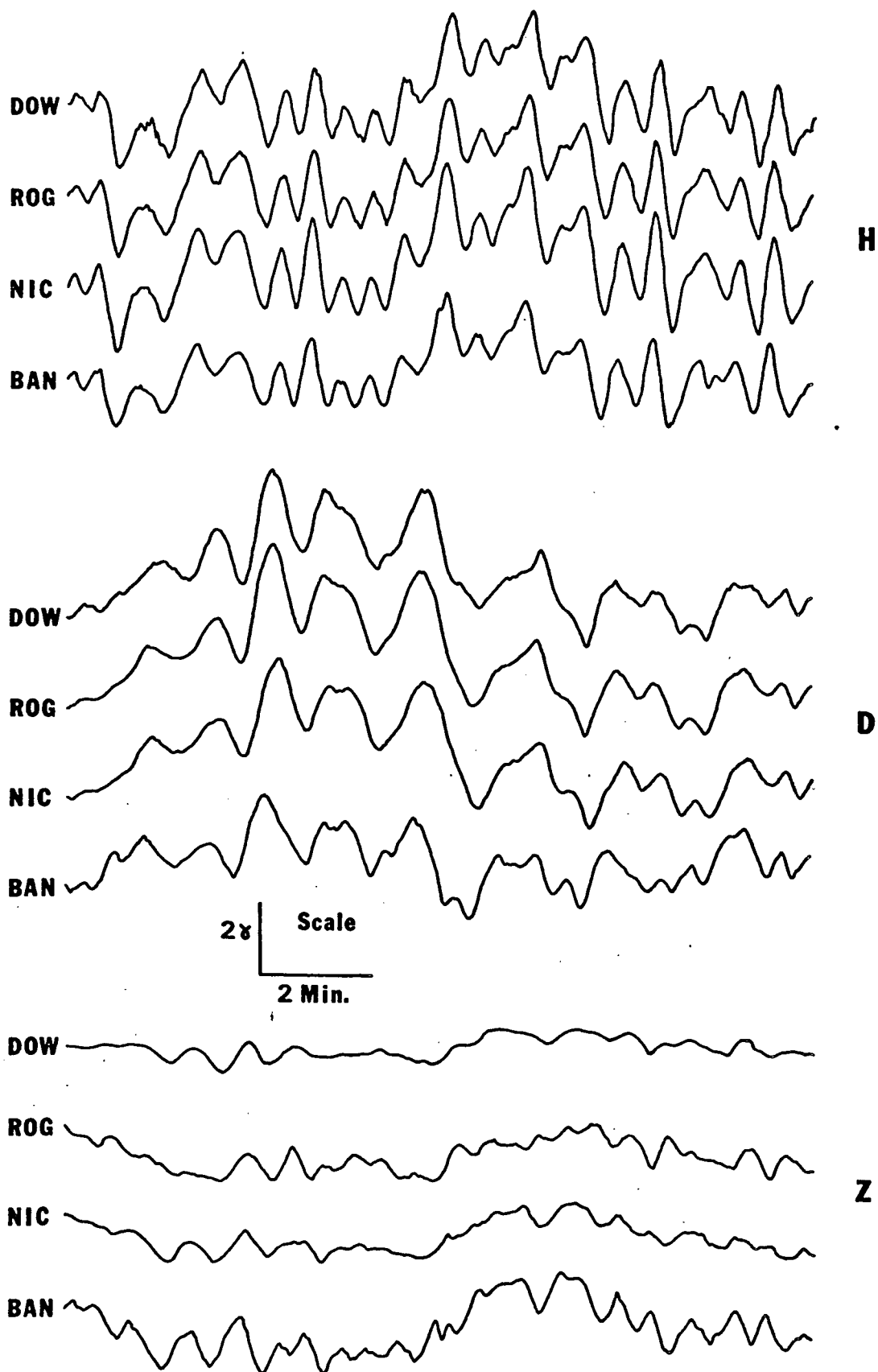


Fig. IV-3. Sample of Band B data recorded at broad-band stations.

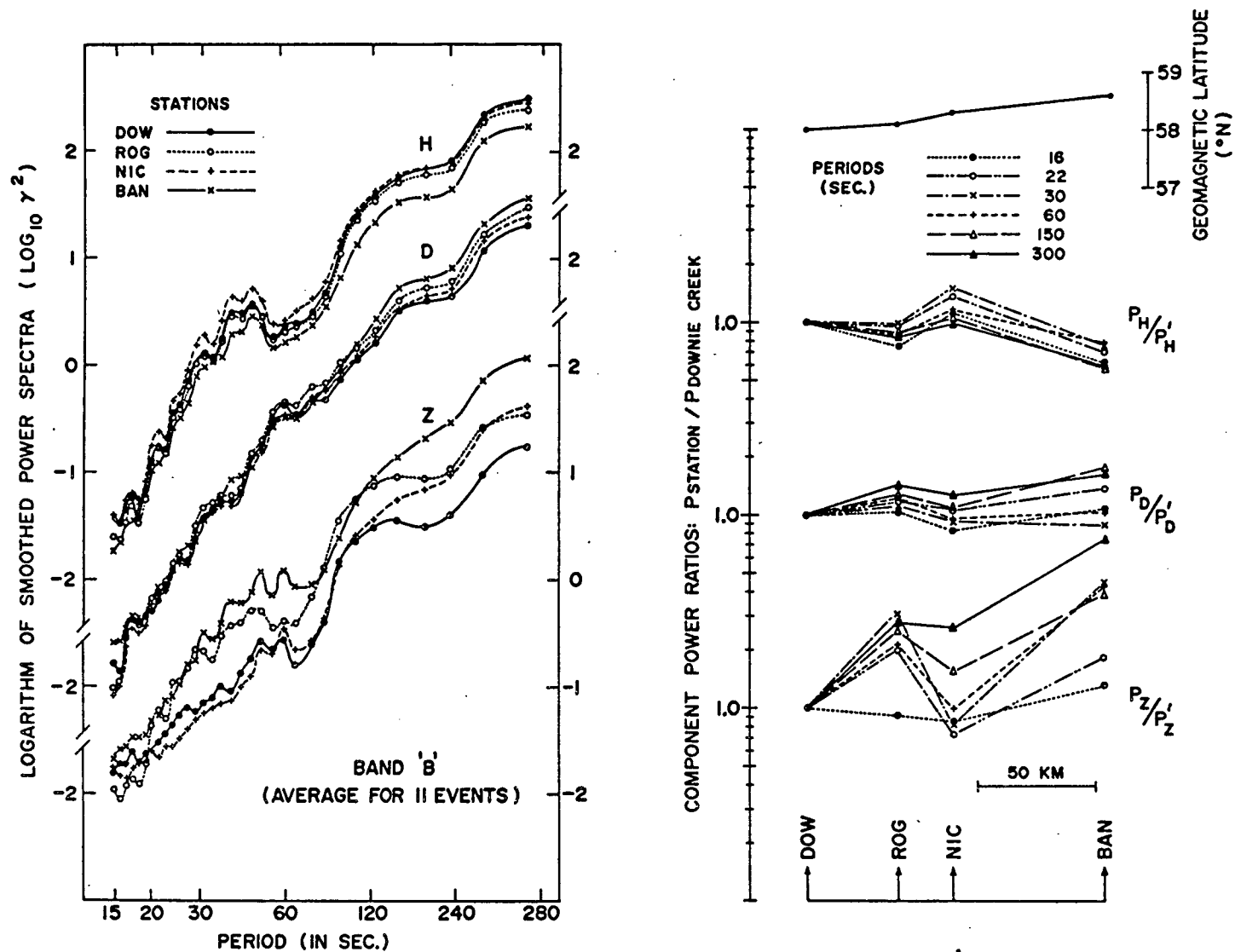


Fig. IV-4. Smoothed spectral estimates for Band B averaged over 11 events. Component power ratios are also shown for selected periods. (Graph of geomagnetic latitude indicates possible latitude effects.)

period of about 44 s. The increased Z-amplitudes and the Z-H correspondence at ROG and especially BAN, as well as the phase differences of Z at ROG and BAN are apparent even from these relatively short samples of data. The presence of anomalous field variations is verified by spectral analysis. Figure IV-4 illustrates the smoothed spectral estimates at the broad-band stations averaged for 11 events, and the component power ratios for these estimates at selected periods. The spectral estimates for individual components track reasonably well suggesting a time-averaged source uniformity over this four-station spread. In addition to the obvious vertical field enhancement at ROG and BAN, an anomalous H contribution is indicated for NIC and a slight reduction of H power is defined for BAN.

A sample of Band A records for the entire profile is shown in Figure IV-5. Worthy of note is the strong attenuation of Z activity at not only the western stations (CLE and DOW) but also the easternmost station, SUF, which lies in an area previously hypothesized to be a high-I region. The expected increase in the amplitude of Z fluctuations at strongly anomalous sites is apparent at BAN and COC; perhaps more striking is a similar strong enhancement of the H and D components at COC. The spatial and frequency dependence of the Band A components is more clearly shown by the spectral estimates and component power ratios for a 36-hour sample event (see Fig. IV-6). Again, good tracking is indicative of source uniformity over the profile for this event. Relative to CLE, the short-period Z power peaks strongly at BAN and COC but is reduced again at SUF. Enhancements of the horizontal components at COC are seen to be quite pronounced while less significant perturbations of D are indicated for ROG and BAN.



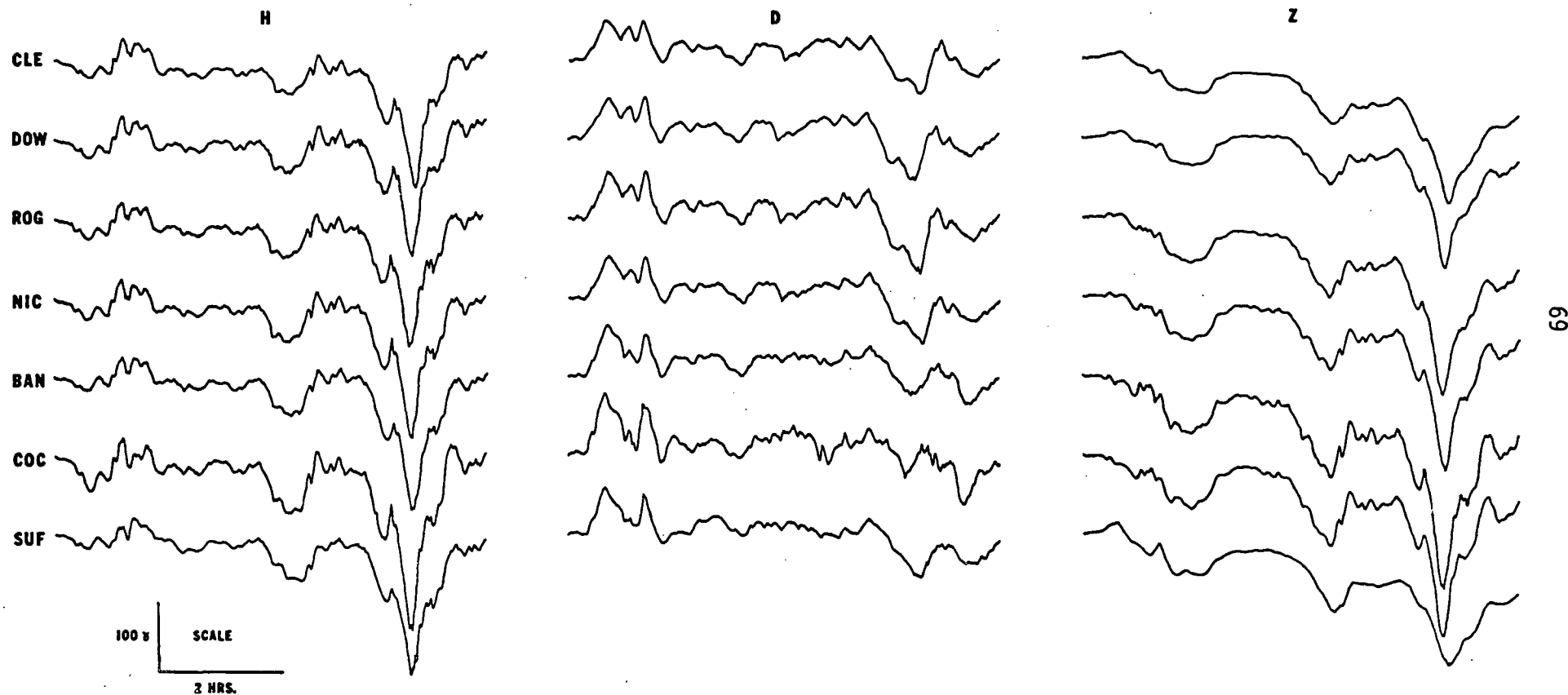


Fig. IV-5. Sample of Band A data recorded at all profile stations.

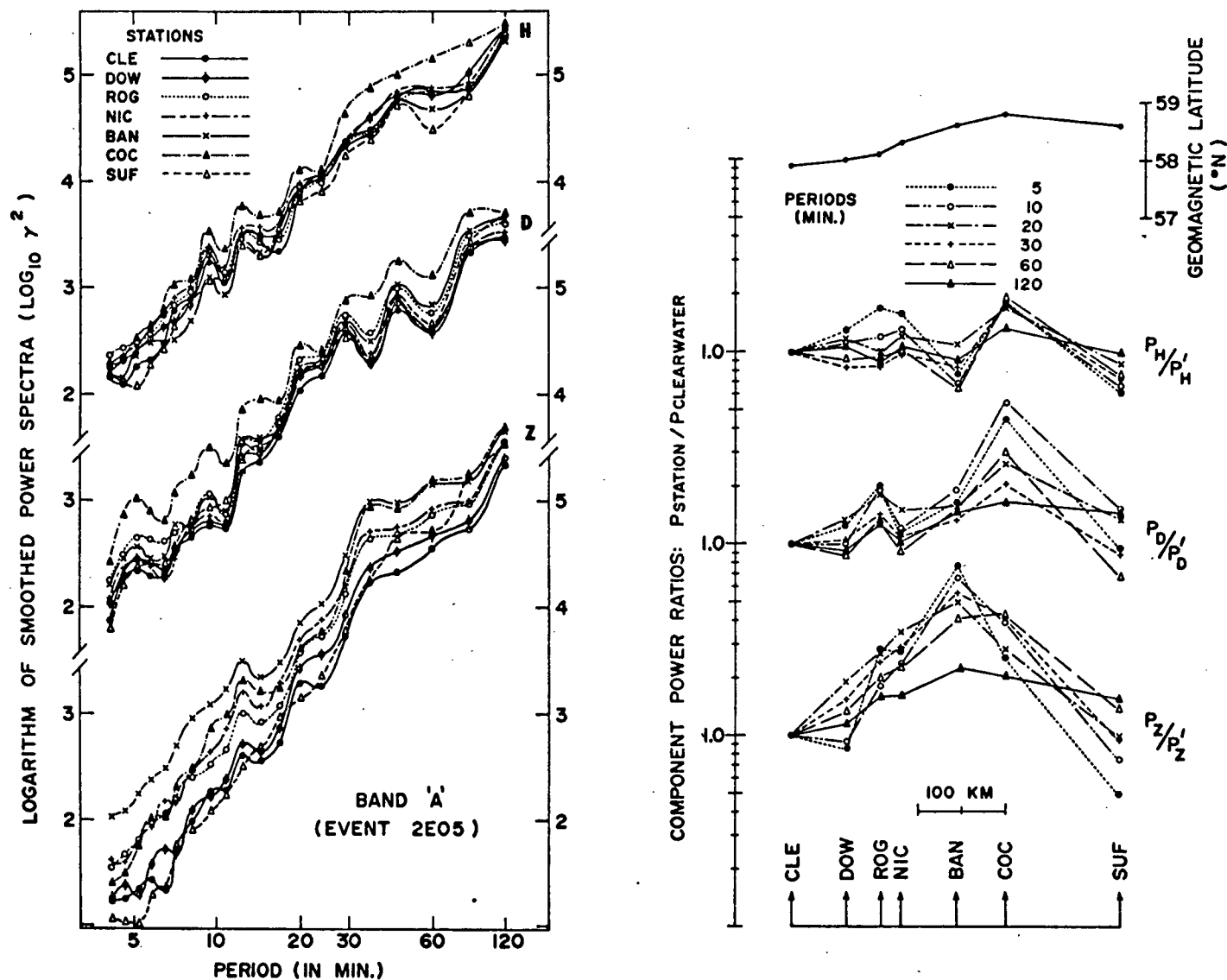


Fig. IV-6. Smoothed spectral estimates for Band A for a sample event of 36 hours. Component power ratios are also shown for selected periods. (Graph of geomagnetic latitude indicates possible latitude effects.)

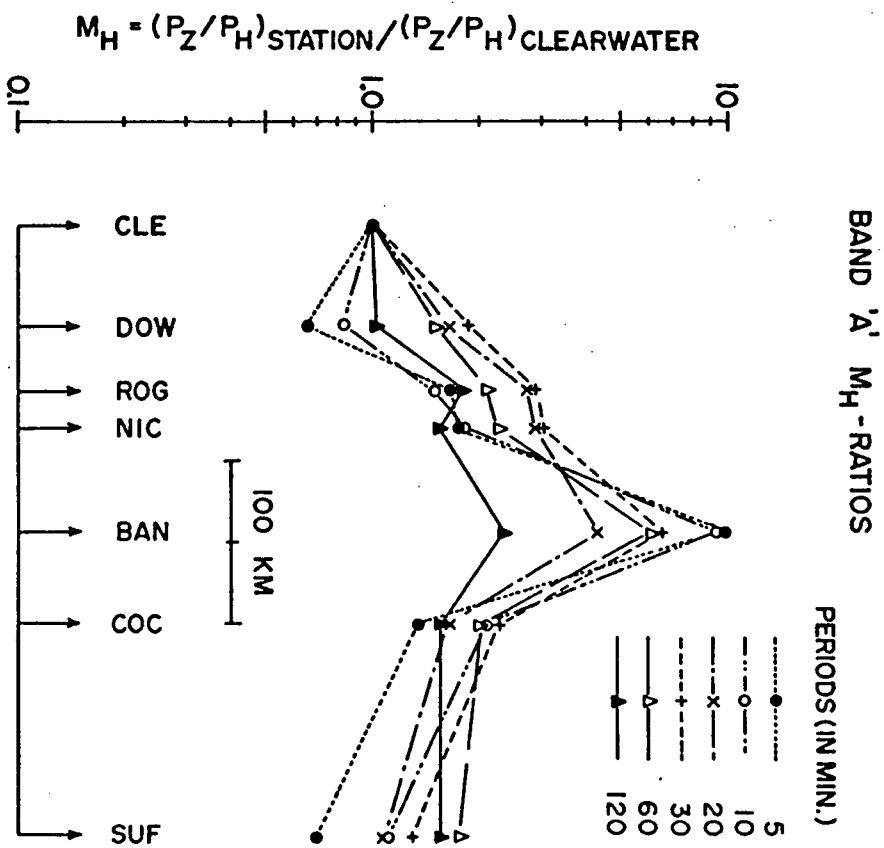
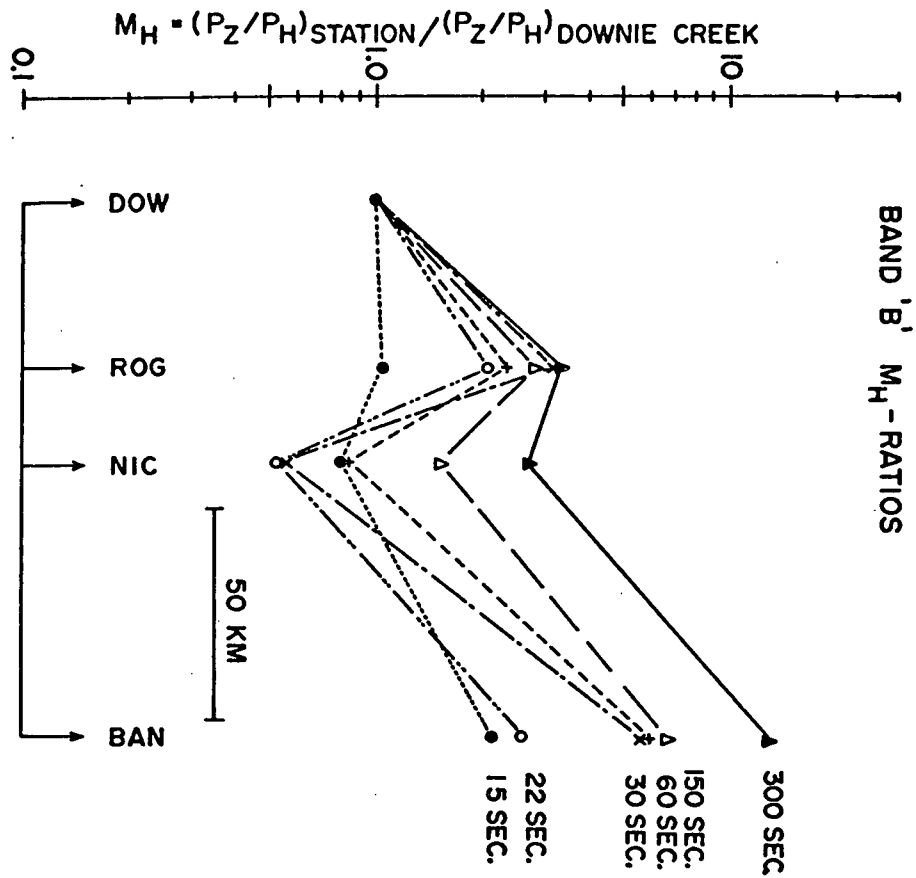


Fig. IV-7. Power attenuation ratios,  $M_H$ , for Bands A and B determined from the spectra illustrated in Fig. IV-4 and IV-6.

From the illustrated spectra for Bands A and B, power attenuation ratios ( $M_H$ ) were also evaluated (see Fig. IV-7). It is obvious that anomalous field contributions dominate; consequently, no valid horizontal-layering model can be deduced from this apparent impedance measure.

### (iii) Single-Station Vertical Transfer Functions

For Band B, mean vertical transfer functions ( $T_Z$ ) were computed using the weighted spectral averages of eleven 100-minute events, each event being normalized with respect to total Z power. (For computation details see Appendix II.) Standard error limits were obtained from the observed scatter in transfer functions computed from individual events. Figure IV-8 illustrates the frequency dependence of the mean in-phase and quadrature components of  $T_Z$  for the short-period band at each station. The general tendency for increased deviations for periods less than 40 s is indicative of possible source non-uniformities. The spatial and frequency dependence of  $T_Z$  is more readily discernable when presented in the form of in-phase and quadrature induction vectors (Fig. IV-9). The features important to subsequent analysis and interpretation are: 1) For sites recording the short-period band, DOW shows the least perturbations and hence is a logical reference site for normal field estimation; 2) A reversal in Z occurs between ROG and BAN, with a corresponding reduction in anomalous Z at NIC; 3) Generally, for increasing period the quadrature components become more significant and a rotation towards the south is apparent for the in-phase components.

Mean  $T_Z$ 's computed for the long-period band were based on the weighted spectral average for four events of 36 hours each, again each event being normalized with respect to total Z power. Figures IV-10 and IV-11 illustrate the amplitudes and directions of the in-phase and quadrature components of  $T_Z$  for Band A, along with their computed standard

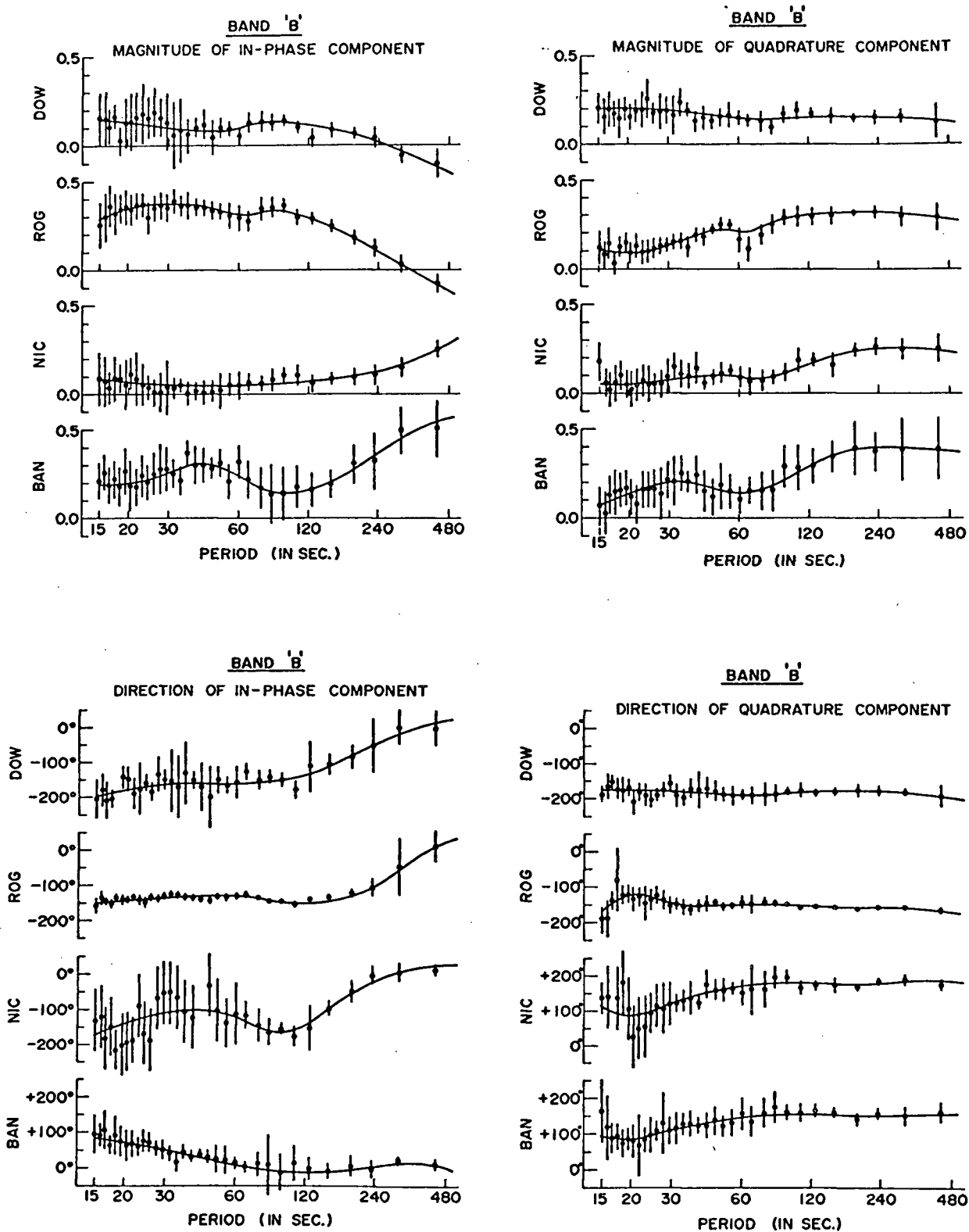
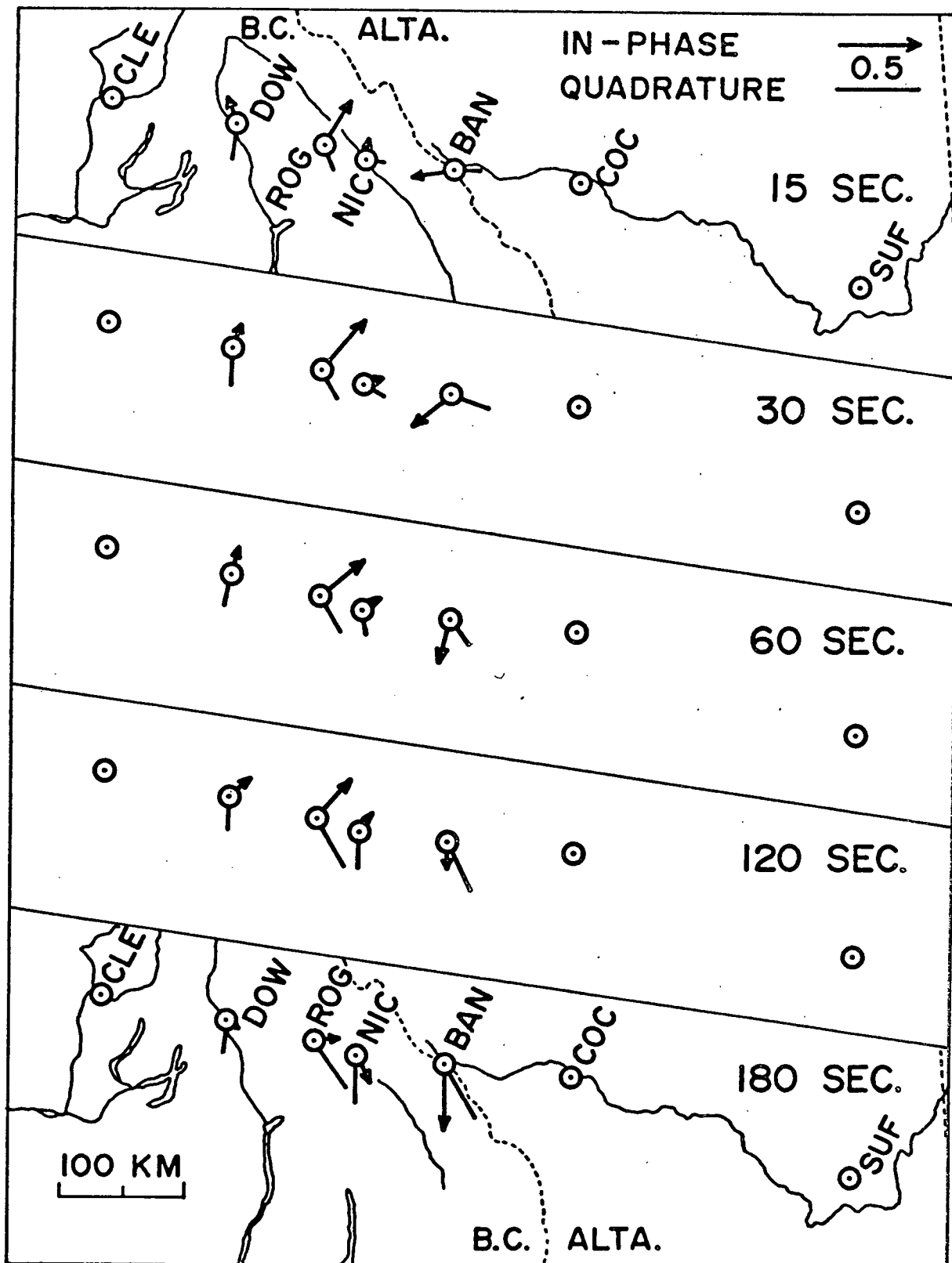


Fig. IV-8. Single-station transfer function amplitudes and directions for Band B. Directions are measured positive east of true north.



## BAND B : SINGLE-STATION INDUCTION VECTORS

Fig. IV-9. Single-station transfer function arrows for Band B.  
The in-phase vectors are negative to follow Parkinson's convention.

deviations. Generally, the curves are well defined and the increased deviations for periods greater than 45 minutes possibly reflect the greater variance (10 to 30%) of the spectral estimates at these frequencies. The in-phase portions of the  $T_Z$ 's appear to peak between 20 and 30 minute periods at all anomalous sites except BAN where the maximum value occurs between 15 and 20 minute periods.

Induction arrows for Band A (Fig. IV-12) clearly reveal the following important features: 1) Minimum anomalous vertical field contributions are observed at CLE and SUF, indicating either as possible candidates for a reference site. Since the western area was considered better known through previous investigations and since a western station (DOW) was chosen as Band B reference, CLE was chosen to represent normal field variations for Band A. It should also be pointed out that the similarity of  $T_Z$  at CLE and SUF is quite striking for two sites more than 600 km apart and supposedly located in quite distinct conductivity regions. 2) No Z reversal is apparent across the transition zone for Band A. 3) The in-phase and quadrature components are comparable in magnitude and their directions tend to diverge with increasing period. 4) The directions of the in-phase components are dominantly south to southwest for all periods.

#### (iv) Paired-Station Transfer Matrices

As expected, it was extremely difficult to obtain stable transfer matrices in the paired-station analysis. From the formulation for  $T$  (see equation 3.2 in Section III), it is obvious that numerical instabilities are introduced when the cross-spectral matrix  $P_{NN}$  approaches a singularity or contains small elements. In either case, the inverse of  $P_{NN}$ , and consequently  $T$ , will be ill-determined. Furthermore,

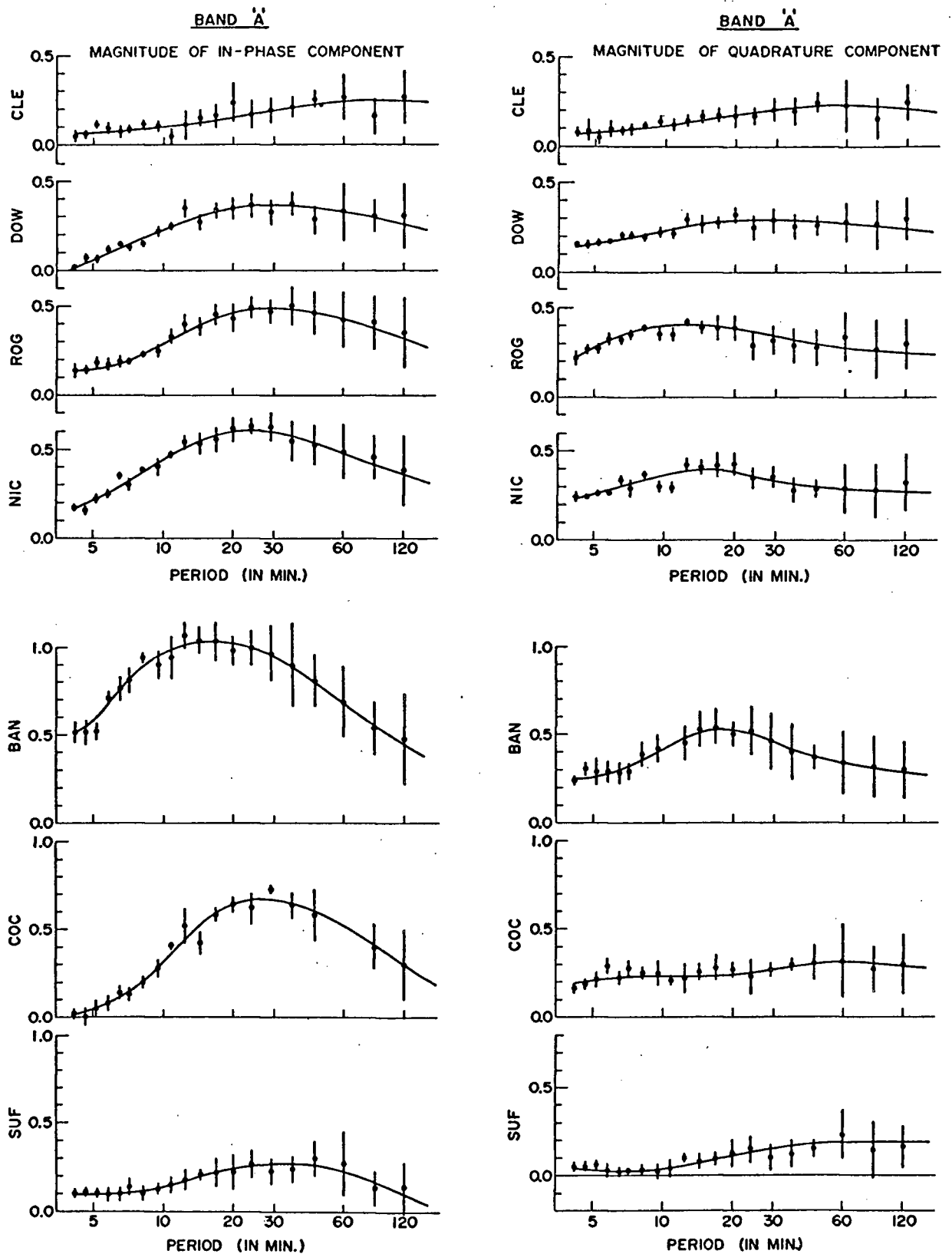


Fig. IV-10. Single-station transfer function amplitudes for Band A.



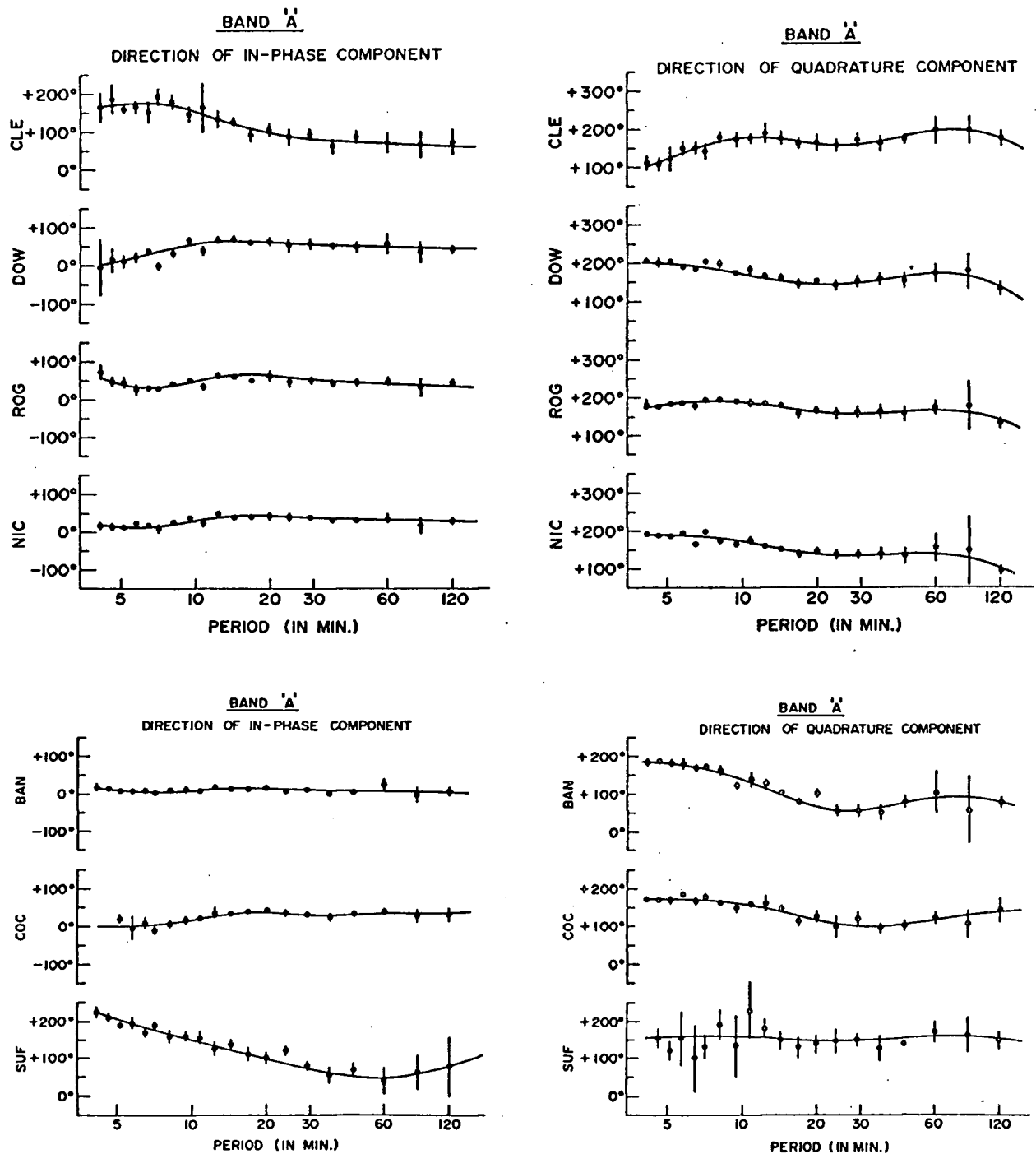
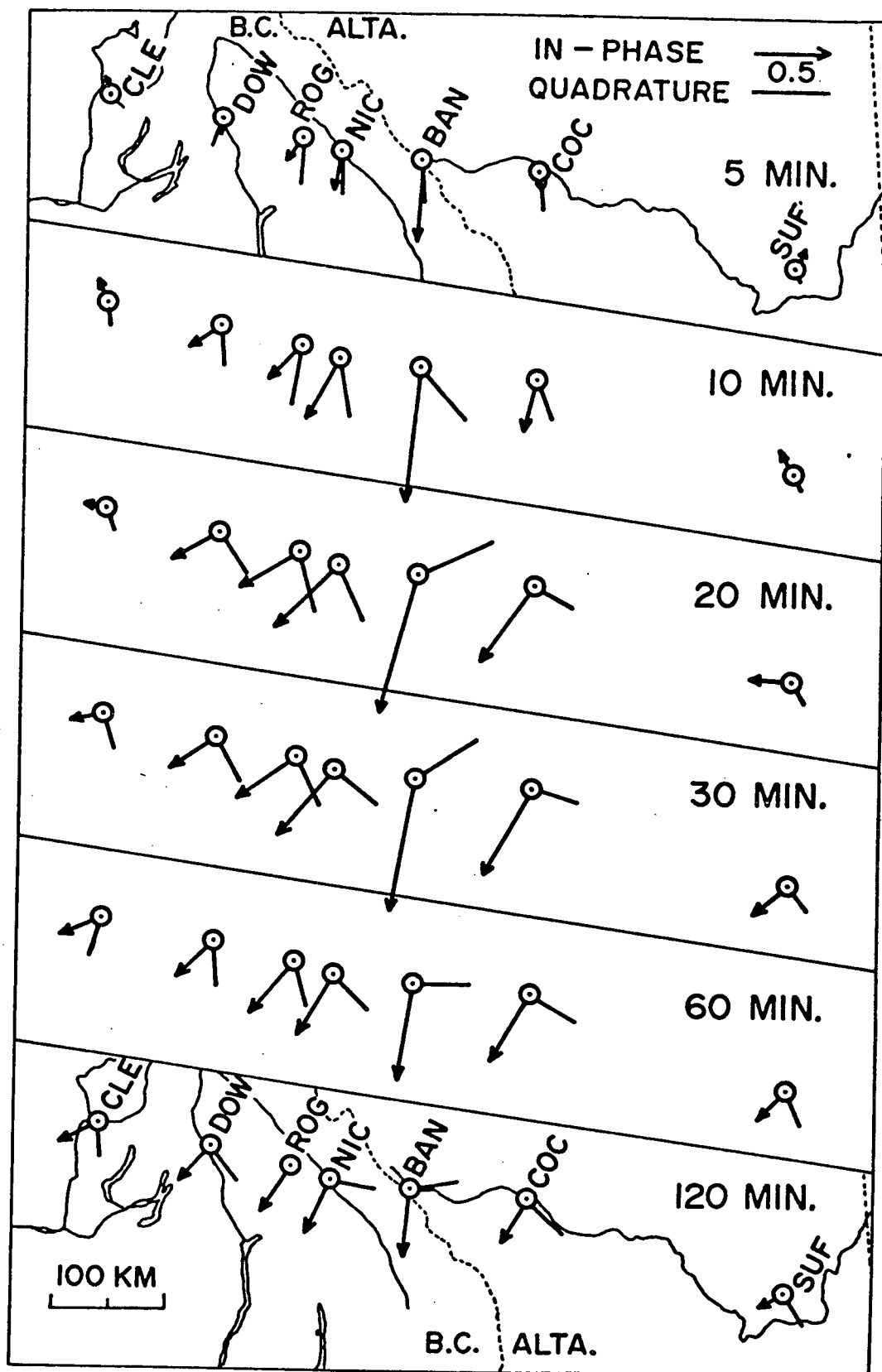


Fig. IV-11. Single-station transfer function directions for Band A (measured positive east of true north).



### BAND A : SINGLE-STATION INDUCTION VECTORS

Fig. IV-12. Single-station transfer function arrows for Band A. The in-phase vectors are negative to follow Parkinson's convention.

since each term of the cross-spectral matrices has numerical errors of estimation associated with it, the matrix  $T$  will assimilate a multiplicity of errors. Even larger instabilities are likely to be introduced by the spatial non-uniformity of the source field. If like-components lack coherence between two sites, there is little hope of obtaining a valid, stable transfer matrix relating the fields observed at each location.

Using the same 11 events as for the  $T_z$  evaluations, mean transfer matrix functions were determined from weighted spectral averages, each event being weighted according to a total-coherence factor between the fields at the analysis site and the reference site (see Appendix II). As before, error limits were obtained from the observed scatter in transfer matrices computed from individual events. *No meaningful transfer matrices could be evaluated for Band B.* The scatter associated with elements of  $T$  was often 70% or higher and frequency trends of both horizontal and vertical transfer terms were erratic and ill-defined. An examination of spatial coherencies (Fig. IV-13) reveals that for Band B the coherence of the horizontal field components ( $R_{HH}$  and  $R_{DD}$ ) falls below 0.75 at about 50 s periods, while the vertical field coherence ( $R_{ZZ}$ ) drops below this level at a period of about 120 s. In comparison, note that this situation is somewhat improved for Band A:  $R_{HH}$  and  $R_{DD}$  maintain values greater than 0.75 for periods longer than 10 minutes, while  $R_{ZZ}$  drops below this level at about 20 minute periods only for the most remote station.

Based on the average weighted spectral estimates of four 36-hour events, mean paired-station transfer matrices and their standard deviations were determined for Band A using CLE as reference. For clarity, the error bars have not been drawn in the figures illustrating the frequency dependence of the elements of  $T$  at each site; consequently, when viewing

## Sample Coherencies

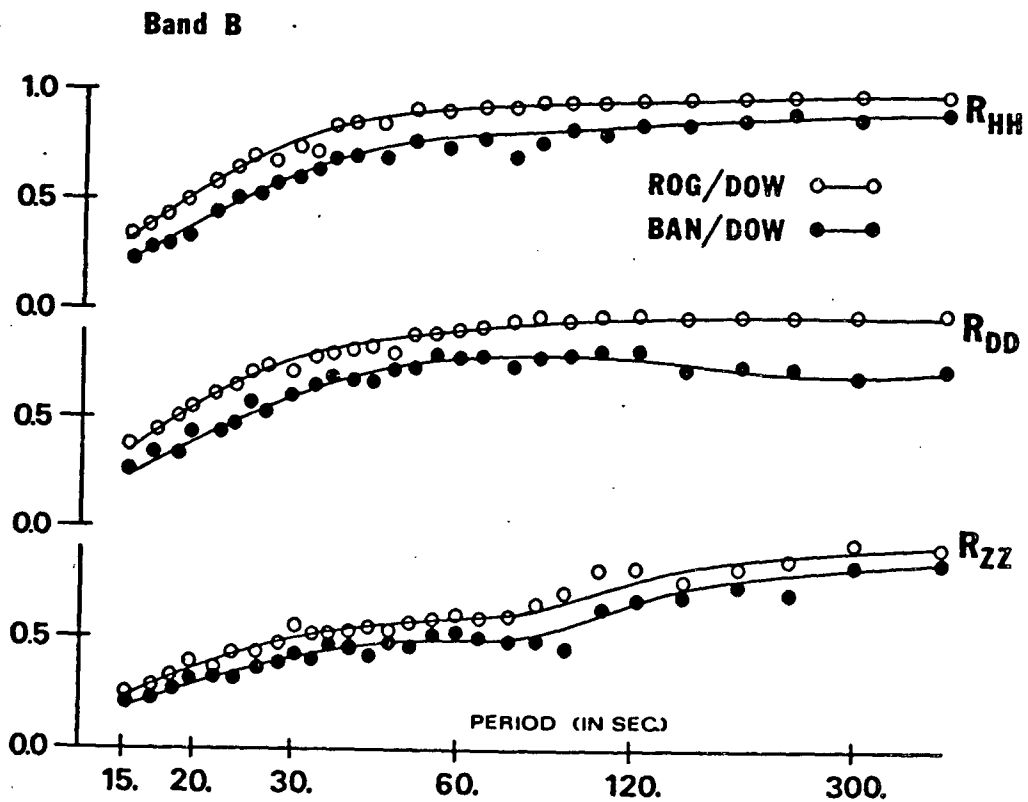
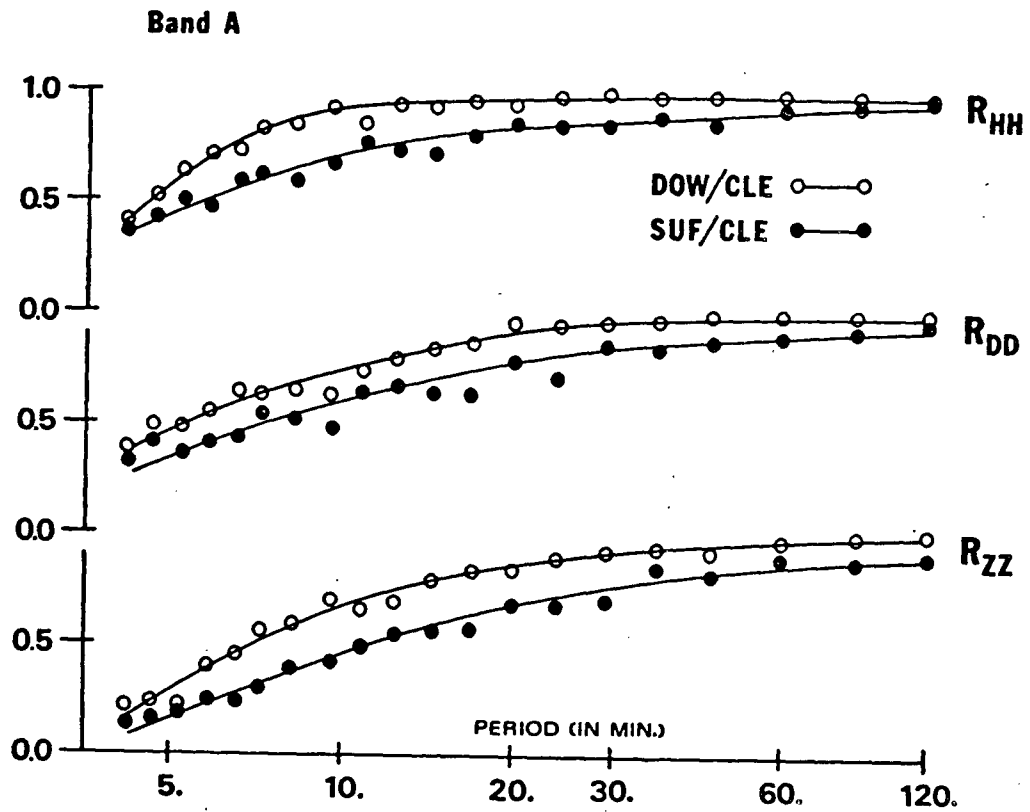


Fig. IV-13. Average coherencies between field components at the reference site and those at the closest and furthest station for Band A and Band B.

these, it must be kept in mind that the scatter about these mean values is easily twice that of the  $T_Z$  determinations, averaging between 30 and 60% and even greater for shorter-period vertical transfer elements ( $z_H$ ,  $z_D$ , and  $z_Z$ ) at sites more remote from the reference location. Nonetheless, frequency trends are apparent, especially at the more anomalous sites, and the following observations are worth noting:

(a) The Diagonal Terms of T

As pointed out in Section III, for zero (or at least constant) coherencies between normal components across a profile, the contribution to the paired-station transfer matrix from the change of normal background can appear only in the diagonal elements of T. Anomalous contributions from lateral conductivity discontinuities can of course appear in any element of T. If the station located over more conductive layering is used as reference, then the modulus values of  $h_H$  and  $d_D$  will have a theoretical maximum of 0.5, while, due to formulation, the real and imaginary parts of all the diagonal elements will be negative and positive respectively. The maximum value for the modulus of  $z_Z$  will be determined by the effective conductivity contrast between the two normal regions. It should be noted that also as a result of formulation, lack of coherence between similar components at different sites will cause the real and imaginary parts of all diagonal terms to approach -1 and 0 respectively.

In Figure IV-14, the diagonal elements of T are plotted as functions of period at each location. For periods less than 10 minutes, the coherencies between stations deteriorated and the above outlined formulation limits were approached. Consequently, the short-period frequency trends have no real physical meaning. For periods greater than 15 minutes, the diagonal transfer terms generally reflect a behaviour expected

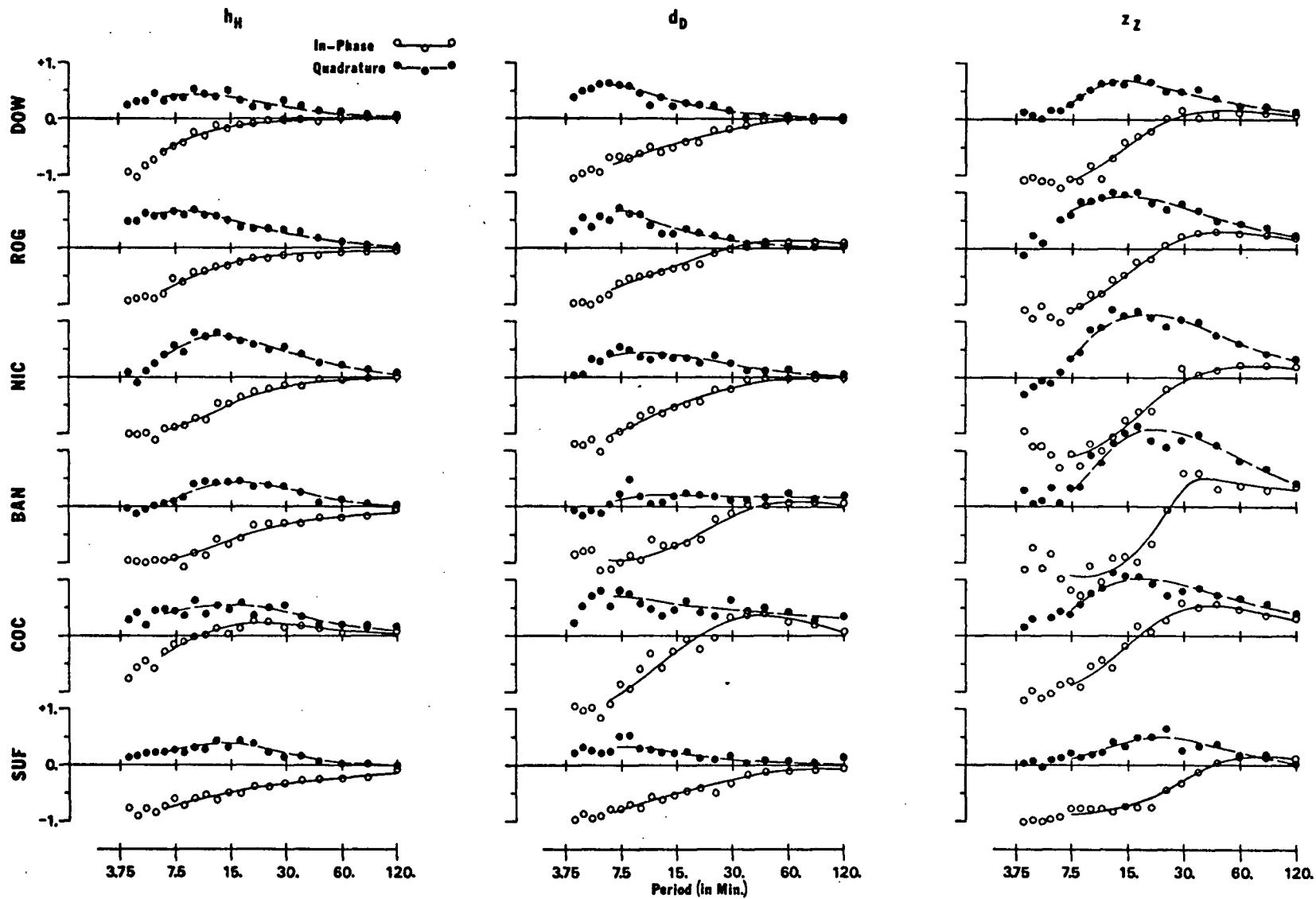


Fig. IV-14. Diagonal elements of the paired-station transfer matrix as functions of period (Band A) at each site.

for the case of a reference site located over a more conductive region with  $h_H$ ,  $d_D$ , and  $z_Z$  following a pattern of values delimited in the previous paragraph. However, it appears necessary to invoke anomalous contributions to account for the changed character of the curves at BAN and COC at these longer periods. For the period range of 7 to 15 minutes, the quadrature parts of  $h_H$ ,  $d_D$ , and  $z_Z$  appear consistently large. Since it is in this period range that coherencies begin to deteriorate, it is probable that these larger values reflect not anomalous contributions but changes in phase patterns for the normal field components.

#### (b) The Horizontal Transfer Functions

The graphs of  $h_Z$  and  $d_Z$  (Figure IV-15) are marked by ill-defined trends and increased standard deviations (not shown) which reflect the difficulties inherent in obtaining horizontal transfer functions at anomalous sites referred to a normal site with low power in Z and reduced values of  $R_{ZZ}$ . As before, this limited coherence renders  $h_Z$  and  $d_Z$  meaningless for periods less than 10 minutes. Significant trends are observable only at the more anomalous locations such as BAN and COC (and perhaps NIC). The curves at SUF may represent valid anomalous contributions, but it must be kept in mind that relations between the field observed at SUF and that observed at the reference site are most likely to be affected by non-uniformities in the source field.

Only at COC are there significant contributions to the horizontal component cross-terms  $h_D$  and  $d_H$  (see Fig. IV-16). For periods greater than 7.5 minutes, both these terms are reasonably well defined functions of frequency and have an average deviation of about 20 to 30% associated with them. The fact that, for COC,  $h_H$  and  $d_D$  are similar but  $h_D$  and  $d_H$  are not indicates that a simple two-dimensional structure cannot be the

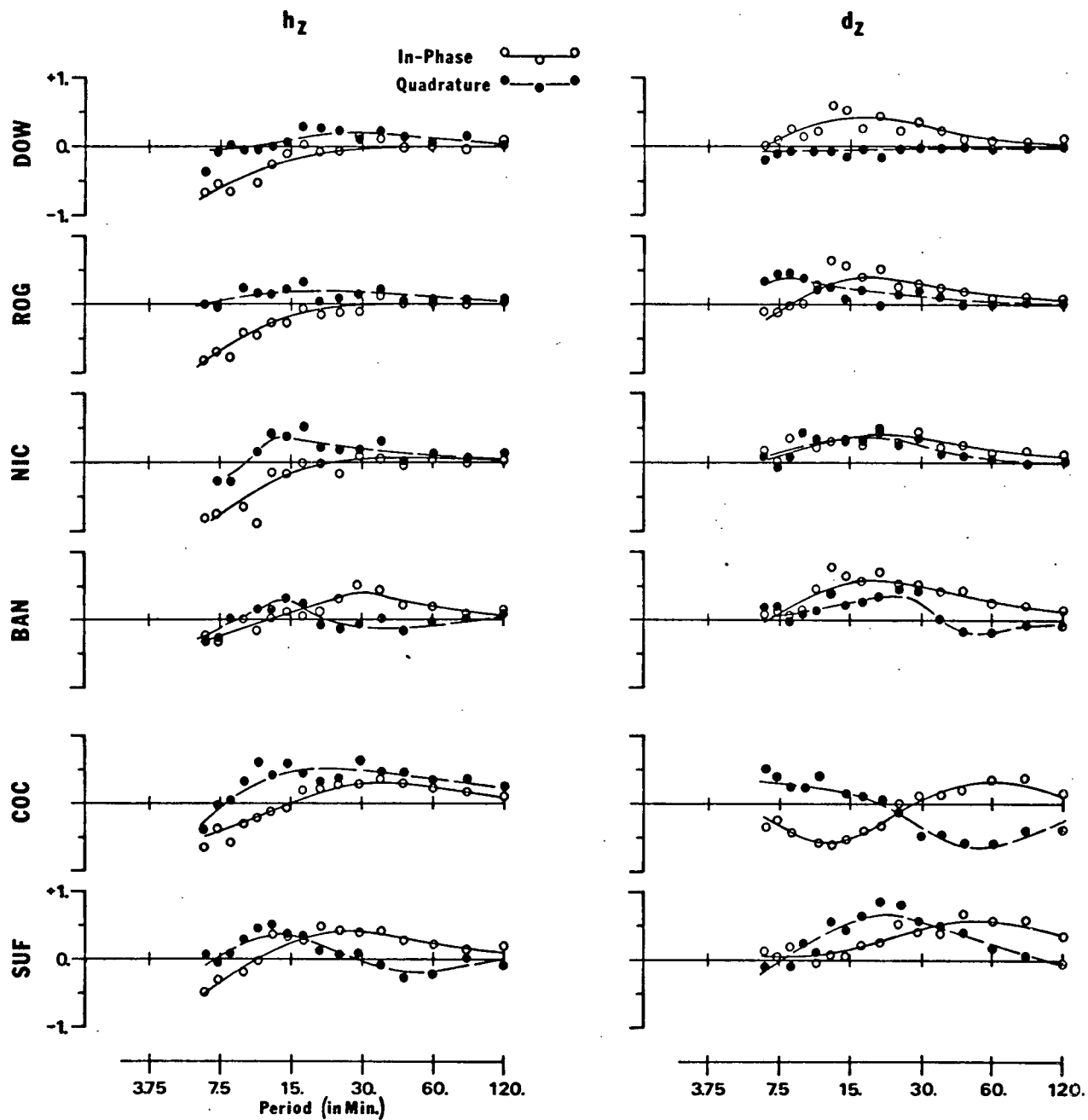


Fig. IV-15. Elements  $h_z$  and  $d_z$  of the paired-station transfer matrix as functions of period (Band A) at each site.



## COC

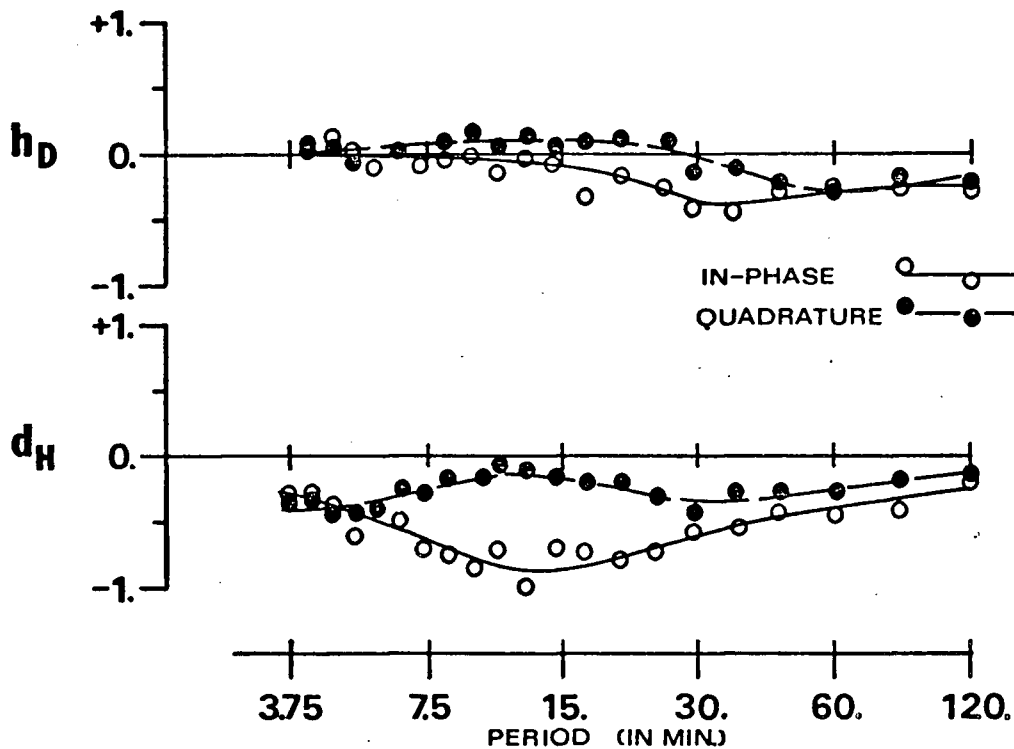


Fig. IV-16. Elements  $h_D$  and  $d_H$  of the paired-station transfer matrix as functions of period (Band A) at COC.

source of the strongly anomalous D component observed at this site.

(c) The Vertical Transfer Function

The vertical transfer function ( $z_H, z_D$ ) contained in the transfer matrix  $T$  is shown in Figure IV-17. Due to the sustained coherence of  $R_{HH}$  and  $R_{DD}$  across the profile, the drawn curves have smaller associated deviation errors ( $\sim 20\%$ ) and appear consistent both frequency-wise and spatially. Maximum anomalous contributions are apparent at BAN and COC at periods of about 20 minutes, which agrees with previous  $T_Z$  determinations. However, the anomalous peaks exhibited by  $z_H'$  and  $z_D'$  (see Fig. IV-18), the components of the single-station vertical transfer function, are both larger and broader than those shown by  $z_H$  and  $z_D$ . Even SUF, which has no

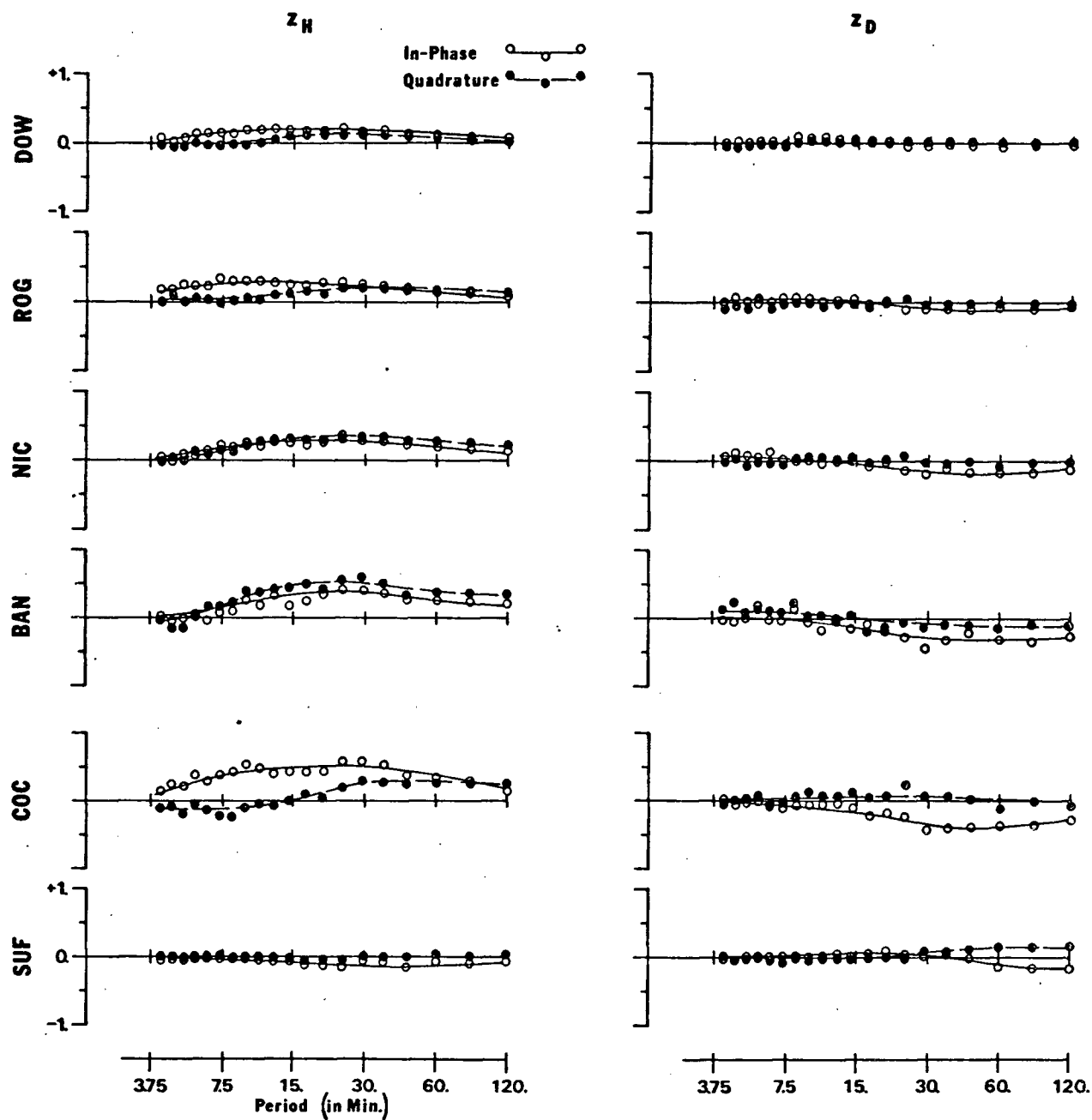


Fig. IV-17. The vertical transfer function elements  $z_H$  and  $z_D$  contained in the transfer matrix  $T$  as functions of period (Band A).

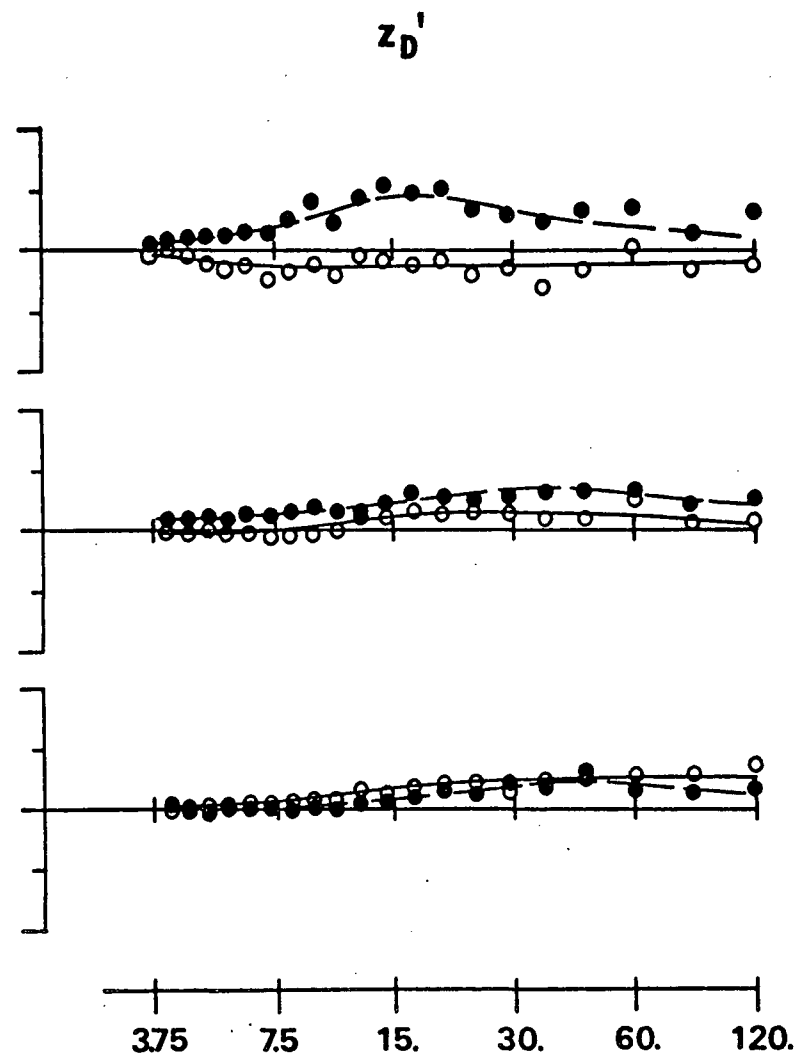
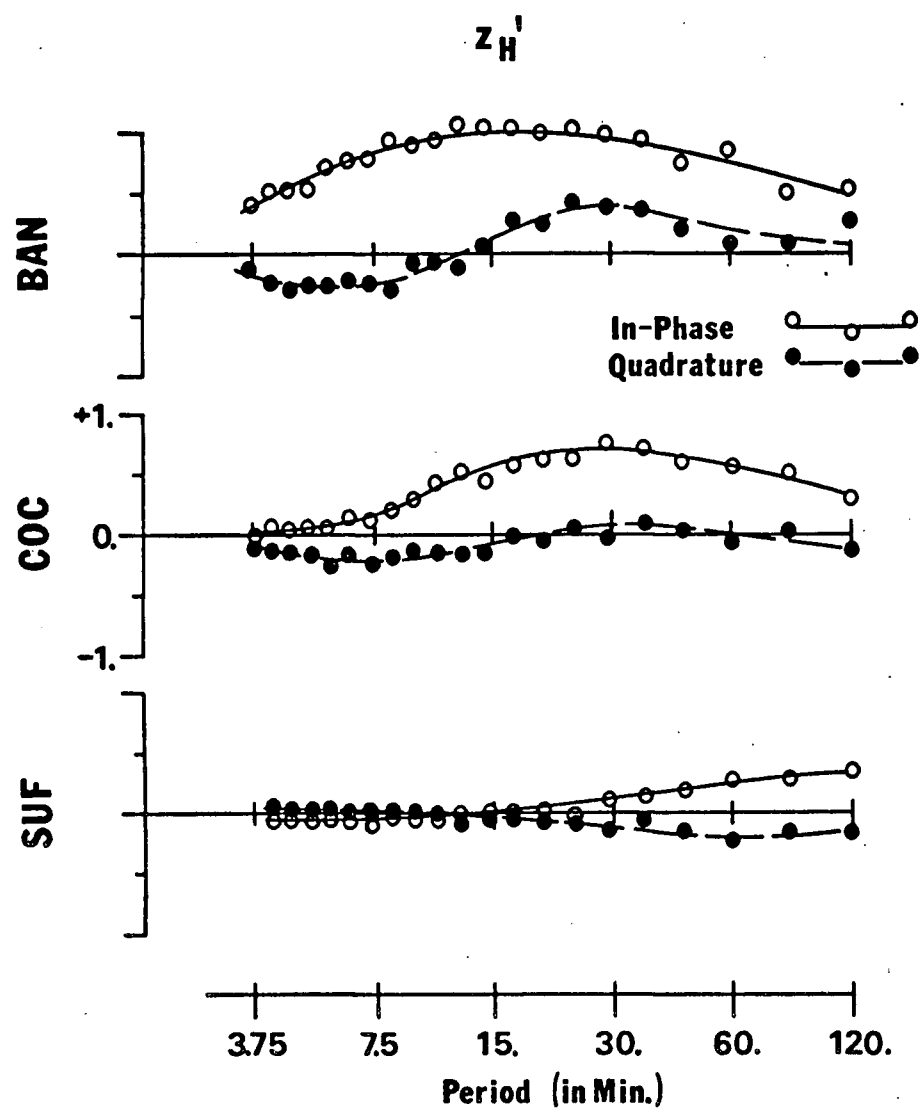


Fig. IV-18. Elements  $z_H'$  and  $z_D'$  of the single-station vertical transfer function,  $T_Z$ , as functions of period (Band A) at BAN, COC, and SUF.

appreciable vertical transfer function contribution in the T determination, shows significant anomalous content for longer periods in the  $T_Z$  evaluation.

### 5. *Qualitative Interpretation*

#### (i) Influence of Source Field Non-Uniformity

For inducing fields with spatial wavelengths less than 800 to 1000 km, no accurate results of conductivity structure can be obtained without taking the source field into consideration (Price, 1962). Consequently, before proceeding with the interpretation of data from a single profile, a measure of source uniformity must be estimated in order to assess the validity of any conductivity structure derived from a uniform-source assumption. Coherency estimates for Band B indicate that for periods less than 30 s, the source field is likely to be non-uniform over distances greater than 50 km while for periods of 50 s to 60 s, source field uniformity becomes questionable over distances greater than 100 km. This implies that numerical results from conventional modelling techniques (c.f. Wright, 1969; Swift, 1971; Jones and Price, 1970) applied to the Band B data at the four closely-spaced broad-band stations become increasingly unrealistic for periods less than 1 minute. For Band A, whose site locations are spread over a 600 km distance, the coherency estimates indicate non-uniform source effects at periods of 10 min. and less. Consequently for this frequency band, there is a possibility that induction at periods smaller than 10 min. is being increasingly controlled by the nature of the source non-uniformity, not the nature of the internal conductivity structure. It must be noted that, as pointed out by Caner (1971), the use of coherency to estimate spatial uniformity is quite

arbitrary and its exact relation to the horizontal scale parameter  $\lambda$  contained in Price's (1962) formulation has not been defined.

(ii) Definition of Normal Field and Regional Conductivity Layering

The sample spectral estimates and spectral ratios show the expected low-Z normal variations within the western Cordillera of British Columbia. However, for this transition zone profile, the rise to high-Z normal variations cannot be separated from the strong anomalous Z variations at the eastern stations. An examination of the diagonal elements of the paired-station transfer matrix can help to resolve this difficulty. The general patterns of  $h_H$ ,  $d_D$ , and  $z_Z$  can be used like a frequency dependent I-ratio to identify regional differences in conductivity layering, with the added ability of detecting the presence of strong anomalous contributions which might bias the standard I-ratio calculation (See the previous discussion: "The Diagonal Terms of T"). In brief, the general trends of  $h_H$ ,  $d_D$  and  $z_Z$  for Band A data are consistent with the previous interpretation (Caner, 1971) of a more conductive layer beneath the western stations of the profile in the lower crust or upper mantle.

To further increase the ambiguity in establishing the high-I normal region, the spectral results for SUF clearly indicate this site to be a low-I station. This requires one of two explanations: 1) What has previously been interpreted as a wide-spread high-I region east of the Canadian Rockies, may in reality be an area of strongly anomalous vertical fields separating regions characterized by attenuated vertical fields (similar to the 'Wasatch Line' anomaly of Reitzel et al. (1970) in the western United States); or 2) the SUF location has a local conductivity

structure associated with it quite distinct from the other profile stations. Other geophysical information (c.f. Kanasewich et al, 1969; and Chandra and Cumming, 1972) indicates the latter to be the case.

### (iii) Direction of the Inducing Field

The horizontal anomalous components caused by vertical induction (related by  $h_z$  and  $d_z$ ) are found to be comparable in magnitude to the vertical anomalous components caused by horizontal induction (related by  $z_H$  and  $z_D$ ). However, due to the large errors and ill-defined trends of  $h_z$  and  $d_z$  and the fact that their contributions are significant only at BAN and COC (and perhaps at SUF), it is impossible to determine 1) whether horizontal or vertical induction dominates, and 2) whether either or both modes of induction are 'primary-source-generated' or 'secondary-anomalous-generated' through mutual induction or conductive channeling in a three-dimensional conductor configuration. The facts that BAN and COC are highly anomalous, and that this anomaly cannot be attributed to a single two-dimensional conductivity structure appear to favour the latter possibility of inductive or conductive coupling.

### (iv) Discrepancies between $T_z$ and $T$

The ambiguities and errors in both the  $T$  and  $T_z$  formulations rule out a meaningful evaluation of the quantitative relation (see equation (3.13) in Section III) between the vertical transfer functions obtained from each technique. It is possible that  $T_z$  actually contains unsuspected contributions from 'cross-terms' as pointed out in the discussion on practical limitations of the transfer function techniques (see equation (3.12) in Section III). However, the consistency of the broader frequency response and larger anomalous contribution indicated by the  $T_z$  technique

at each site, implies that there is either a large anomaly seen uniformly by all profile locations and hence will be precluded from the T formulation, or, more likely, the assumptions concerning normal field coherencies begin to break down. In support of this latter view, the uniform southwest direction of the induction vectors for periods greater than 20 min at sites not only in this study but also to the north (Dragert, 1973) and to the south (Lajoie and Caner, 1970), indicates that consistent normal field coherencies may be present. Whether these are primarily source coherencies or coherencies brought about by the channeling or deflection of large scale internal sheet currents is unresolved.

Although the paired-station transfer matrix formulation allows for such coherencies and consequently results in smaller, less biased anomalous terms, this formulation is adversely affected by coherence relations between the normal components that are non-uniform across the profile. For example, the strong out-of-phase parts of  $h_H$ ,  $d_D$ , and  $z_Z$  observed at periods less than 10 min need not reflect actual differences in horizontal conductivity layering; instead they could indicate a systematic phase change between similar components from station to station dependent primarily on the nature of the source non-uniformity. Davidson and Heirtzler (1968) have pointed out the occurrence of systematic relative phase differences in source fields at sites from 32 to 550 km apart in their study of geomagnetic rapid variations (10 s to 200 s) in the northeastern United States. The application of their findings to longer period variations and in an area much closer to the auroral zone is open to argument.

### (v) Description of the 'Transition Zone' Anomaly

The anomalous field contributions in the geomagnetic transition zone between Revelstoke and Calgary can be attributed to three distinct conductivity structures.

First, from the analysis of Band B data, an enhancement of the horizontal field at NIC and a reversal of the vertical anomalous field between ROG and BAN indicates that a near-surface conductor, having a width of the order of 20 km and striking in a northwest direction, is located in the trench area. Induction ellipses (Everett and Hyndman, 1967) determined from the induction vectors for Band B have an average eccentricity of 10:1, indicating an effective two-dimensional conductivity structure.

Secondly, the change of normal fields from a western low-I to an eastern high-I region accompanied by strong anomalous contributions in the vertical field peaking at 20 min periods mark the presence of a second, deeper lateral conductivity heterogeneity. The anomalous effects due to this structure, observed at practically all profile stations to various extents, show no reversal in the anomalous vertical field component which indicates that this structure is 'step-like' or decreases in depth towards the east. The exact strike of this conductor is more difficult to determine due to the perturbing effects of an associated third anomaly, although it can be estimated to be in a N or NW direction. Induction ellipses evaluated between 15 and 20 minute periods at the more anomalous sites revealed an average eccentricity of 3:1, thus precluding the possibility of a simple two-dimensional conductivity structure.

Finally, the evidence of 1) induction ellipses with small eccentricities (1 to 5) at all anomalous sites; 2) the strong asymmetric



anomalous D contribution observed at COC; 3) the general southwest trend of all induction arrows for periods greater than 10 min ; and 4) the striking resemblance of the  $T_z$  anomalies at BAN and COC to the one at Kootenay Lake (Cochrane and Hyndman, 1970) all imply the presence of a second, highly anomalous, conductive zone striking roughly northeast and lying to the south of COC and most likely connecting with (or identical to) the Kootenay anomalous structure. The exact relation between this anomaly and the transition zone anomaly cannot be clearly defined from this investigation; however, a direct conductive connection appears likely.

#### 6. *Numerical Modelling*

No practical numerical or analytic techniques are available to obtain solutions for the electromagnetic field for general three-dimensional conductivity structures. For two-dimensional structures, solutions for the magnetotelluric E and H fields can be obtained from numerical network-solution techniques based on a transmission line analogy (Wright, 1969; Swift, 1971). These techniques assume a uniform source with an infinite wavelength to allow separate solutions of the 'H polarization' and 'E polarization' modes, and usually the structure response to a horizontal inducing magnetic field perpendicular to strike is evaluated for comparison to observed geomagnetic data. Most techniques employ irregular grids such that the edges of the network are sufficiently distant from the anomalous structure to allow the application of simple Cagnaird (1953) solutions as boundary conditions.

The straightforward generation of a numerical model for the transition zone is therefore hampered on two counts: 1) the previous

qualitative interpretation shows that the 'network-solution' formulation assumptions are certainly not well met in this case; and 2) even if all these formulation conditions were well satisfied, the limited spatial extent and spatial resolution of the data, as well as the ambiguities of anomalous/normal field separation, would prevent the independent generation of a realistic conductivity model based solely on data from this investigation. Consequently, an indirect quantitative approach was adopted. Using Swift's 'transmission-line' numerical method as formulated by Hyndman and Cochrane (1971), model transfer function curves were obtained for the two-dimensional conductivity structures based on Caner's (1971) and Gough and Camfield's (1972) models (shown in Figs. I-2,3 in part I of this thesis). These theoretical curves were then compared to observed transfer function values resolved perpendicular to regional tectonic strike, and thus a 'validity' of each model for the investigated area was established. Implicit in this approach are the assumptions that the transition zone anomaly parallels tectonic strike and that the total anomaly due to both conductivity structures is a simple vector sum of the individual anomalous contributions.

Figure IV-19 presents the computed spatial and frequency response of the in-phase transfer function for both models as well as the observed values of  $T_Z$ . It is obvious that the exact peak locations and peak amplitudes for Band B are ill-defined by the sparse sampling provided by the four broad-band systems. However, the observed data does present a clearly antisymmetric curve defining the Z reversal for periods less than 3 min, and a skewed double-peak curve for the longer periods of this band, indicating the effect of a deeper anomaly on the observed reversal. The relatively shallow 10 km conductive layer of Caner's model affects the shorter periods of Band B too strongly to allow a reasonable fit to

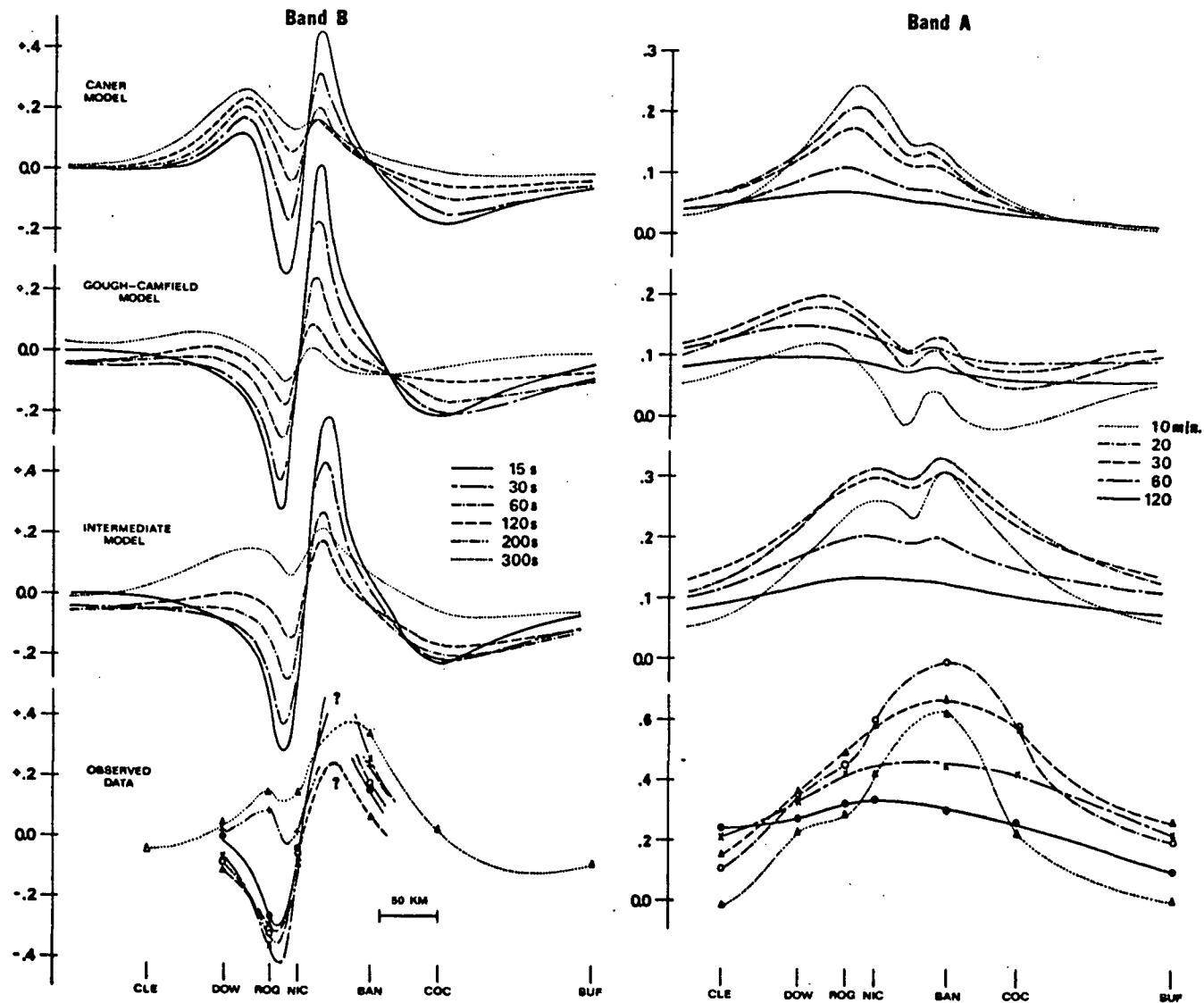


Fig. IV-19. The in-phase transfer function computed for Caner's (1971) and Gough and Camfield's (1972) conductivity models and the observed values. The response of an 'intermediate' model is also shown.

the Z reversal caused by the shallow trench conductor. Gough's western-region conductive layer, on the other hand, is probably too deep (80 km), evidenced by its weak effect on the 5 min period response of the trench conductor. Note that if the eastern deep conductivity structure of Gough's 'double-peak' anomaly is removed and the western conductive layer raised to about 50 km, a more agreeable fit is obtained, as illustrated by the response curves of the 'intermediate model' in Figure IV-19.

The observed in-phase components of  $T_Z$  for Band A are characterized by an extremely strong (0.8) anomalous peak in the 20 min period data. Although this is most likely an overestimate (as discussed previously), neither model generates even half of the observed  $T_Z$  values. (Models with increased conductivity contrasts were attempted but resulted in extremely broad response peaks.) As far as frequency dependence of peak values is concerned, the observed data again favours an intermediate model with a conductive layer underlying the western region at a depth of about 50 km and having an eastern termination beneath the trench area. No double-anomaly structure as observed by Gough for the Idaho Panhandle region is resolved by the data for this profile location.

Again it must be emphasized that this tenuous 'intermediate' model is not intended to serve as an alternate conductivity model for southwestern Canada, resolving differences between the Caner and Gough models. Within the framework of the questionable assumption of the applicability of two-dimensional modelling to this case, it simply suggests possible alterations of either model to make it more concordant with data observed in the area of investigation. This brief quantitative examination of possible two-dimensional models allows the following

limited conclusions to be drawn:

- 1) The trench itself acts as a near-surface two-dimensional conductor with a depth extent of about 2 km and an average conductivity of the order of  $0.1 \text{ (ohm-m)}^{-1}$ . These values are not well defined due to the lack of adequate spatial resolution.
- 2) The conductive layer underlying the western region is probably at or dips to a depth of the order of 40 to 50 km beneath the transition region. The thickness ( $\sim 15 \text{ km}$ ) and conductivity ( $\sim 0.2 \text{ (ohm-m)}^{-1}$ ) of this layer were adopted from the other models and appear to agree with observed data.
- 3) The 'double-peak' structure proposed by Gough and Camfield for the northwestern United States is not found along this profile.
- 4) The fact that the large amplitudes of the observed in-phase components of  $T_Z$  could not be approached by 'reasonable' models, and the fact that the quadrature components of  $T_Z$  revealed trends discordant with expected two-dimensional conductivity patterns, indicate that channeling of current or mutual induction is probably occurring.

### *7. Conclusions and Discussion*

In summary, the conductivity structures which comprise the geomagnetic transition zone anomaly along a line between Revelstoke and Calgary are as follows:

First, the trench itself constitutes a shallow-lying two-dimensional conductivity anomaly. It has been clearly resolved for the first time due to the expanded frequency coverage of the broad-band GDS systems. The depth-conductivity parameters for this conductor are not well defined due to a lack in spatial resolution; however, a conductivity of 0.05 to  $0.1 \text{ (ohm-m)}^{-1}$  and a depth extent of between 1 and 3 km gives model

results agreeable with observations. The most likely cause of this enhanced conductivity are the trench sediments. Although no magnetotelluric-based measurements of conductivity are available for these sediments, other workers (Vozoff and Swift, 1968; Pamenter, 1971; Reddy and Rankin, 1971; Vozoff, 1972) have found sediments with conductivities between  $1.0$  and  $0.1 \text{ (ohm-m)}^{-1}$  down to depths of about  $5 \text{ km}$ .

Secondly, the termination of a conductive subcrustal layer underlying the western Cordillera creates the lateral conductivity discontinuity beneath the western front of the Rocky Mountains which characterizes the transition zone anomaly. The Gough-Camfield model of a deeper conductive layer in a more resistive host appears to provide better agreement with the observed data. The fact that the Gough-Camfield model and the model alterations suggested here are both based on the evaluation of strictly anomalous GDS data, whereas the Caner model is based mainly on magnetotelluric results in normal areas may be significant! Three major alterations of the Gough-Camfield model are suggested:

- 1) The conductive layer underlying the western region placed at a depth of about  $50 \text{ km}$  provides better agreement with the observed data. Thickness and conductivity of this layer remain the same.
- 2) The thickening of this conductive layer near its edge is not resolved by the observed data.
- 3) The double-peak anomaly of the Idaho Panhandle is not observed here, implying that the eastern subcrustal conductivity layer is either absent or has a much smaller conductivity contrast with the host material.

The discrepancy between the Caner "lower-crustal" and the Gough "upper-mantle" conductive layer remains significant, even with a modified depth of  $50 \text{ km}$  for the latter in the transition zone area. It is conceivable

but unlikely that the conductive layer dips eastward increasing its depth by 40 km over a horizontal distance of 200 km. Such an extreme dip may not be necessary in the light of the following observations. First, as pointed out before, geomagnetic depth-sounding interpretation is highly dependent on source wavelength. If source wavelengths are less than 800 km, as indeed indicated possible for periods less than 10 min in this study, then numerical-model-derived depth estimates based on an infinite source wavelength assumption will tend to over-estimate the depth to the conductive layer. Secondly, indications from GDS work (Cochrane and Hyndman,1970) and MT work (Reddy and Rankin,1971) are that both the electric and magnetic fields observed at Pincher are not normal (as assumed by Caner,1969), but are perturbed by anomalous contributions. Corrections for anomalous perturbations (Cochrane and Hyndman,1970) result in GDS data favouring the lower limit of the MT depth range of 10 to 20 km derived by Caner.

Consequently, if an error of 20% is assumed for the rough depth determination of this study, a more acceptable dip (from 20 km to 40 km over a distance of 200 km) would allow the transition anomaly to be still associated with a lower crustal conductivity layer. In fact, recent seismic models (Chandra and Cumming,1972) and gravity models (Stacey,1972) support such a dipping model by proposing a crust/mantle boundary at a depth of about 50 km dipping towards the east under the Rocky Mountain area.

A general discussion of possible causes of the enhanced conductivity of this lower-crust/upper-mantle layer has been given elsewhere (c.f. Caner,1969; Gough and Camfield,1972) and will not be repeated here. In conclusion, it is only hypothesized that if Caner's model is accurate for

the western Cordillera, then a dipping sub-crustal conductive layer is the more probable model for the transition zone anomaly. Such a model relates most easily to oceanic lithosphere, resting on a more resistive upper mantle, underthrusting the continent and through hydration and partial melting, creating a well defined conductivity layer parallel to the crust/mantle interface. In this tectonic interpretation, the Rocky Mountain Trench could mark the eastern extent of the underthrusting.

Finally, a third contribution to the total transition zone anomaly appears to stem from a highly conductive zone to the south of BAN and COC striking roughly perpendicular to the tectonic pattern of the Rocky Mountains. The strong influence of this zone on all induction vectors indicates that this conductor lies roughly at the same depth as the western region conductive layer beneath the transition zone ( $\sim 40$  km), and its conductivity is of the order of  $1 \text{ (ohm-m)}^{-1}$  or better. The lateral extent of this zone is not well defined by these data alone. However, the induction arrows of Hyndman's (Cochrane and Hyndman, 1970) stations in southwestern Canada in conjunction with this data delineate a continuous anomalous zone striking northeast from Kootenay Lake to midway between Calgary and Lethbridge. The weaker anomalous indications at SUF indicate either a termination of this zone or an abrupt change in strike.

This relatively precise definition of the anomalous zone allows an unambiguous correlation with the buried Precambrian rift located by Kanasewich et al. (1969) in southwestern Alberta (see Fig. IV-20). The depth of this rift (35 km) is well defined by seismic reflection in Alberta, whereas its boundaries can be traced by both gravity and magnetic trends into British Columbia. Kanasewich (1968) has proposed that this



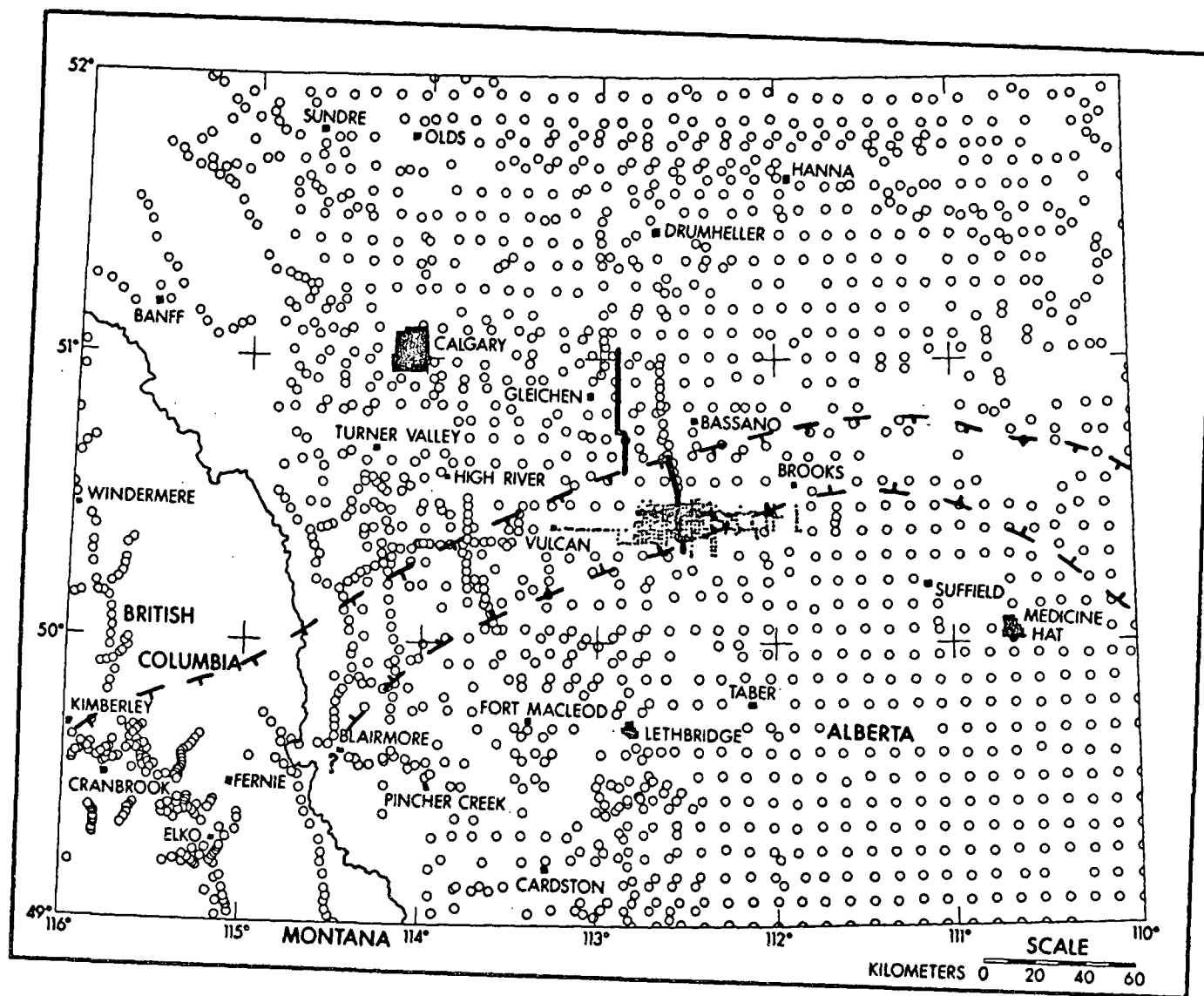


Fig. IV-20. Assumed boundaries of buried Precambrian rift in southwestern Alberta. Circles indicate Dominion Observatory gravity stations. (After Kanasewich et al., 1969.)

rift served as the site for syngenetic and/or hydrothermal ore deposition which created layers of metal oxides and sulfides. Such rift-confined layers would undoubtedly have conductivities much greater than even moderately conductive host rocks, creating a highly conductive channel in the lower crust.

It therefore appears likely that the Kootenay anomaly is not due to a local east-west trending strike-slip feature (Lajoie and Caner, 1970), but due to the conductive effect of mineralization contained within this buried rift zone extending about 300 km from Kootenay Lake northeast into central southern Alberta. Furthermore, if the deeper conductive layer (80 km) proposed to underlie the Front Ranges and the Great Plains (Gough and Camfield, 1972) in the northwestern United States can be reconciled to the shallower depth under discussion here, then the rift conductor may mark the northern extent of this layer.

The pronounced interaction of the main transition-zone anomaly and the rift-zone anomaly has been brought to light by the computed paired-station transfer functions and by the failure of the two-dimensional model to totally account for the observed anomaly. Although the exact interrelation of these anomalies is open to speculation, the following tentative conclusion can be drawn: The previously outlined results (in particular, the strong anomalous D component related to H variations at COC; the exceptionally strong anomalous vertical fields at BAN and COC; the probable normal component coherencies; and the uniform pattern of induction vectors in this and other investigations concerned with the transition zone) all indicate that conductive channeling of internal currents is occurring, similar to that suggested by Camfield et al. (1971) for the North American Central Plains Anomaly. This implies that the nature of the anomaly in this area is primarily determined by the severe local deflection of current patterns induced over a much larger region.

## V. SUMMARY

The primary purpose of investigating the geomagnetic transition anomaly in the areas of the western front of the Rocky Mountains within the Canadian Cordillera has been dealt with in three logical steps.

First, wide-band instrumentation was developed particularly suited to the high-sensitivity and wide-dynamic-range requirements demanded by GDS work in the Canadian Cordillera. Specifically, a field system was built with a recording frequency range of 0.01 to 100 mHz, a dynamic range of 80 db, and a resolution of 0.2γ. The subsequent two-month pilot project showed this system to be both a reliable and a practical instrument for geomagnetic field investigations.

Secondly, numerical techniques suited to the analysis of anomalous geomagnetic data collected along profiles were briefly reviewed in the light of implicit assumptions and practical limitations in order to establish a meaningful, comprehensive analysis method for subsequent work.

Incorporated in such a method are: 1) the periodogram technique employing a frequency-dependent smoothing window to obtain efficient stable spectral estimates for large quantities of shorter period data; 2) the maximum entropy method to extract daily harmonics from limited record lengths; 3) the evaluation of spatial coherences, vertical transfer functions and paired-station transfer matrices, to allow the separation of normal and anomalous fields. Although each aspect of such a method is well known, its practical application in its entirety has been rare.

Finally, the transition zone anomaly in the Rocky Mountain Trench area was investigated by means of a profile of GDS stations extending from Clearwater to Suffield. The extended frequency coverage and the

more comprehensive analysis approach revealed the following structural information:

- 1) The Rocky Mountain Trench sediments form an equivalent two-dimensional near-surface conductor.
- 2) The western region subcrustal conductive layer is at an approximate depth of 40 km beneath the trench area, probably sloping towards the east and thus parallel to the crust/mantle boundary.
- 3) The buried Precambrian rift of southwest Alberta has a strong anomalous geomagnetic expression which is continuous all the way to Kootenay Lake; the anomaly at Kootenay Lake is therefore likely to be rift caused instead of strike-slip caused.

In conclusion, this detailed study has indicated that for this area the nature of the anomaly is not determined solely by direct induction in the local structures; instead, the local structures serve to deflect general current patterns induced over a larger region.

## REFERENCES

- BARNARD, T.E., Analytical studies of techniques for the computation of high resolution wavenumber spectra, Spec. Rep. 9, Texas Instrum. Advanc. Array Res., Dallas, Texas, 1969.
- BLACKMAN, R.B., and J.W. TUKEY, The Measurement of Power Spectra, Dover, New York, 1958.
- BULLARD, E.C., and R.L. PARKER, Electromagnetic induction in the oceans, in *The Sea*, ch. 6, Interscience, New York, 1970.
- BURG, J.P., Maximum entropy spectral analysis, paper presented at the 37th meeting, Soc. Explor. Geophys., Oklahoma City, Okla., Oct. 31, 1967.
- BURG, J.P., A new analysis technique for time series data, paper presented at NATO Advanced Study Institute on Signal Processing, Enschede, Netherlands, August 1968.
- CAGNIARD, L., Basic theory of the magnetotelluric method of geophysical prospecting, *Geophysics*, 18, 605-635, 1953.
- CAMFIELD, P.A., D.I. GOUGH, and H. PORATH, Magnetometer array studies in the northwestern United States and southwestern Canada, *Geophys. J.R. Astr. Soc.*, 22, 201-221, 1971.
- CANER, B., and W.H. CANNON, Geomagnetic depth-sounding and correlation with other geophysical data in western North America, *Nature*, 207, 927-928, 1965.
- CANER, B., W.H. CANNON, and C.E. LIVINGSTONE, Geomagnetic depth-sounding and upper mantle structure in the Cordillera region of western North America, *J. Geophys. Res.*, 72, 6335-6351, 1967.
- CANER, B., Electrical conductivity structure of the lower crust and upper mantle in western Canada, unpublished PH.D. thesis, University of British Columbia, Vancouver, 1969.
- CANER, B., D.R. AULD, H. DRAGERT, and P.A. CAMFIELD, Geomagnetic depth-sounding and crustal structure in western Canada, *J. Geophys. Res.*, 76, 7181-7201, 1971.
- CANER, B., Quantitative interpretation of geomagnetic depth-sounding data in western Canada, *J. Geophys. Res.*, 76, 7202-7216, 1971.
- CANER, B., and H. DRAGERT, Instrumentation for wide-frequency-band (0.01-100 millihertz) geomagnetic induction work, *Zeitschrift fuer Geophysik*, 38, 121-132, 1972.
- CHANDRA, N.N., and G.L. CUMMING, Seismic refraction studies in western Canada, *Can. J. Earth Sci.*, 9, 1099-1109, 1972.

- COCHRANE, N.A., and R.D. HYNDMAN, A new analysis of geomagnetic depth-sounding data from western Canada, *Can. J. Earth Sci.*, 7, 1208-1218, 1970.
- COOLEY, J.W., and J.W. TUKEY, An algorithm for the machine calculation of complex Fourier series, *Mathematics of Computation*, 19, April, 1965.
- DAVIDSON, M.J., and J.R. HEIRTZLER, Spatial coherence of geomagnetic rapid variations, *J. Geophys. Res.*, 73, 2143-2162, 1968.
- DRAGERT, H., A geomagnetic depth-sounding profile across central British Columbia, unpublished M. Sc. thesis, University of British Columbia, Vancouver, 1970.
- DRAGERT, H., A transfer function analysis of a geomagnetic depth-sounding profile across central B.C., *Can. J. Earth Sci.*, 1973 (in press).
- EDWARDS, R.N., L.K. LAW, and A. WHITE, Geomagnetic variations in the British Isles and their relation to electrical currents in the ocean and shallow seas, *Phil. Trans. Roy. Soc. London*, 270, 289-323, 1971.
- EVERETT, J.E., and R.D. HYNDMAN, Geomagnetic variations and electrical conductivity structure in southwestern Australia, *Phys. Earth. Planet. Int.*, 1, 24-34, 1967.
- GOUGH, D.I., and P.A. CAMFIELD, Conductive structures under the northern Rocky Mountains, *J. Geophys. Res.*, submitted 1972.
- GRETTON, H.W., The alteration of the magnetic field of transient variations by an axisymmetric island in a large ocean, *Planetary Space Sci.*, 21, 97-112, 1973.
- HYNDMAN, R.D., Electrical conductivity inhomogenities in the earth's upper mantle, unpublished M. Sc. thesis, University of British Columbia, Vancouver, 1963.
- HYNDMAN, R.D., and N.A. COCHRANE, Electrical conductivity structure by geomagnetic induction at the continental margin of Atlantic Canada, *Geophys. J. R. Astr. Soc.*, 25, 425-446, 1971.
- JENKINS, G.M., General considerations in the analysis of spectra, *Technometrics*, 3, 98-131, 1961.
- JONES, R.H., A reappraisal of the periodogram in spectral analysis, *Technometrics*, 7, 531-542, 1965.
- JONES, F.W., and A.T. PRICE, The perturbations of alternating geomagnetic fields by conductivity anomalies, *Geophys. J. R. Astr. Soc.*, 20, 317-334, 1970.

- KANASEWICH, E.R., Precambrian rift: genesis of strata-bound ore deposits, *Science*, 161, 1002-1005, 1968.
- KANASEWICH, E.R., R.M. CLOWES, and C.H. McCLOUGHAN, A buried Precambrian rift in western Canada, *Tectonophysics*, 8, 513-527, 1969.
- LACOSS, R.T., Data adaptive spectral analysis methods, *Geophysics*, 36, 661-675, 1971.
- Lajoie, J.J., and B. CANER, Geomagnetic induction anomaly near Kootenay Lake — a strike-slip feature in the lower crust?, *Can. J. Earth Sci.*, 7, 1568-1579, 1970.
- LAMBERT, A., and B. CANER, Geomagnetic depth-sounding and the coast effect in western Canada, *Can. J. Earth Sci.*, 2, 485-509, 1965.
- LINES, L.R., and F.W. JONES, The perturbation of alternating geomagnetic fields by three-dimensional island structures, *Geophys. J. R. Astr. Soc.*, in press, 1973.
- MADDEN, T., and C.M. SWIFT, Magnetotelluric studies of the crust and upper mantle, in *The Earth's Crust and Upper Mantle*, *Geophys. Monogr. Ser.*, vol. 13, pp. 469-479, AGU, Washington, D.C., 1969.
- McGEE, T.M., On Burg's method of spectral analysis, unpublished manuscript, Vening Meinesz Laboratory, Utrecht, July, 1969.
- PAMENTER, B., Magnetotellurics declared a practical exploration tool, *Oilweek*, January, pp. 20-24, 1971.
- PARKINSON, W.D., The influence of continents and oceans on geomagnetic variations, *Geophys. J.*, 4, 441-449, 1962.
- PEACOCK, K.L., and S. TREITEL, Predictive deconvolution: theory and practice, *Geophysics*, 34, 155-169, 1969.
- PORATH, H., D.W. OLDENBURG, and D.I. GOUGH, Separation of magnetic variation fields and conductive structures in the western United States, *Geophys. J.*, 19, 237-260, 1970.
- PORATH, H., D.I. GOUGH, and P.A. CAMFIELD, Conductive structures in the northwestern United States and southwest Canada, *Geophys. J. R. Astr. Soc.*, 23, 387-398, 1971.
- PRICE, A.T., Electromagnetic induction in a semi-infinite conductor with a plane boundary, *Quart. J. Mech. Appl. Math.*, 3, 385-410, 1950.
- PRICE, A.T., The theory of magnetotelluric methods when the source field is considered, *J. Geophys. Res.*, 67, 1907-1918, 1962.
- REDDY, I.K., and D. RANKIN, Magnetotelluric measurements in central Alberta, *Geophysics*, 36, 739-753, 1971.

- REITZEL, J.S., D.I. GOUGH, H. PORATH, and C.W. ANDERSON III, Geomagnetic deep sounding and upper mantle structure in the western United States, *Geophys. J.*, 19, 213-235, 1970.
- ROSTOKER, G., Midlatitude transition bays and their relation of spatial movements of overhead current systems, *J. Geophys. Res.*, 71, 79-95, 1966.
- SCHMUCKER, U., Anomalies of geomagnetic variations in the southwestern United States, *J. Geomag. Geoelec.*, 15, 193-221, 1964.
- SCHMUCKER, U., An introduction to induction anomalies, *J. Geomag. Geoelec.*, 22, 9-33, 1970a.
- SCHMUCKER, U., Anomalies of geomagnetic variations in the southwestern United States, *Bull. Scripps Inst. Oceanog.*, 13, University of California, 1970.
- SERSON, P.H., An electrical recording magnetometer, *Can. J. Physics*, 35, 1387-1394, 1957.
- STACEY, R.A., Gravity anomalies, crustal structure and plate tectonics in the Canadian Cordillera, *Can. J. Earth Sci.*, submitted 1973.
- SWIFT, C.M., Theoretical magnetotelluric and turam response from two-dimensional inhomogenities, *Geophysics*, 36, 38-52, 1971.
- TREUMANN, R., Electromagnetic induction problem in plates with two-dimensional conductivity distribution. II Approximate method and solutions, *Geomag. and Aeronomy*, 10, 464-472, 1970.
- TRIGG, D.F., An automatic zero suppression circuit, *Rev. of Scient. Instr.*, 41, 1298-1302, 1970.
- TRIGG, D.F., P.H. SERSON, and P.A. CAMFIELD, A solid-state electrical recording magnetometer, *Publ. Earth Physics Branch, Ottawa*, 41, 5, 67-80, 1971.
- ULRYCH, T.J., Maximum entropy power spectrum of truncated sinusoids, *J. Geophys. Res.*, 77, 1396-1400, 1972.
- ULRYCH, T.J., D.E. SMYLIE, O.G. JENSEN, and G.K.C. CLARKE, Predictive filtering and smoothing of short records using maximum entropy, *J. Geophys. Res.*, in press, 1973.
- VOZOFF, K., and C.M. SWIFT, Magnetotelluric measurements in the North German basin, *Geophys. Prosp.*, 16, 454-473, 1968.
- VOZOFF, K., The magnetotelluric method in the exploration of sedimentary basins, *Geophysics*, 37, 98-141, 1972.
- WRIGHT, J.A., The magnetotelluric and geomagnetic response of two dimensional structures, *Gamma*, 7, *Inst. fuer Geophysik u. Meteorologie, Tech. Univ. Braunschweig*, 1969.



## APPENDIX I

## Data Preparation

The analogue data recorded on the slow-speed FM tape recorders was reduced and prepared for numerical analysis in the following manner.

## (i) Digitization

Using a Sanborn Model 3900 tape recorder, the analogue signals were first played back onto a six-channel graph for editing purposes. This allowed selection of storm events for subsequent digitization on an Interdata Analogue/Digital Converter. The data were digitized in three bands:

- 1) Band 1, having a digitizing interval of 2.50 s and record lengths of 100 min.
- 2) Band 2, having a digitizing interval of 1.00 min and a record length of 36 hr.
- 3) Band 3, having a digitizing interval of 10.0 min and a record length of 100 hr.

These digitizing intervals were controlled to within an accuracy of better than 1% by the use of a constantly monitored pulse generator.

Before digitizing, each band was pre-filtered at its Nyquist frequency by a Rockland active low-pass filter to reduce aliasing and play-back noise. The voltages of these filtered analogue signals were then digitized over a range of  $\pm 10.00$  v with a resolution of 10 mv. In practice, the A/D converter allowed the simultaneous digitization of four channels and consequently, three components along with a timing reference were digitized at one time. These digitized data were initially recorded in binary form and in a multiplexed format on 7-track magnetic tape and later de-multiplexed and converted to a decimal format with four significant figures.

### (ii) Altering of Digitized Traces

To determine the reliability of the digitized traces and to remove spurious pulses from actual magnetic variations, all digitized data were viewed at an Adage Graphics Terminal. A program written by J. W. Coulthard at the Computing Centre of the University of B. C. allowed direct visual/digital interaction between the displayed trace and the corresponding stored data array. By automatic scaling and efficient isolation of trace sections, the data could be not only critically viewed but also altered in the following manner:

- 1) The value of single points could be changed. This allowed the removal of spikes.
- 2) The value of a range of points could be changed by a constant. This allowed the removal of step functions.
- 3) The value of a range of points could be changed by the addition of an externally supplied function. This allowed the removal of the exponentially-decaying filter-convolved time pulses.

These altered data traces were considered to be the best digital representation of actual magnetic fluctuations and were stored on magnetic tape for subsequent numerical analysis.

### (iii) Preparation of Data for Spectral Analysis

For the spectral estimations of Band 1 and Band 2 data, standard periodogram techniques were employed. Consequently, for optimum Fourier transform calculations the data were prepared in the following manner:

#### (a) Removal of mean and long-period contributions:

To avoid strong DC and long-period spectral contributions, each time series was fitted to the linear equation

$$(1.0) \quad y = mt + y_0$$

by the method of least-mean-squares. The mean value and linear drift thus determined were then subtracted from the data. For Band 2 data, the strong contributions of the first four daily harmonics were similarly removed by fitting the data to the equation

$$(1.1) \quad y = y_0 + mt + A_k \cos(2\pi k/\tau) + B_k \sin(2\pi k/\tau)$$

where  $\tau = 24$  hr

and  $k = 1, 2, 3$ , and  $4$ .

(b) Prewhitening of series:

To further reduce spectral leakage from the stronger long-period variations, the time series were prewhitened by the simple relation

$$(1.2) \quad y(t_k)' = y(t_k + \Delta t) - \alpha y(t_k) \quad 0 \leq \alpha < 1$$

where  $\alpha$  = a prewhitening factor

$\Delta t$  = the digitizing interval

If  $\alpha$  was not specified externally, it was then automatically evaluated by the relation

$$(1.3) \quad \alpha = \frac{\sum_{k=0}^{N-1} y(k\Delta t)y((k+1)\Delta t)}{\sum_{k=0}^{N-1} y(k\Delta t)^2}$$

After auto- and cross-spectral estimation, the transforms of the prewhitened series were re-coloured by the relation

$$(1.4) \quad F_y(\omega) = F_y'(\omega)/(e^{+i\omega\Delta t} - \alpha)$$

(c) Tapering of series and zero extension:

To minimize side-lobing, each time series was tapered over its first and last M points (where M was made 10% of series length) by a cosine-bell window. That is,

$$(1.5) \quad y'(t_k) = W(k) y(t_k) \quad k = 0, 1, \dots, N-1$$

$$\text{where } W(k) = \begin{cases} \frac{1 + \cos\{\pi k / (M-1)\}}{2} & \text{for } k \leq M \\ 1 & \text{for } M \leq k < N-1-M \\ \frac{1 + \cos\{\pi((k+M-N)/M)\}}{2} & \text{for } k \geq N-1-M \end{cases}$$

To further reduce side-band ripple associated with spectral estimates of finite data samples and to increase the efficiency of the Fast Fourier Transform, about 10% zeros were added such that the extended series length  $N'$  was either an exact power of two or at least an even integer having a highly composite number of low prime terms.

## APPENDIX II

## A. Generation of the Variable-Width Window

In the evaluation of smoothed spectral estimates, a Parzen window (2.0) was employed.

$$(2.0) \quad W(\omega_n, M) = \frac{3M}{4\pi} \left\{ \frac{\sin(\omega_n M/4)}{\omega_n M/4} \right\}^4$$

If the time series analyzed is a stationary Gaussian process with a power spectrum that does not vary too much over the bandwidth of the window  $W$ , then the normalized asymptotic variance of (2.0) may be approximated by (Jenkins, 1961)

$$(2.1) \quad V \approx 0.542 M/N$$

while its "equivalent equ-variability bandwidth", defined by Jenkins (1961) as "the base width of the rectangular or band-pass window which has the same area and which in addition, gives rise to the same variance for the spectral estimate as the given window", is estimated by

$$(2.2) \quad B \approx 1/M \quad (\text{in Hz})$$

Using relation (2.1),  $M$  was determined as a function of frequency as follows.  $V$  was arbitrarily set to a minimum value,  $V_{\text{MIN}}$  (0.01), at the Nyquist frequency and then allowed to increase (with decreasing frequency) according to a logarithmic or square-root function until an arbitrary, preset maximum value,  $V_{\text{MAX}}$  (0.75), was reached at the fundamental period of the data sample. For example, for the square-root-function dependence,

V was calculated by

$$(2.3) \quad V(\tau_k) = V_{\text{MIN}} + \frac{(V_{\text{MAX}} - V_{\text{MIN}})}{(\sqrt{\tau_2} - \sqrt{\tau_{\text{NY}}})} (\sqrt{\tau_{\text{NY}+1-k}} - \sqrt{\tau_{\text{NY}}}) \quad k=1,2,\dots,\text{NY}-1$$

where  $\tau_k = \frac{2\pi}{\omega_k}$ , the sampled periods

$\tau_2$  = the fundamental period of the data sample

$\tau_{\text{NY}}$  = the Nyquist period

The resultant frequency dependent value of M was then used to generate the smoothing window (2.0) which subsequently possessed a variable variance and a variable equivalent bandwidth as determined by (2.1) and (2.2) respectively. The window was not evaluated at each  $\omega_n$  but only at certain frequencies such that adjacent windows intersected at their equivalent bandwidths.

For example, in the analysis of Band A data, the Parzen window at the Nyquist period (2.00 min) had an equivalent bandwidth of 0.20 min and a variance of 1.0%. At a centre period of 20 min, the smoothing window possessed a bandwidth of 3.3 min and a variance of 6.0%, whereas at 60 min, the bandwidth and variance increased to 17 min and 11% respectively.

## B. Computation of Transfer Functions

### (i) Single-Station Vertical Transfer Function

The smoothed auto- and cross-spectral estimates of the three magnetic field components observed at one site are used in the relations (Cochrane and Hyndman, 1970)

$$z_H' = \frac{S_{ZH} S_{DD} - S_{ZD} S_{DH}}{S_{HH} S_{DD} - S_{DH} S_{HD}} \quad (2.4)$$

$$z_D' = \frac{S_{ZD} S_{HH} - S_{ZH} S_{HD}}{S_{HH} S_{DD} - S_{DH} S_{HD}}$$

to evaluate the complex vector  $T_Z(z_H', z_D')$  at each frequency  $\omega_k$ . The mean value  $\overline{T_Z}$  is obtained by using the weighted average of spectral estimates from  $R$  different events, where the spectral contributions from each event are normalized by the  $Z$  power; i.e.

$$\overline{S_{XY}} = \frac{\sum_{r=1}^R (S_{XY})_r / (S_{ZZ})_r}{\sum_{r=1}^R 1 / (S_{ZZ})_r} \quad \text{where } X \text{ or } Y = H, D, Z \quad (2.5)$$

The error associated with the computed  $\overline{T_Z}$  was determined by evaluating  $(T_Z)_r$  for each of the  $R$  events, and then calculating the standard deviation of the real and imaginary parts of the mean values  $\overline{z_H'}$  and  $\overline{z_D'}$  as shown by (2.6)

$$\epsilon\{\text{Re}(\overline{z_H'})\} = \left\{ \sum_{r=1}^R [\text{Re}(\overline{z_H'}) - \text{Re}(z_H')_r]^2 / (R-1) \right\}^{1/2} \quad (2.6)$$

The errors associated with the magnitudes and directions of the in-phase and quadrature induction vectors were evaluated from a standard functional combination of the individual component errors as given by (2.7).

$$\epsilon_f^2 = \sum_{j=1}^J \left\{ \frac{\partial f}{\partial x_j} \epsilon(x_j) \right\}^2 \quad (2.7)$$

For example, setting  $\text{Re}(\overline{z_H^T}) = a_1$  and  $\text{Re}(\overline{z_D^T}) = a_2$ , the magnitude of the in-phase vector is given by

$$f = \{a_1^2 + a_2^2\}^{1/2}$$

Consequently, the error associated with  $f$  is given by

$$\epsilon_f^2 = \sum_{j=1}^2 \left\{ \frac{\partial f}{\partial a_j} \epsilon(a_j) \right\}^2 = \{(a_1 \epsilon(a_1))^2 + (a_2 \epsilon(a_2))^2\} / f^2$$

Similarly, the direction of the in-phase vector is determined by

$$g = \tan^{-1} (a_2/a_1)$$

Applying relation (2.7) then yields an error estimate of

$$\epsilon_g^2 = \{(a_2 \epsilon(a_1))^2 + (a_1 \epsilon(a_2))^2\} / f^4$$

## (ii) Paired-Station Transfer Function Matrix

The smoothed auto- and cross-spectral estimates of the magnetic field components at an anomalous and at a reference site are used to generate the spectral matrices  $P_{AN}$  and  $P_{NN}$ . (See Section III, equation (3.2).) The inverse of the matrix  $P_{NN}$  is then estimated numerically by the Gauss-Jordan technique, and the transfer matrix is evaluated by

$$(2.8) \quad T = P_{AN} P_{NN}^{-1}$$

at each frequency  $\omega_k$ . The reliability of the inverse can be monitored by the calculation of an approximate Turing-condition number given by



$$(2.9) \quad c = \left\{ \frac{1}{N} \sum_{i,j=1}^N |p_{ij}|^2 \sum_{i,j=1}^N |q_{ij}|^2 \right\}^{1/2}$$

where  $N=3$ , and  $p_{ij}$  and  $q_{ij}$  represent the elements of  $P_{NN}$  and  $P_{NN}^{-1}$  respectively. (For an exact inverse,  $c = 1$ .)

As in the case for  $\overline{T}_Z$ , the mean value  $\overline{T}$  is obtained by using the weighted average of spectral estimates from  $R$  events.

$$(3.0) \quad \overline{T} = \left\{ \sum_{r=1}^R w_r (P_{AN})_r \right\} \cdot \left\{ \sum_{r=1}^R w_r (P_{NN})_r \right\}^{-1}$$

where  $w_r = (R_{HH}^2 + R_{DD}^2 + R_{ZZ}^2)^{1/2}$ , the vector magnitude of the H, D, and Z coherencies between the two sites.

By computing transfer matrices separately for each event, the errors associated with the real and imaginary parts of each element of the matrix  $\overline{T}$  were determined in a manner entirely analagous to equation (2.6).